The Development Of Biomagnetic Systems : Planar Gradiometers And Software Tools

Thesis

The development of biomagnetic systems: planar gradiometers and software tools.[1]

Mr Krishna Devi Singh BSc.

May 1991

[1]Thesis submitted for the degree of Doctor of Philosophy in the discipline of Physics

EX12

HIGHER DEGREES OFFICE

LIBRARY AUTHORISATION FORM

STUDENT: Mr K.D SINGH SERIAL NO: M70L509

DEGREE: PhD

TITLE OF THESIS: The Development of Biomagnetic Measurement systems - planar gradiometers and software tools.

I confirm that I am willing that my thesis be made available to readers and maybe photocopied, subject to the discretion of the Librarian.

SIGNED: K.D Singh DATE: 2 Jan 1991

Abstract

This thesis is concerned with two aspects of the design and construction of biomagnetic systems. Firstly, it considers the optimum design of planar gradiometers. The modelling of gradiometers is discussed and an algorithm for optimising the sensitivity of a specific type of gradiometer is presented. A test thin-film procedure for the manufacture of a planar gradiometer is outlined. The performance of three different types of gradiometer in recovering test current distributions, using a distributed current analysis technique, is assessed.

Secondly, four major software tools that are essential in the analysis of data from large multi-channel biomagnetic systems are presented. These tools are then used to analyze data from a visual evoked response experiment. The system used to collect data was the Helsinki multi-channel system which consists of 24 planar gradiometers. The results confirm the retinotopic mapping of visual field information, and suggest that the time evolution of activity in different parts of the visual cortex is similar for early latencies.

Acknowledgements

There are two large groups of people that have made the completion of this thesis possible; my work colleagues who have given technical help and advice and those friends and family who have kept me sane when it all seemed too much. I'm lucky to be able to say that the two groups are not mutually exclusive!

The thin film project mentioned in chapter 7 was carried out at Leicester Polytechnic, and I am grateful to Norman Bevan and Colin Horley for technical support and advice. My thanks also go to David Grimes for his advice and spare bedroom in Leicester! Kathia Fiaschi and Ian Thomas here at The Open University helped me a great deal with the cooling and SQUIDLET tests of OPTPOD2. Transatlantic help from Hodge Worsham at Yale was extremely useful with this project. I am also grateful to the Electron Microscope Suite here at the Open University for their analysis of my thin-films.

The distributed current analysis technique used in chapter 4 was developed by Andy Ioannides and Rob Hasson and I am extremely grateful for their help and patience in explaining details of the method, many of which must have seemed simple to them. It is fair to say that the emergence of such techniques is moving biomagnetism into a very exciting area and so I am especially grateful to Andy for giving me the opportunity to move into this work. I hope that some of his enthusiasm and energy might rub off on me!

The evoked response experiment was carried out at the Helsinki University of Technology and I am very grateful to Risto Illmoniemi and Seppo Ahlfors for their hard work (both as experimentalists, subjects and guides to Finland!).

The expert system outlined in chapter 5 was programmed in PROLOG by Dr Niall Palfreyman and I would like to thank him for many lively discussions we had on this novel approach to the inverse problem. I should also thank Steve Daniels and Marilyn Moffat in ACS for their help and advice about the VAX, and the UNIRAS graphics libraries. The specimen MR images used in the description of the IMAGE software tool were taken at The University of Texas Medical Center in Galveston.

Special thanks must go to Steve Swithenby for his good humored patience and understanding as my supervisor. I can think of only one thing more tedious than re-drafting a chapter four times, and that is having to read it for corrections four times. Thanks, Steve.

I owe a special debt to my friends (including the people above) who although they might not have understood what was driving me mad ('I only put it in Acetone for 30 seconds and the WHOLE circuit dissolved...') certainly kept me going. I should make a special mention of Helen, John and Squeak Colleran, who not only put up with me more than most (by virtue of their close proximity!) but were kind enough to lend me their spare room when I needed somewhere to stay. It would take too much space to thank everybody else, but you know who you are!

Finally I'd like to thank my parents Shiv and Edna, and my brother and sister; Narvin and Shari. Oh, and Ben the dog.

Contents

List of Figures

Chapter 1

Introduction

1.1 Biomagnetism: An historical overview

Biomagnetism is based on the measurement of the magnetic fields generated by living systems. The pioneering measurement was made by Baule and McFee in 1963 [1]. They were able to detect the magnetic field of the human heart, using several million turns of copper wire on a ferrite core. For researchers working in 1991, with 37 channel systems using superconducting electronics, it is hard to believe that these initial measurements were treated with great scepticism by other scientists. Cohen, another pioneer in the field, noted in 1982 [2]

> ...in 1965, when I was building my first shielded room for biomagnetism, I saw one day that a large time-varying magnet was being installed in the very next lab; its field would easily penetrate my shielding. When I complained to the appropriate officials, they responded that biomagnetism was absurd and that I would never detect anything in any case, so why bother moving the magnet?...

Despite the attitude of his colleagues, Cohen and others persevered with biomagnetism research throughout the late sixties. In the last few days of 1969, biomagnetism as we know it today was born, with the first measurement of a biomagnetic signal using the SQUID.

The SQUID or Superconducting Quantum Interference Device utilizes an effect predicted by Josephson in 1962 [3]. He predicted that electrons could tunnel across a normal junction between two superconductors, and that this tunnelling constituted a current. Additionally, because of the phase properties of the electron wavefunctions, this current would be affected by an applied magnetic field. In 1963 at the Ford Scientific Laboratory there began a series of experiments into superconductor behavior which would culminate in the development of the rf-SQUID [4]. The rf SQUID consists of a loop of superconductor containing one Josephson junction. It is an extremely sensitive detector of magnetic flux: changes as small as 10^{-6} flux quanta are detectable. As one of the researchers at Ford, Jim Zimmerman, reported in 1987 [7].

> ...in an experiment on Nuclear Magnetic Resonance they [John Lambe and colleagues] noted that the X band impedance of a bit of superconducting thin film varied periodically as a function of the dc magnetic field in the neighborhood. The periodicity of the variation was in the neighborhood of one or two nanotesla- it must have been obvious that they had a magnetic

> field sensor of unparalleled sensitivity...I was consulted for suggestions as to the fundamental nature of the phenomenon...I was able to shed not the faintest glimmer of light on the subject...

Over the next few years the Ford group made the connection with Josephson's theory and Zimmerman developed the design of first the rf biased SQUID and then the double Josephson junction dc-SQUID.

Coincidentally both Cohen and Zimmerman were funded by the US Navy. The scientist in charge of these two projects at the Office Of Naval Research, Edgar Edelsack, soon realised that the SQUID would be useful in biomagnetism. The SQUID project was being funded by the Navy with a view to possible submarine detection (a promise which has never been fulfilled). Edelsack arranged a collaboration with the two groups and at the end of 1969 the first magnetocardiogram was recorded at MIT, with Zimmerman as the subject. The first attempt at measuring a brain signal, with Edelsack as the subject, was not as successful:

> ...I undressed down to my shorts, entered the room and with some trepidation placed my head close to the tip of the dewar..I wondered what would happen if the dewar broke and spilled helium all over me. Time seems infinitely long when you're trying to hold your head steady near the tip of a helium dewar...finally the door opened...From the look on their faces, I got the message. They didn't think that there was anything wrong with Jim's SQUID detector. The trouble they believed, was that there was no signal emanating from the source...

Anybody who has had experience of being a subject in a biomagnetic brain measurement will recognize all the feelings that Edelsack had in the MIT shielded room. With another subject and a more sensitive SQUID magnetometer, the first Magnetoencephalogram (MEG) was recorded in 1972.

All these measurements used a simple SQUID magnetometer, and relied on heavy magnetic shielding (and some co-operation from Cohen's next door neighbours) to be able to detect the tiny magnetic fields generated by the body. The next advances in instrumentation were in the development of gradiometric techniques i.e the measurement of spatial gradients of the magnetic field, to reduce the sensitivity to distant noise sources. In Baule and McFee's original measurement, they used two solenoid coils wound in opposition to detect the heart signal. This approach was extended to SQUID magnetometers by using external superconducting pickup coils, wound in opposition. The supercurrent in these coils is proportional to the external magnetic field gradient, and is coupled into the SQUID loop using a small coil in series with the pickup coils. The first biomagnetic measurement using a gradiometer in an unshielded environment was carried out in New York (surely one of the most magnetically noisy places in the world) in 1977. This gradiometer was a second order device (i.e it measured the second spatial derivative of the field).

After this, the basic technology for biomagnetism was in place. The most sophisticated systems now have 37 channels, using first order gradiometers, in a single dewar. They enable the magnetic field to be sampled over a large area of e.g. the head, every few milliseconds.

In the 21 years since the first SQUID measurement the techniques of analysis of biomagnetic signals have proceeded rather slowly. It was soon realised that measuring the magnetic

field produced by the brain had some advantages over the clinically widespread Electroencephalography (EEG), in which the electric field was measured using scalp electrodes. The information contained in the EEG is distorted by the varying conductivity geometries of the brain, scalp and skull, with the result that it is sometimes difficult to locate the primary current sources generating the EEG within even the correct hemisphere. The magnetic field is not distorted to the same extent, but the calculation of the current distribution that has generated the measured magnetic field (the so called inverse problem) is difficult. Up until the last half of the 'Eighties, the problem was 'solved' by modelling the generating sources as a single, highly localised current source known as a current dipole. The inverse problem was solved by finding the current dipole which best fitted the magnetic field. If the source current density is reasonably localised then the current dipole is a useful way of summarising the activity, however in a lot of cases it is a hopelessly simplistic model. Recently, more sophisticated inverse problem methods are beginning to appear which hold out the possibility of creating 3-d current density images of brain activity [38].

Initially, there were two areas of application in which it was hoped that biomagnetism would make an enormous contribution - basic biological research and clinical diagnosis. Even though over 20 years have past, it is fair to say that progress has been rather disappointing in both respects. The reasons for this are many and varied, but none are fundamental or insurmountable. Firstly, the measurements are difficult and expensive; the new multichannel systems cost millions of pounds to buy and maintain. Secondly, the rather simplistic modelling techniques mentioned above have precluded the gaining of really fundamental insights into how the brain works. The new imaging techniques being developed should go a long way towards solving this problem. Thirdly, as far as clinical applications go, there is an inherent (and probably healthy) conservatism amongst clinicians; those that know about biomagnetism are interested but are waiting to see if it turns out to be as useful as we physicists promise. This is fine, but it illustrates nicely the final problem that has probably slowed down the application of biomagnetism i.e it is by necessity an inter-disciplinary research area. When physicists, engineers and clinicians do work together successfully (such as on the accurate location of epileptic foci [50]), biomagnetism has shown itself to be a useful technique.

Will biomagnetism eventually provide information that cannot be gained from other techniques? Over the last few years it has become clear that there is a promising niche. Firstly biomagnetism provides non-invasive, functional information. By functional information we mean information which shows which structures in, for example, the brain are being activated, and in what sequence. Other clinical techniques such as X-rays are invasive, and provide structural rather than functional information. EEG does provide functional information and is non-invasive (although the author can testify that the attachment of EEG electrodes can seem very invasive). However, because of the conductivity distortions mentioned above, the spatial accuracy of EEG is very bad, and even worse, if an exact conductivity profile of the head is not known (and it never is), the spatial accuracy is un-

predictable. Another clinical technique which is compared to MEG is Positron Emission Tomography or PET. In PET, a radioactive source is introduced into the subject's body. The source is such that it preferentially accumulates in regions of the body that are metabolically active. If one particular part of the brain is more active than another, then it will become more radioactive. Using detectors around the head, a functional image of the brain activity can be gained. Although the spatial accuracy is very good, it takes minutes for enough of the source to be metabolised to provide an image. This means that PET can never compete with the millisecond time resolution offered by MEG.

So biomagnetism has a niche in providing non-invasive, functional information with reasonable spatial accuracy (of the order of a cm), with excellent time resolution. It remains to be seen whether the window it provides on biomedical processes is big enough to justify the time, effort and money needed to provide a clear view.

1.2 Biomagnetic systems - a summary of the thesis

This thesis is concerned with two aspects of the design and operation of biomagnetic systems. In many ways the work that we present here has been developed in specific response to the needs of our laboratory and the collaborations we undertake with other groups, however in many instances we hope there are general lessons to be learned about the optimal design of future systems.

Figure 1.1 shows a schematic diagram of a complete biomagnetism system. The arrows show information flow within the system, where we define information to be anything that conveys the position, strength and orientation of the current density within the living system under study.

The two main areas that we will consider in this thesis are the optimal design of the magnetometers, and the software tools that are a necessary part of the data analysis and inverse problem sections of the system. Although these two areas might seem only loosely connected, we shall see later that the design of the magnetometers may have important consequences for the data analysis and inversion stages of the system.

Magnetometer design

In designing a biomagnetic system there are two major hurdles that must be overcome. Firstly, the signals are extremely small (less than 10^{-13} Tesla for brain activity), and we must use instrumentation capable of detecting them. The only device currently available with enough sensitivity for the task is known as a SQUID (Superconducting Quantum Interference Device). The basic properties of the SQUID are described in the first section of chapter 2, but it is essentially a very sensitive flux to voltage converter. To increase the flux sensitivity of the magnetometer external superconducting pickup coils can be used, which couple flux into the SQUID using a circuit known as a *flux transformer*. Figure 1.2 shows a schematic of a single magnetometer channel. The second problem that has to be

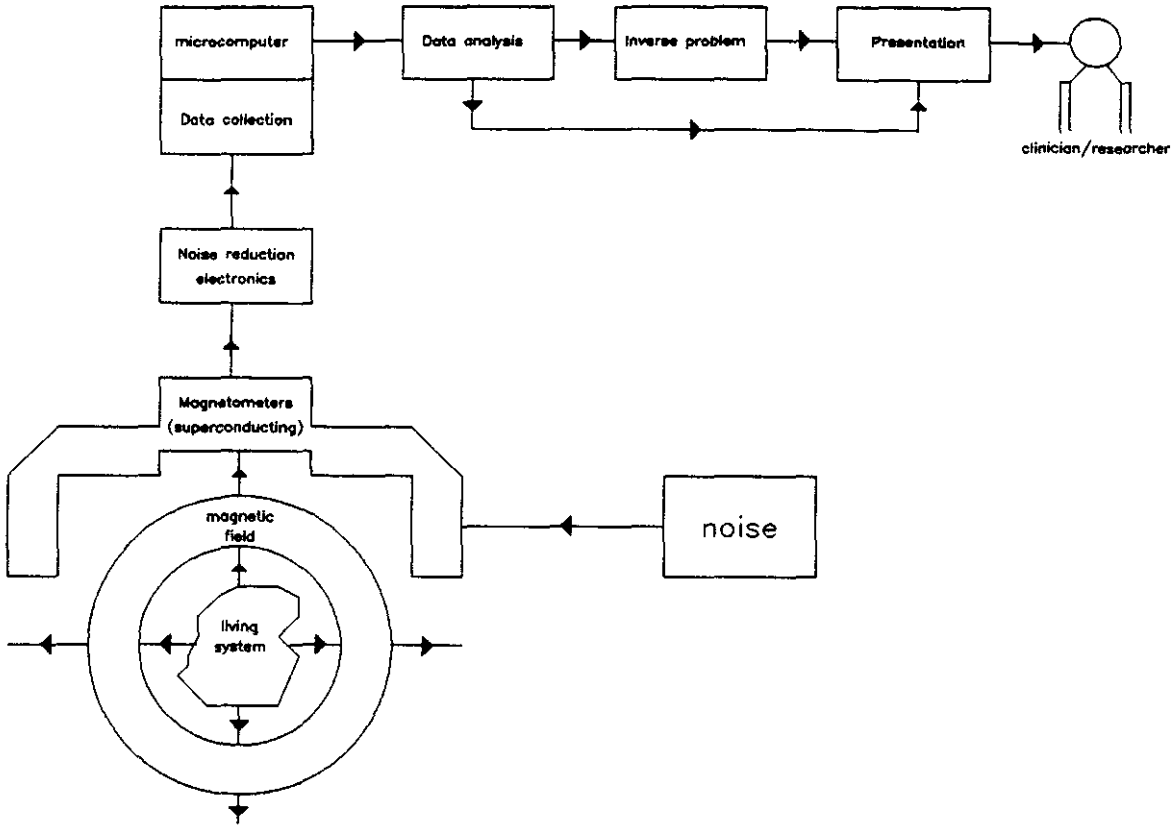

Figure 1.1 A biomagnetism system

solved is the fact that the field noise is several orders of magnitude greater than the signals themselves. This can be seen in figure 1.3. The simplest way to alleviate this problem is to use careful magnetic shielding. This is very expensive however, and does not get rid of subject noise (for example heart artefacts can be a problem in brain measurements). Instead, most groups have adopted the *gradiometer* as a means of reducing noise. The gradiometer is a specific type of flux transformer, in which one or more sets of coils in the circuit are wound in opposition. The final device is then insensitive to the first terms in the Taylor series expansion of the field at the measurement site and gives an output which is proportional to a specific spatial gradient of the magnetic field. As most noise sources are effectively spatially uniform, the gradiometric process preferentially discriminates in favour of close signal sources. The concept of the flux transformer and gradiometer circuits are introduced more thoroughly in chapter 2.

Depending on the construction details, gradiometers can be designed to measure many different gradients of the magnetic field vector. In the final section of chapter 2 we look at the types of gradiometer that can be constructed, and look qualitatively at what implications each design has on our ability to reconstruct the current density from the magnetic field measurements. We construct in simulation gradiometers measuring all the possible field gradients up to second order, and look at the signals that are generated as the gradiometer is scanned in a plane above a small element of current. The results show that the 'shape' of

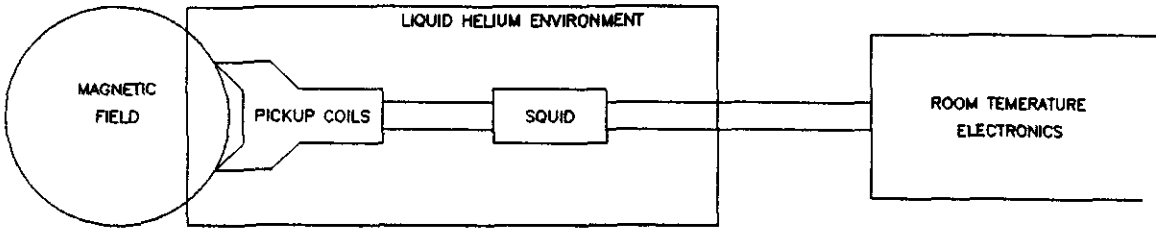

Figure 1.2 A single magnetometer channel.

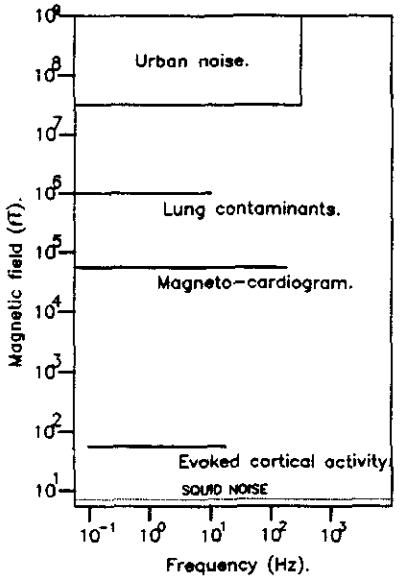

Figure 1.3 Typical biomagnetic fields and noise.

the signal maps produced vary in complexity and that this may make certain gradiometers better suited to inverse problem techniques which work by recognising spatial patterns within such signal maps.

In chapter 3 we look more closely at one aspect of gradiometer optimisation; *forward problem optimisation*. The forward problem consists essentially in calculating what signal a gradiometer will produce in response to some test current distribution. In forward problem optimisation we are therefore trying to maximise the signal that a gradiometer will produce. In the first section of the chapter we look at the various algorithms which we have developed in order to simulate any gradiometer geometry. These include flux calculation algorithms and inductance calculations. One important parameter that must be calculated is the *balance* of the gradiometer. If, for example, a second order gradiometer is designed so that it is completely insensitive to uniform fields and first order gradients, we say that it has perfect intrinsic balance. For the most commonly used gradiometers, made from sets of discrete co-axial coils, the calculation of this intrinsic balance is simply a matter of making sure that the weighted sum of the areas of all the coils in the device is zero. However in general the calculation of this parameter is not as simple as this, so in this chapter we derive some expressions which allow the calculation of the intrinsic balance for any arbritrary shaped

gradiometer.

In the next section of chapter 3 we list some of the parameters that are useful in characterizing the forward problem performance of a gradiometer. These include the sensitivity of the device to particular gradients and current sources, measures of the ability of the device to reject noise sources, and a parameter which quantifies the spatial resolution of the gradiometer.

In this thesis we are mainly concerned with planar gradiometers. These are fabricated on flat substrates or winding formers and hence take up only a fraction of the volume that more bulky devices need. This enables many more channels to be placed in the same dewar space. In the final part of chapter 3 we present a numerical algorithm for choosing the gradiometer with the best forward problem characteristic. This algorithm was developed to help us in the design of a new magnetometer system under construction at The Open University, which uses three planar gradiometers. A numerical approach was chosen as this allows design constraints (such as available dewar space) to be easily incorporated into the optimisation.

Planar gradiometers can be fabricated using conventional superconducting wire wound onto flat formers, or using thin film fabrication techniques with niobium thin films patterned on a silicon substrate. In chapter 7 we present the results of an attempt to fabricate a thin film gradiometer. The gradiometer was designed using the numerical optimisation algorithm described above. Although the device was constructed in the correct geometric form, it was not superconducting. This illustrates quite nicely the problems that have to be overcome if the promised multi-channel systems using thin film gradiometers are to appear in the near future. At the moment even the most sophisticated biomagnetic systems still use wire-wound gradiometers (or thick-film devices), but as experience in the construction of superconducting thin-film devices grows, this is likely to change. Thin film devices are desirable in that they can, in principle, be constructed in large numbers with very highly reproducible characteristics and with a high intrinsic balance.

In chapter 4, we extend the characterization of gradiometer performance from the forward problem, to the inverse problem. The inverse problem is essentially the calculation of the generating current distribution, given the magnetic field measurements. Sophisticated inverse problem techniques have recently been developed which calculate the most probable current density distribution throughout an entire 2 or 3 dimensional region of space. One such approach, developed by researchers here at the Open University is outlined in the first section of chapter 4. This technique, at least in principle, should work with any type of gradiometer, and this is empirically tested in the final part of this chapter. We look at the ability of four different multi-channel systems, using three different types of gradiometer, to recover a simulated current distribution using the distributed current analysis technique. The results seem to support the hypothesis that the actual gradiometer type is not as important as the physical distribution and number of gradiometers. If too few gradiometers are used, spaced by too great a distance, then significant errors will occur in the solutions.

Software tools

One of the consequences of the use of multi-channel systems and sophisticated current density imaging techniques is that the amount of data that needs to be analyzed and assimilated by the operator is now very large. This problem is even more significant when we remember that we hope eventually for biomagnetism to enter routinely into the clinical environment. There is a great need therefore for the development of comprehensive 'user-friendly' software tools to assist in the analysis process. In chapter 5 we describe four such tools that have been developed to meet specific needs in our analysis of biomagnetic data. Computer graphics play an important part in all of them, but it is a mistake to regard this as simply a matter of 'pretty' presentation. The choice of appropriate graphical representations for the information contained in the distributed current images described in chapter 4 plays an important role in 'distilling out' the pertinent information from the complete data set [5,6].

The first tool we describe, DataView was designed to enable the user to graphically view the magnetic field data (as scans or contour plots) from a multi-channel system, immediately after it has been collected in the laboratory. It also allows the user to software filter the data if appropriate. This viewing of the signal data before inversion is essential as it can give the user an indication of the presence of significant noise events in the data, or of systematic problems with noise in a particular channel.

The second software tool, GCL, was developed as a comprehensive system for producing contour maps (or other appropriate representations) of data. The data may be magnetic field data or current density solutions. It can be used interactively by the user, or other programs can use its facilities.

The final two systems that we shall present in this chapter both address the problem of finding *active regions* within the brain. These are small parts of the entire current density space which have a relatively large and localised current density, and in the future we hope to be able to match the location of these functional regions to specific brain structures.

The first tool, ABIS, models these regions as a set of current dipoles, and then uses some pattern recognition ideas to identify and locate these dipoles. It works by analyzing a 'map' of magnetic field data over some area (for example the back of the head) and then treating this map as an image which can be analysed to locate the current dipoles. The process is controlled by an expert system which uses a rulebase to tell it how to find the dipoles. We present the basic principles behind the dipole location process, and comment on the accuracy and limitations of the method. It is interesting to note that as it is essentially a pattern recognition process, some gradiometers are better suited to the method than others.

The second tool, IMAGE, was developed to analyze and summarise the very large amount of information contained in the distributed current density images. The problem here is that the sources may range over a 2D disk, or a 3D cylinder, and typically, there will be a different solution every few milliseconds. As an experiment may run for several hundred milliseconds, there might be several hundred disks or cylinders that have to be analyzed. Initially, video animations were produced which gave a good global view of the solutions as they changed

in time. However, both the level of interaction available to the user, and the amount of quantitative information that he/she can extract from video are limited. IMAGE allows a variety of graphical 'investigations' of the entire solution set to be made, under full control of the user. The main use of IMAGE is in the location of active regions, and the analysis of how the activation within these regions varies in time. IMAGE also allows the inclusion of graphical information from structural imaging techniques such as MRI. In the final part of chapter 5 we describe the various representations that IMAGE can produce.

Documentation of the full capabilities of all the software tools described in chapter 5 can be found in appendix B.1.

An application: A visually evoked experiment

In chapter 6 we describe an experiment in which many of the ideas discussed in the rest of the thesis are put to real use.

The only multi-channel system in operation at the present time which uses planar gradiometers is the 24 channel system at the Helsinki University of Technology. This is one of the systems that we tested with the distributed current inversion technique in chapter 4.

We performed an experiment using this system which involved stimulating the left and right visual fields of a normal subject with a reversing checkerboard pattern. It is known that the visual cortex has a retinotopic map i.e information from different areas of the visual field stimulate neuronal populations in different parts of the visual cortex. We hoped with this experiment to investigate this retinotopic property.

In the first part of chapter 6 we describe the basic properties of the human visual system, and then go on to describe the philosophy behind the *evoked response* measurement. In an evoked response experiment a well characterized stimulus is presented to a subject with the aim of eliciting a response in the brain. The three specific stimuli we used were the reversal of an octant in the left field of view, one in the right field of view and then both octants reversing together.

In the next section we describe the experimental protocols that were used in the experiment. The data were inverted using the distributed current analysis technique, and IMAGE was used to find the active regions within the solution set. Using this approach we were able to show that the active regions for the left and right octant reversals were on opposite sides of the visual cortex and, as predicted, it was a contralateral response i.e the left stimulus provoked a response on the right visual cortex and vice-versa. We then looked at the time variation of the activity in each region, and found that this was very similar for both regions, with the activity arriving at around 100ms after the stimulus, decreasing over a 30-40ms period, and then reappearing at the initial site around 60-80ms after the initial response. We remark briefly on how this may fit in with some theories of brain function. Finally we were able to show that for up to around 200ms, when both responses were strong, the response to both octants reversing was very close to the linear sum of the response to the two individual octants.

Chapter 2

Use of gradiometers

In this chapter we describe the basic principles and techniques involved in measurement of biomagnetic signals. The heart of the magnetometer system is a superconducting device known as a SQUID, and in the first section we describe some of the important features in SQUID operation. Although the SQUID is a highly sensitive magnetic flux detector it is rather small, and intercepts only a small amount of flux. External pickup coils are used to trap more flux and couple it in to the SQUID.

These *flux transformer* circuits are described in the second section of this chapter. The major advantage of using flux transformers is that the coils can be wound so that the device is sensitive to some spatial gradient of the magnetic field. This specific type of flux transformer is known as a gradiometer and is more insensitive to environmental noise sources. In the final sections of this chapter we describe some of the important issues in gradiometer design, and look at how the chosen gradiometer geometry affects the sensitivity of the device to particular current sources.

2.1 The SQUID

At the heart of almost every magnetometer used for biomagnetism is a device known as a SQUID, or Superconducting Quantum Interference Device. In this thesis SQUID operation is only briefly described. More thorough treatments of this subject are readily available [10,29,30,58] .

The SQUID consists of a ring of superconducting material with one or two weak links (known as Josephson junctions) fabricated into the loop. In a fully superconducting loop there is phase coherence and this leads to the flux quantization relation

$$\Phi = n\Phi_0 \tag{2.1}$$

where Φ_0 is the flux quanta and is equal to 2.07×10^{-15} Webers, Φ is the total magnetic flux within the loop, and n is an integer. If an external magnetic flux Φ_{ext} is applied to the loop, a screening current i_s will flow which maintains the original flux state of the loop

$$\Phi_{ext} + Li_s = \Phi \tag{2.2}$$

where L is the self-inductance of the loop and as the flux must be quantized,

$$\Phi_{ext} + Li_s = n\Phi_0 \tag{2.3}$$

If we introduce a single Josephson junction into this loop then there is a phase change across the weak link. Josephson found that the electron pairs can tunnel across the weak link, and this tunnelling constitutes a current, i_j, which induces a phase change θ in the superconducting wavefunction across the junction such that

$$i_j = i_c \sin\theta \tag{2.4}$$

where i_c is the maximum current that can flow, and is known as the critical current for the junction. The phase change means that flux within the loop is no longer exactly quantized, and we have a new flux relation

$$\Phi = \Phi_0(n - \frac{\theta}{2\pi}) \tag{2.5}$$

Rearranging for θ and substituting into equation 2.4 (with n=0 for simplicity)

$$i_j = -i_c \sin(\frac{2\pi\Phi}{\Phi_0}) \tag{2.6}$$

This current is able to screen external flux and so we can write down a modified version of equation 2.2

$$\Phi_{ext} - Li_c \sin(\frac{2\pi\Phi}{\Phi_0}) = \Phi \tag{2.7}$$

This kind of single Josephson junction device is known as an rf SQUID and is usually designed so that $2\pi Li_c > \Phi_0$. In this case the Φ/Φ_{ext} curve is multi-valued and, if applied flux were to vary in a periodic way with sufficient magnitude, hysteresis losses would occur. Figure 2.1 shows the form of this curve for $Li_c = 1.25\Phi_0$. The dotted lines show a typical hysteresis path.

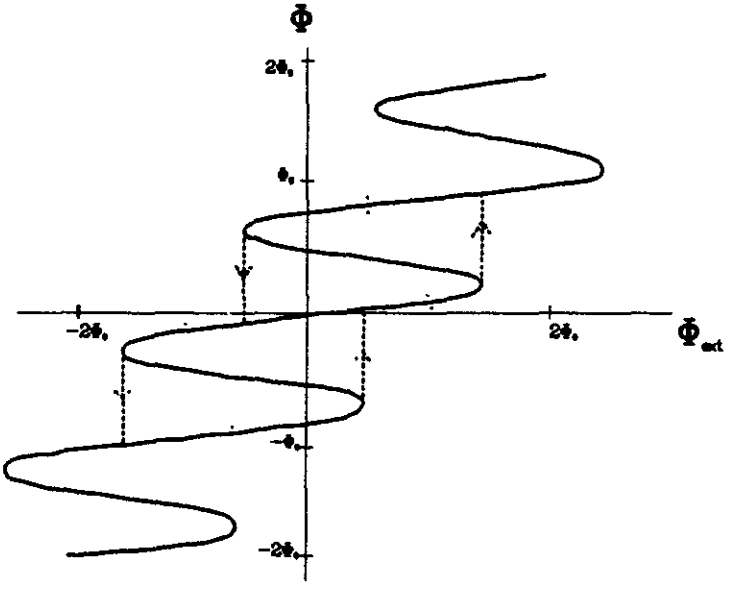

Figure 2.1 Flux in rf SQUID loop versus applied flux, for $Li_c = 1.25\Phi_0$.

The normal mode of operation for an rf SQUID uses this hysteresis property. An external tank circuit superimposes an rf bias flux on the signal to be measured. The energy losses

that occur in the tank circuit will depend on the rf bias *and* the signal flux, and manifest themselves as a varying rf voltage in the tank circuit. The relationship between this rf voltage and the signal flux is periodic and non-linear, so a phase sensitive detector is usually used to linearise the output voltage. In this flux locked mode, the detected signal is fed back to the SQUID to keep the detected rf voltage constant, i.e the flux oscillations in the SQUID remain centred on the same part of the Φ/Φ_{ext} curve. The resulting rf voltage then depends linearly on the signal flux

$$\Delta V \propto \Delta\Phi_{signal} \tag{2.8}$$

In the dc SQUID, there are two Josephson junctions. This type of SQUID is biased with a dc current rather than an rf signal, but the detection electronics also use a flux-locked mode to linearise the response, and the resultant voltage-flux relation is the same as the rf SQUID. Dc SQUIDs are becoming more prevalent in biomagnetism because their noise performance is significantly better than rf SQUIDS. This is partly because the intrinsic noise level of the SQUID is lower in the dc SQUID, but noise also originates in the first stage of amplification and the noise in dc amplifiers is significantly lower than that in rf amplifiers.

Intrinsic noise in SQUIDS can be expressed as a flux value within the SQUID loop i.e. there is some minimum value of signal flux S_n which will give a signal to noise value of 1 in the SQUID. For commercial dc SQUIDs a typical value for this will be $8 \times 10^{-6}\Phi_0/\sqrt{\text{Hz}}$, which is an order of magnitude better than typical rf SQUID noise levels. In designing magnetometer systems we must always be aware of these values, as they set an absolute limit for the kind of current sources we might hope to detect with our system. In practice, we are more likely to be limited by environmental noise (or even subject noise) than the intrinsic SQUID noise.

Josephson junctions can be fabricated using several techniques and the highest quality SQUIDs manufactured at the moment are dc SQUIDS entirely fabricated using thin-film techniques.

To summarise, SQUIDs can be used as very sensitive flux to voltage converters with flux sensitivities of the order of $10^{-5}\Phi_0$. Although it is possible to use a SQUID directly to measure the magnetic field, magnetic flux is usually collected in a larger set of pickup coils and is coupled via a superconducting circuit into the SQUID loop. The SQUID itself is surrounded by a superconducting shield which stops external magnetic flux from penetrating the SQUID loop. Such a circuit is known as a flux transformer. There are two reasons for this approach; firstly, the larger pickup coils will trap more flux and funnel it into the SQUID. Secondly, by winding the pickup coils in opposition, the flux transformer can be made sensitive only to spatial gradients of the magnetic field. This makes the magnetometer system less sensitive to noise sources.

In the next section we look at the design and use of a general flux transformer circuit.

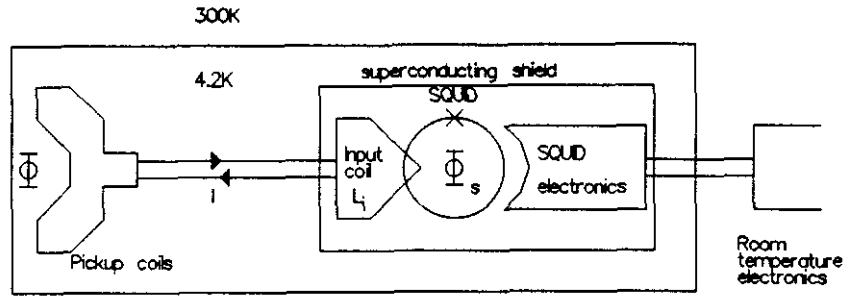

Figure 2.2 Schematic diagram of a flux transformer.

2.2 Flux transformers

Figure 2.2 shows a schematic diagram of a flux transformer. External magnetic flux links the pickup coil arrangement and produces a shielding current in the superconducting circuit. This current is carried by superconducting wires into the superconducting shield containing the input coil and the SQUID. If there are n pickup coils in the flux transformer, the current is given by

$$I = \frac{\sum_{k=1}^{n} \Phi_k}{L_{input} + \sum_{j=1}^{n} L_j} \tag{2.9}$$

Φ_k is the flux through the kth pickup coil, and L_j is the self inductance of the jth coil. L_{input} is the self inductance of the SQUID input coil. Note that any small inductance that the leads connecting each coil might have is considered negligible and, to minimise this inductance, the wires are usually made into twisted pairs.

The current I produces a flux Φ_{SQUID} in the SQUID loop which is given by

$$\Phi_{SQUID} = MI \tag{2.10}$$

where M is the mutual inductance between the input coil and the SQUID loop and is given by

$$M = K\sqrt{L_{SQUID}}\sqrt{L_{input}} \tag{2.11}$$

K is a geometric constant expressing the strength of coupling between the SQUID and the input coil. Substituting equation 2.9 and 2.11 into equation 2.10 we get

$$\Phi_{SQUID} = K\sqrt{L_{SQUID}}\sqrt{L_{input}}\frac{\sum_{k=1}^{n} N_k\Phi_k}{L_{input} + \sum_{j=1}^{n} L_j} \tag{2.12}$$

Note that the term N_k has been introduced into the equation to allow for the fact that each of the pickup coils can have more than one turn i.e. N_k is the number of turns on the kth coil.

The above equation defines the response of any flux transformer circuit and in designing the magnetometer we should maximise the above function. Note that the output voltage of the system is linearly proportional to Φ_{SQUID} (see section 2.1) and so all the simulation and optimisation procedures described later will use Φ_{SQUID} as the function to be studied.

The SQUIDs that we use are commercially made and have fixed values for K, L_{SQUID} and L_{input}. This means that magnetometer design consists of defining the geometry of the external components i.e. the pickup coils. If we differentiate the Φ_{SQUID} function with respect to L_{input} and set this function to zero we find a maximum with respect to L_{input} when $L_{input} = \sum_{j=1}^{n} L_j$ [58]. This is only one of the parameters which we can choose to look at and its importance should not be overstated. However it turns out that the optimum flux transformer circuits which have been designed in chapter 3 do tend to have pickup coil geometries which are very close to obeying the above condition.

If we simply wanted to measure the magnetic field, all we would need would be a single pickup coil. However, this arrangement would be good at picking up noise sources as well as the target signal. To reduce this problem, a special type of flux transformer known as a gradiometer is used.

2.3 Gradiometers

2.3.1 Measurement of spatial gradients

The magnetic field from some arbitrary source will have a complicated spatial form, but the magnitude of the field will generally fall off with distance from the source according to a simple power law

$$B \propto \frac{1}{r^n} \tag{2.13}$$

Where B is the magnitude of the magnetic field and r is the magnitude of the distance to the source. Using this equation we can write down the ratio of the measured field B_s generated by a near signal source, and the field B_n generated by a distant noise source i.e a 'signal to noise' ratio

$$S = \frac{B_s}{B_n} = (\frac{r_n}{r_s})^n \tag{2.14}$$

If we were instead to measure a spatial gradient of the field $\frac{\partial^q B}{\partial r^q}$ then this ratio becomes

$$S = \frac{\frac{\partial^q B_s}{\partial r^q}}{\frac{\partial^q B_n}{\partial r^q}} = (\frac{r_n}{r_s})^{n+q} \tag{2.15}$$

So measuring a spatial gradient of the field increases the noise rejection performance (as assessed by the above ratio) by a power of q. A first order gradiometer (a flux transformer which measures an approximation to the first spatial derivative of the field) is shown in figure 2.3. The coils in this gradiometer measure the z component of the field and are wound in opposite directions. If a magnetic field with uniform z component was applied to this device, the resulting signal would be zero. If a field with $\frac{\partial B_z}{\partial x} \neq 0$ was present then there would be a non-zero signal flux in the SQUID. This signal flux can be expressed using equation 2.12

$$\Phi_{SQUID} = K\sqrt{L_{SQUID}}\sqrt{L_{input}}\frac{\Phi_A - \Phi_B}{L_{input} + L_A + L_B} \tag{2.16}$$

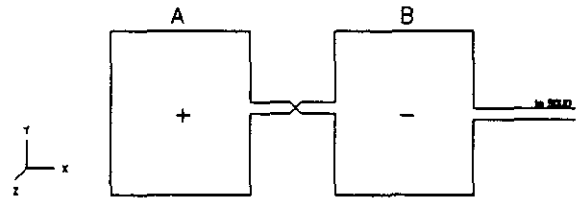

Figure 2.3 A first order gradiometer.

Note that information about the winding sense of the coil is contained in the N_k term of equation 2.12, i.e. $N_A = +1$ and $N_B = -1$. Also note that we have neglected the mutual inductance between each coil. This is a valid approximation if the coils are separated by a reasonable distance.

Gradiometers are supposedly circuits for measuring spatial gradients of the field. In fact this is only true if the source is a long way from the gradiometer, compared to the *baseline* (the distance between each coil in the gradiometer). When this condition is met we have the equivalent to setting $dx \rightarrow 0$ in a simple differential i.e. we are measuring the gradient. Then the gradiometer can be said to be measuring the following

$$V = \sum_{n=1}^{\infty} \sum_{i=x,y,z} \sum_{j=x,y,z} C_{ijn} \frac{\partial^n B_i}{\partial r_j^n} \tag{2.17}$$

This is the general equation, with C_{ijn} being a constant defined by the geometrical design of the gradiometer, and the inductances in it. All the coils in the gradiometer are considered to be at the same point in space, $\vec{r}$. Usually a gradiometer has only one value of each of i, j and n. For example if a gradiometer was sensitive to the second order of B_z, differentiated with respect to z, then $C_{i,j,n}$ would be non-zero only for i=z, j=z and n=2. So, in nearly all practical cases, the response can be written as

$$V = C_{ijn} \frac{\partial^n B_i}{\partial r_j^n} \tag{2.18}$$

Until recently, most gradiometers used in biomagnetism have been second order gradiometers measuring $\frac{\partial^2 B_z}{\partial z^2}$. The design of such a device in use at the Open University, the SHE gradiometer, is shown in figure 2.4(a). This particular device is known as a symmetric gradiometer because the two baselines are the same and the 3 coils have the same radius. Another second order axial gradiometer designed here at the Open University is known as SQUIDLET and is shown in figure 2.4(b). This gradiometer was designed with a very small bottom coil to improve the spatial resolution of the device, and is used for investigating the signals from small developing organisms [49]. To balance the gradiometer it is necessary to have many more turns on the small bottom coil. SQUIDLET is an asymmetric second order axial gradiometer.

It should be noted that these so called axial gradiometers need large winding formers of volume $\pi r^2 2d$ where r is the radius of the coils and d is the baseline. For the SHE gradiometer this volume is around 30 cm^3. Planar gradiometers can be constructed to occupy much less volume. A comparable thin film device would occupy around a third of the space.

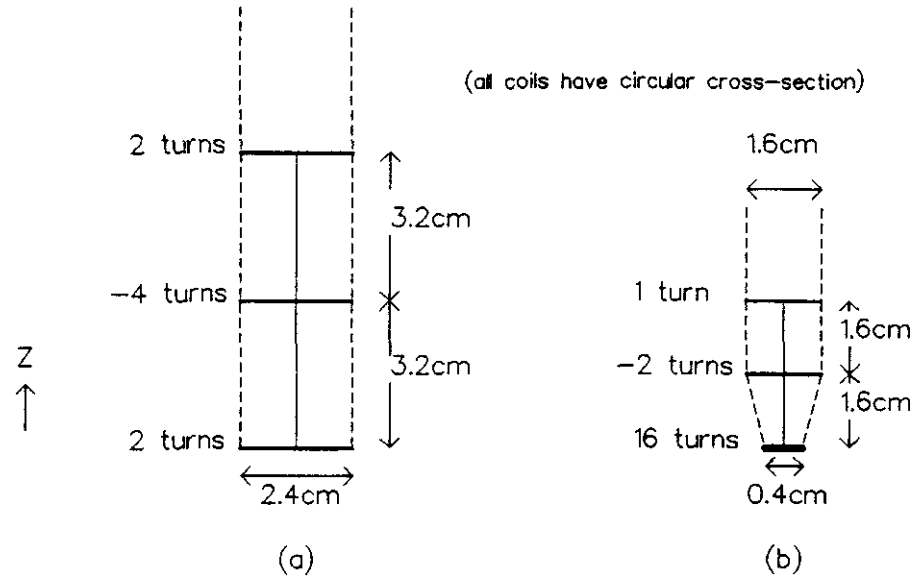

Figure 2.4 Side view of the SHE and SQUIDLET gradiometers

In planar gradiometers we have a qualification to equation 2.18 because it is impossible to construct a planar device which differentiates along the same direction as the field component being measured. So the sensitivity can be written as

$$V = C_{ijn} \frac{\partial^n B_i}{\partial r_j^n} \qquad (i \neq j) \tag{2.19}$$

These devices are known as 'off diagonal' gradiometers because of the $i \neq j$ condition.

Devices which measure third order gradients [23] have been constructed but the general trend has been to lower order gradiometers as screened rooms and noise-rejection techniques become more prevalent. Here at the Open University we do not have a screened room at the moment so the presently operating systems use second order gradiometers.

It is worth emphasizing that a practical gradiometer will only have a response that can be modelled by the above equations for far-away sources. When the source is near to one or other of the coils the response is more complicated and the gradiometer must be fully simulated by calculating all the parameters in equation 2.12. The algorithms for doing these calculations are described in chapter 3.

2.3.2 Balancing

To be useful as a device for noise rejection, the gradiometer must be field balanced i.e. the areas of the coils must be defined such that there is no sensitivity to uniform field. In the gradiometer shown in figure 2.3 the area of coil A should be equal to the area of coil B.

Secondly, the gradiometer must be *gradient balanced.* This means that an n_{th} order gradiometer must give a zero response to all constant gradients of order $n-1$ or less. For a second order gradiometer this means there must be no signal resulting from a constant first-order gradient.

In practice it is impossible to manufacture devices such that the balance is perfect, especially when the gradiometers have been hand wound.

There are several ways to deal with this intrinsic imbalance. Firstly, if the measurements are carried out in a magnetically shielded room, it can be ignored. This might be appropriate if the background magnetic field is so weak that it does not matter if the gradiometer has a slight sensitivity to it. Secondly, the balance can be corrected post-measurement by electronic subtraction of a fraction of the noise field [52]. This requires separate flux transformer circuits which, rather than being gradiometers, are simply coils which measure the field. A fraction of the output from these circuits is then subtracted from each of the gradiometer circuits. The subtraction can be carried out using electronics or digitally using a computer. Thirdly, the gradiometers can be manufactured using thin-film techniques which are potentially much more accurate than hand winding the gradiometers. Thin-film gradiometers are limited to being planar devices i.e. they must be fabricated on a two-dimensional substrate. In chapter 7 the design and construction of a test thin-film gradiometer is outlined.

Finally it is possible to mechanically perfect the balance using small 'trim-tabs' of, for example, lead. Lead is a superconductor and as such will deflect magnetic flux lines when it is cooled below 4.2K . By moving the trim-tabs relative to the coils in the gradiometer it is possible to deflect small amounts flux in or out of a specific coil thereby increasing or decreasing its effective area. This method is cumbersome and is only really feasible in systems which only have a few measurement channels. However, it does yield a high final balance.

2.3.3 Characterization of gradiometer signals

In this final subsection we look at how different gradiometers respond to specific spatial components of a current distribution. The test current distribution we have chosen is the current dipole [55], an element of current which is infinitesimally small. We scan each type of gradiometer in a plane above the test dipole, and look at the signal in the simulated gradiometer at each point of the plane (see figure 2.5).

The current dipole has always been used in biomagnetism to approximate the size, orientation and magnitude of the primary source(s) in the subject under study. This approach is now under question (see chapter 4), but it is still a widely used source configuration and hence makes an obvious choice for the analysis of gradiometer performance.

The magnetic field B from a current dipole is given by

$$\vec{B}(\vec{r}) = \frac{\mu_o}{4\pi} \frac{\vec{Q} \times \vec{r}}{|\vec{r}|^3} \tag{2.20}$$

where $\vec{Q}$ is the *dipole moment* and is the product of the current element and its magnitude. $\vec{r}$ is the vector from the source to the place where the field is to be calculated.

There are two reasons why the current dipole is a good test source when looking at gradiometer sensitivity. Firstly, it is a useful test of the spatial localisation ability of the

gradiometer. A perfect (if unrealisable) gradiometer would return a delta function response. This would enable two close dipole sources to be resolved. Secondly, any current distribution can be built up from a linear combination of current dipoles, and the response of the gradiometer will similarly be a linear combination of the responses to those dipoles.

In figures A.1 to A.9 (shown in appendix A) the field gradients (up to second order) that can be measured from a current dipole source are shown. Copies of two of these figures are also shown in figures 2.9 and 2.10 at the end of this chapter.

These contour maps are the result of simulating real gradiometers using the algorithms outlined in chapter 3. The gradiometers are made up of circular coils, 1 cm in diameter and the baselines are also 1 cm. As these dimensions are small compared with the distance to the source (5 cm), the gradiometers can be considered to be measuring more or less true spatial gradients of the magnetic fields. On each montage of 3x3 contour plots the dipole is shown

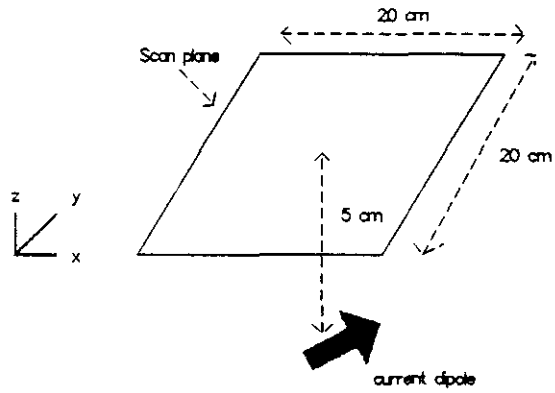

Figure 2.5 Current dipole source and the test scan plane.

as a heavy black arrow at the centre of the plot. A heavy dot indicates that the dipole is pointing out of the page. Dotted contour lines indicate negative values. Each contour plot is normalised independently.

There are several important features to be noted from these plots

- Each gradiometer is sensitive to 2 out of 3 components of the current dipole. For example a $\frac{\partial^2 B_x}{\partial x^2}$ gradiometer has no response to the x component of the current dipole (figure 2.9).

- Some gradiometers give a maximum above the current dipole, while in others the maximum is some distance away.

- In all the gradiometers, the larger the gradient order the better the spatial 'tightness' of the response. In, for example, figure 2.10 the contour lines in the plot of the second order response are bunched much tighter than that of the plot of the response from a field measuring coil. This is obviously desirable as it improves the spatial resolution of the device.

- The plot of $\frac{\partial^2 B_z}{\partial z^2}$ response (2.10) is rotationally stable i.e. as the dipole rotates under the gradiometer, the signal pattern produced remains the same and simply rotates

with the dipole. This quality is desirable for certain inverse problem algorithms such as the expert-system approach (see chapter 5) which relies on pattern recognition. With a rotationally stable pattern it is very easy to get a good first approximation to the dipole orientation.

- Some of the plots are quite complicated and have up to 6 'lobes', while some are simply a single peak. Again, there are advantages and disadvantages to both types. A simple peak is easier to identify and characterize but a more complicated response is easier to pick out from random noise.

The individual normalisation of each contour plot means that in one or two cases a mistaken impression of equal sensitivity to both dipole components might be given. Figure 2.6 shows the second order derivatives of B_x with respect to z for the two dipole components which this gradiometer is sensitive to (i.e. y and z). Instead of a contour map representation, a single scan along the y axis is shown. It is obvious that the stronger sensitivity is to the y component of the dipole. The reason for this is that the maximum response to the z component does not occur above the source but several centimetres away. At this position the gradiometer is further away from the source than if it were directly above, so the signal is reduced.

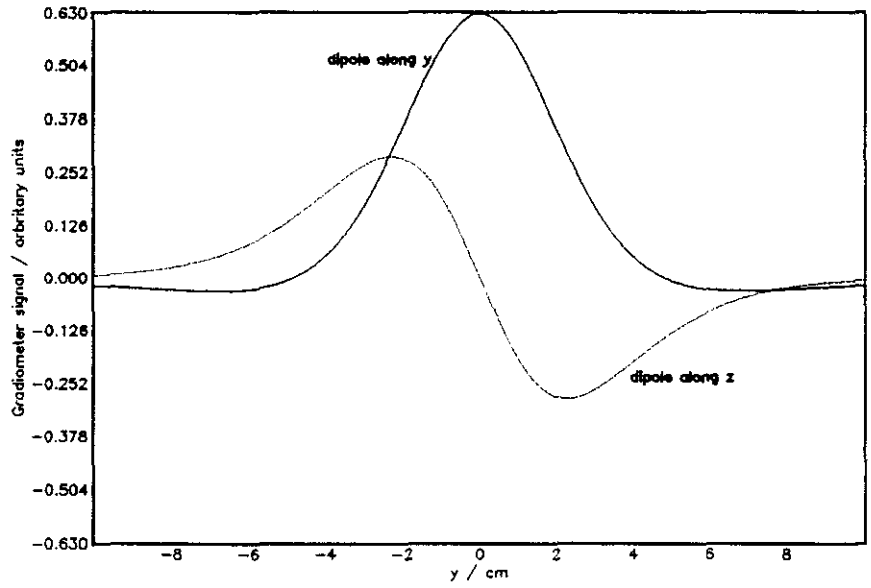

Figure 2.6 A scan along the y axis, using a $\frac{\partial^2 B_x}{\partial z^2}$ gradiometer over a dipole pointing along y, and a dipole pointing along z.

As well as gradiometers that measure 'pure', single components of equation 2.17 it is possible to construct gradiometers that measure mixtures of field gradients. One interesting gradiometer of this type is the concentric-circle gradiometer [47] and is shown in figure 2.7. This gradiometer measures an approximation to $\nabla^2 B_z$ with $\nabla = (\partial_x, \partial_y)$ and its response to the test dipole configuration described earlier is shown in figure 2.8. It is the only planar gradiometer which produces a rotationally stable pattern but has the disadvantage of having

to be fairly large to give a signal comparable to that of a standard axial gradiometer. This means that the spatial resolution is not as good as some other gradiometers. Another problem is that it is very difficult to manufacture accurate circular coils using thin-film techniques.

The planar or 'off diagonal' gradiometers do have a disadvantage in their lack of rotational stability. However they have a major advantage in the fact that it is possible to pack more gradiometers into a small space, because there is no need for large winding formers. It is also clear that manufacturing these devices using thin-film techniques would produce reproducible, well balanced gradiometers. For this reason here at the Open University we decided to investigate further the use of planar gradiometers both in a test thin film project (see chapter 7) and in a 3 channel system which uses wire-wound gradiometers. This system is a good example of the efficiency of planar gradiometers as the 3 channels fit into a dewar space previously occupied by a single non-planar gradiometer.

Having decided on the type of gradiometer we wish to construct it is necessary to come up with the best design consistent with our design constraints. This is the subject of the next chapter.

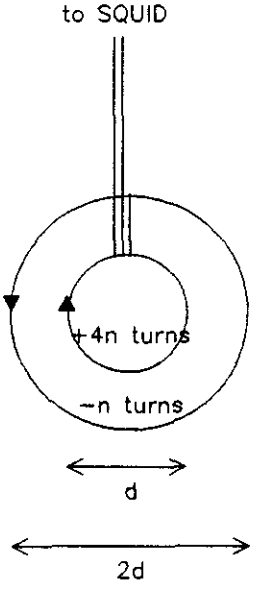

Figure 2.7 A concentric circle gradiometer.

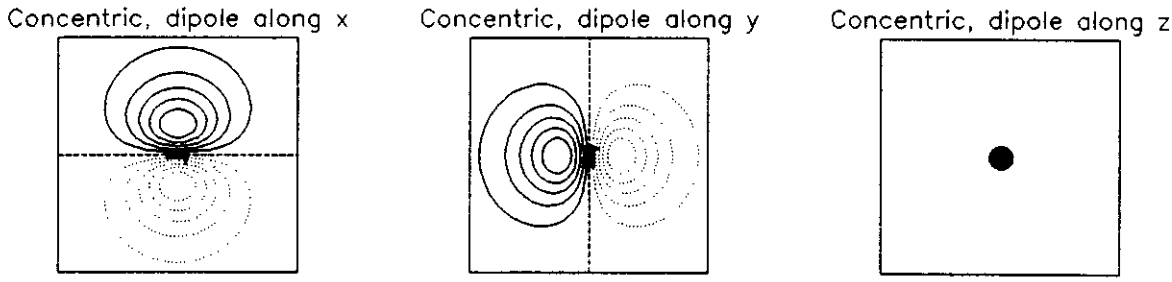

Figure 2.8 Response of a concentric circle gradiometer to a current dipole.

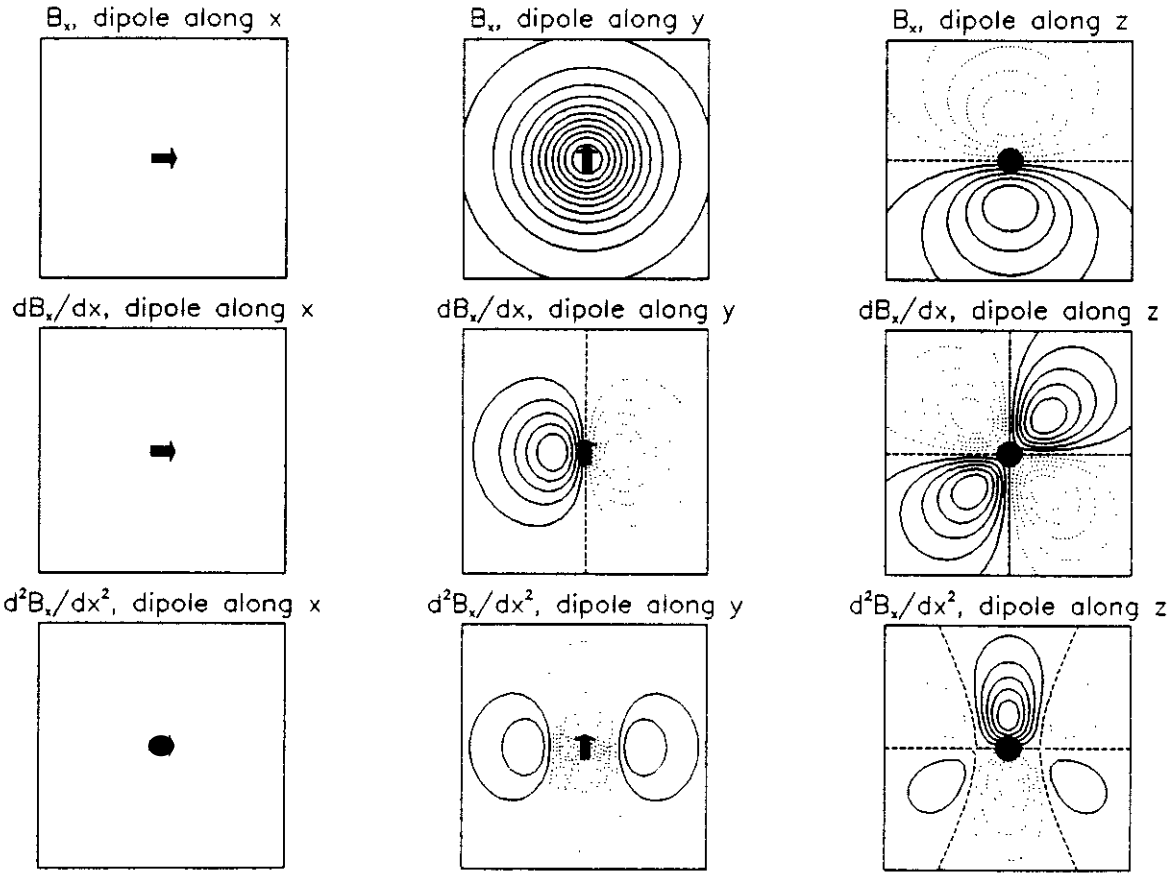

Figure 2.9 B_x and its x derivatives.

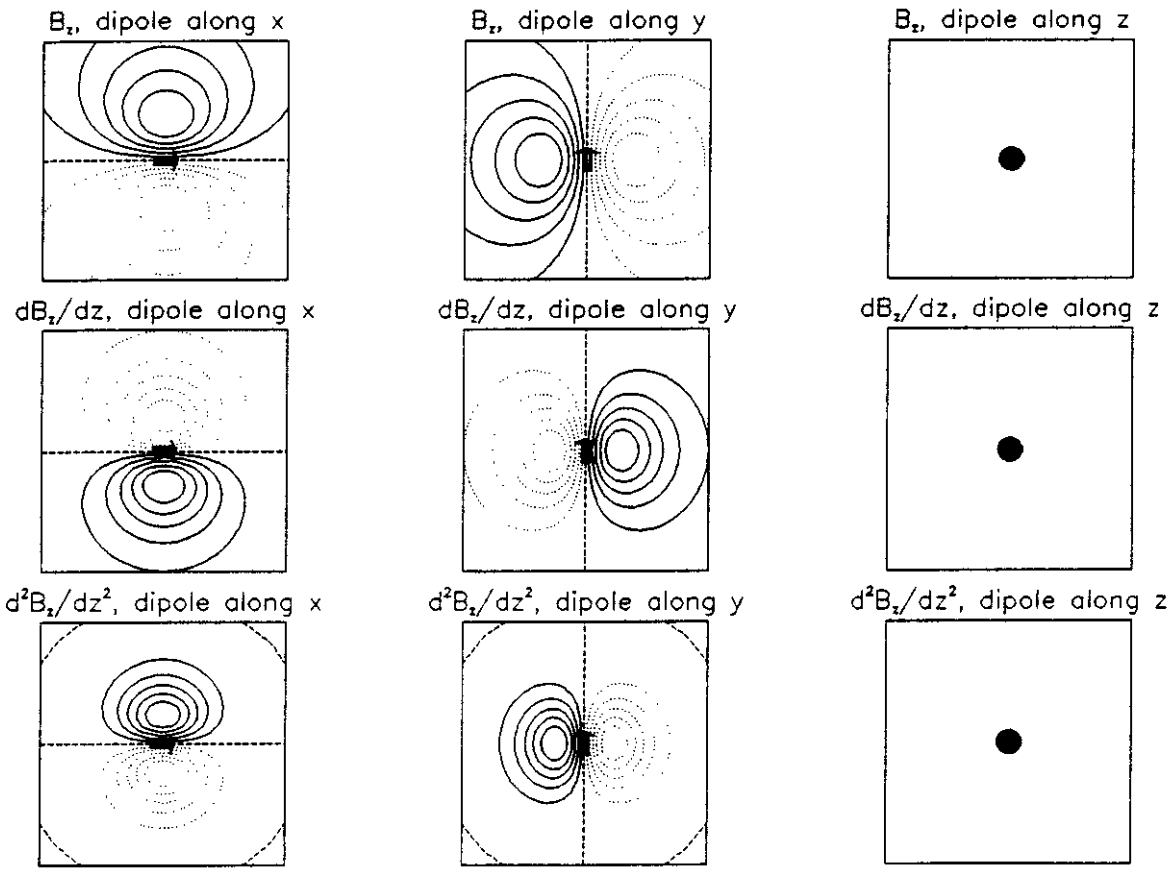

Figure 2.10 B_z and its z derivatives.

Chapter 3

Forward-problem optimisation of gradiometers

In this chapter we consider one aspect of the optimal design of a gradiometer, the maximisation of the signal from the gradiometer in response to a trial source configuration. To do this we must solve what is known as the *forward problem* i.e. the calculation of the magnetic field generated by a current distribution.

In the first section of this chapter, we define some of the parameters that need to be calculated if we are to simulate a particular gradiometer, together with the algorithms used to calculate them. These include the flux in the gradiometer arising from various sources, and the total device inductance. We also look at the calculation of the theoretical balance of an arbitrary planar gradiometer path.

In the second section we introduce some parameters which can be used to characterize a gradiometer's forward problem performance. These parameters give an indication of how large a signal the gradiometer will give from a particular source, how good the gradiometer is at rejecting noise sources and what the spatial resolution of the device will be.

For most gradiometers, optimisation will involve the user in a manual 'trial and error' procedure which will consist of defining a few similar gradiometers, calculating the forward problem parameters and then choosing a design. For axial gradiometers it is relatively easy to design an optimised gradiometer (consistent with the physical design constraints such as dewar-tail size) in this way as there are a limited number of valid (i.e balanced) gradiometers. The only complication occurs when specialised assymetric devices are constructed, such as SQUIDLET which has a very small bottom coil to improve spatial resolution.

For planar geometries, the problem is more complicated as there are more 'degrees of freedom' in the design. Although confined to a plane, the superconducting pathway making up the gradiometer can be distributed in an arbitrary way in that plane, so long as the device is balanced. For axial geometries this balance criterion is such that it reduces the number of valid gradiometers to a few choices which are easily recognised by the user. For planar geometries these choices are not as apparent and so we have investigated the use of a more automated process for this type of device.

These semi-automatic procedures are only really suited to specific types of planar gradiometer together with particular current source configurations. This is because the procedures are essentially 'brute-force' numerical algorithms which rely on fast calculation of

the flux in the device. A numerical algorithm was chosen as this is the easiest way to take account of physical design constraints such as the size of the dewar tail.

In the final section of this chapter we describe the use of these optimisation procedures and present examples of their use. The gradiometers used in the three channel system currently under construction in our laboratory, and the thin-film gradiometer described in chapter 7 were designed in this way. We also show how the SQUID parameters can be included in the optimisation to make maximum use of extremely sensitive dc-SQUID devices which have just become available.

3.1 Calculation of gradiometer parameters

The forward problem optimisation of a gradiometer relies on us being able to simulate the gradiometer in a computer model. To do this we must be able to calculate all the relevant parameters in the flux transformer equation 2.12, i.e.

- the flux in each coil.
- the inductance of each coil.

In addition, we must be able to calculate the balance of a simulated gradiometer, to ensure it is only sensitive to the required field components.

It is worth noting here that we have chosen to neglect the mutual inductance between individual coils in the gradiometer design. For most axial geometries, with the coils a significant distance apart, this is a valid approximation. For planar devices with the superconducting paths defined in a much more arbitrary way the acceptability of the approximation is not so apparent. However, the inductance calculation procedures for an arbitrary current path (described below), will automatically take care of this effect as they do not involve breaking the gradiometer down into a subset of coils but treat the whole device as a single pathway.

3.1.1 Flux calculations

The first step in simulating a gradiometer is to calculate the flux through each of the gradiometer coils. Several algorithms are used, depending on the shape of the coils and the type and orientation of the current source. The three current sources used are :-

- a current dipole in free space.
- a current dipole in a conducting sphere.
- a magnetic dipole in free space.

In most cases it is sufficient to use the first of these sources as it is a good comparative test of ability to detect weak, localised sources. If a more absolute characterization of source detection within the brain is needed then using a current dipole in a conducting sphere is a

useful first step. The magnetic dipole is often used as model of a distant noise source so as to look at the gradiometer's ability to reject noise.

The choice of algorithm for flux calculations is also affected by the coil geometry. The types of coil used are :-

- circular coils.
- rectangular coils.
- triangular coils.
- arbitrary current path coils (spirals etc).

Wire-wound, axial gradiometers are usually made from circular coils, planar gradiometers are usually rectangular as curved pathways are more difficult to fabricate and balance.

Thin-film planar gradiometers actually consist of flat spirals rather than true rectangles and can be treated as a single current pathway, rather than a set of discrete coils. However the pitch of the spiral is usually much smaller than the size of the coil, and so can be treated as a rectangular coil for most simulation purposes.

It is possible to construct a general algorithm which would work for any current source and coil geometry by simply evaluating the following integral numerically

$$\Phi_{coil} = \int_S \vec{\mathbf{B}}.\mathbf{d}\vec{\mathbf{A}} \tag{3.1}$$

However, this is not efficient and can be time consuming. For some of the source-geometry configurations there are either faster numerical solutions or analytical expressions. Figure 3.1 shows the decision tree used by a semi-intelligent flux integration algorithm to select the most efficient way of calculating the flux through a particular coil.

Expansion integral for circular coils

If the coils are circular it is possible to use a series expansion of the field around the centre of the coil. This fast and powerful technique was first outlined by Ioannides and Swithenby [24]. The general method can cope with any complicated source distribution, but in this thesis only single sources are considered. If we consider a circular coil of radius α and symmetry axis $\hat{x}_3$, whose centre is separated from a current source by $\vec{\mathbf{r}}_0$, then the flux through this coil is

$$\Phi_{coil} = \pi\alpha^2(\frac{r_d}{r_0})^3(\vec{\mathbf{B}}(\vec{\mathbf{r}_0}).\hat{x}_3)\sum_{M=0}^{5} g_M h^M \tag{3.2}$$

where

$$\begin{aligned} g_M &= \frac{(4M+1)!!}{(M+1)2^{2M}(M!)^2} \\ h &= \frac{\alpha^2(r_0^2 - r_{03}^2)}{r_d^4} \\ r_d^2 &= r_0^2 + \alpha^2 \end{aligned}$$

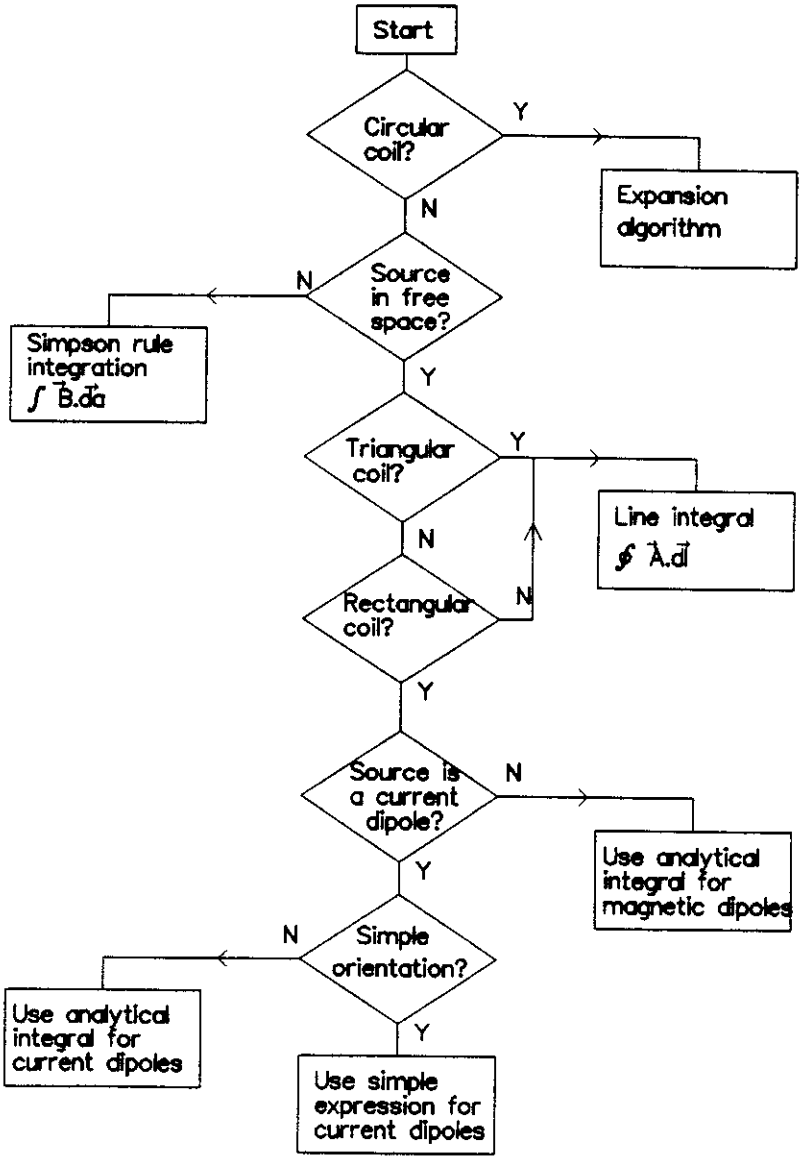

Figure 3.1 Decision flowchart for choosing the flux calculation algorithm.

$\vec{B}(\vec{r_0})$ is the calculated field due to the source, at the centre of the coil. By using 6 expansion terms, the method is accurate to better than 0.2 percent if the source is greater than one coil radius away [24].

Simpson rule integration

If the coils are not circular and the source is not in free space, it is necessary to evaluate the field-area integral directly. This is because there is no analytical expression for the magnetic vector potential $\vec{A}$ from a source in a conducting sphere. This is the most time-consuming of the algorithms as the field from the the source is evaluated at 22x22 positions on each coil. The expression for the flux in the coil is evaluated using Simpson's $\frac{3}{8}$ rule extended into two dimensions [25]

$$\Phi_{coil} = \frac{9}{64} \sum_{j=1}^{22} \sum_{k=1}^{22} b(j)b(k)\vec{B}(\vec{r}_{jk}) \tag{3.3}$$

Where $b(i)$ is the ith Simpson coefficient and $\vec{r}_{jk}$ is the vector joining the source to the jk^{th} gridpoint within the coil.

Analytical expressions

If the source is in free space, analytical expressions for the flux through a rectangular coil can be derived, both for a current dipole source and a magnetic dipole source. This method relies on a line integral of the magnetic vector potential, $\vec{A}$, where $\vec{B} = \nabla \times \vec{A}$. The flux through the coil is then

$$\Phi_{coil} = \oint \vec{A}.\vec{dl} \tag{3.4}$$

The magnetic vector potential for a current dipole is

$$\vec{A} = \frac{\mu_0 Q[dl_x, dl_y, dl_z]}{4\pi \mid \vec{r} \mid} \tag{3.5}$$

Where $\vec{Q}$ is the dipole moment, and can be written as $Q\vec{dl}$ where $\vec{dl} = [dl_x, dl_y, dl_z]$. The integral for the flux through the rectangular coil is then

$$\begin{aligned} \Phi_{coil} &= \int_{Y_1}^{Y_2} A_y(r_z = Z_1)dr_y + \int_{Z_1}^{Z_2} A_z(r_y = Y_2)dr_z \\ &+ \int_{Y_2}^{Y_1} A_y(r_z = Z_2)dr_y + \int_{Z_2}^{Z_1} A_z(r_y = Y_1)dr_z \end{aligned} \tag{3.6}$$

Where the Ys and Zs are the coordinates of the vertices of the rectangular coil (see figure 3.2). Substituting in equation 3.6 the expression for $\vec{A}$ from equation 3.5 gives

$$\begin{aligned} \Phi_{coil} &= \frac{\mu_0 Q}{4\pi} \left\{ \int_{Y_1}^{Y_2} \frac{dl_y}{\sqrt{X^2 + Z_1^2 + r_y^2}} dr_y + \int_{Z_1}^{Z_2} \frac{dl_z}{\sqrt{X^2 + Y_2^2 + r_z^2}} dr_z \right. \\ &+ \left. \int_{Y_2}^{Y_1} \frac{dl_y}{\sqrt{X^2 + Z_2^2 + r_y^2}} dr_y + \int_{Z_2}^{Z_1} \frac{dl_z}{\sqrt{X^2 + Y_1^2 + r_z^2}} dr_z \right\} \end{aligned} \tag{3.7}$$

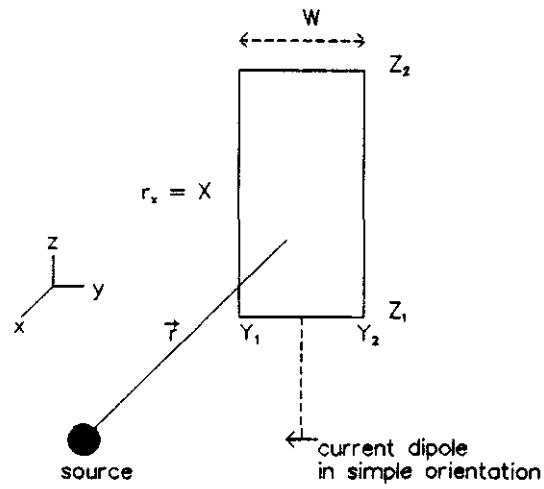

Figure 3.2 Rectangular coil coordinate system.

These integrals are analytically soluble. Each of the above integrals gives rise to two inverse hyperbolic sine terms or $sinh^{-1}$. If we define a new function H_{rct} such that

$$\begin{aligned} H_{rct}(a,b,c,d,e) &= sinh^{-1}\left(\frac{b}{\sqrt{e^2+c^2}}\right) - sinh^{-1}\left(\frac{a}{\sqrt{e^2+c^2}}\right) \\ &+ sinh^{-1}\left(\frac{a}{\sqrt{e^2+d^2}}\right) - sinh^{-1}\left(\frac{b}{\sqrt{e^2+d^2}}\right) \end{aligned} \tag{3.8}$$

Then the expression for the flux in a rectangular coil, generated by a current dipole is

$$\Phi_{coil} = \frac{\mu_0 Q}{4\pi}\left\{dl_y H_{rct}(Y_1,Y_2,Z_1,Z_2,X) - dl_z H_{rct}(Z_1,Z_2,Y_1,Y_2,X)\right\} \tag{3.9}$$

Note that the x component of the dipole does not contribute any flux to the coil. A similar expression can be derived for a magnetic dipole in free space. The magnetic vector potential for a magnetic dipole is

$$\vec{\mathbf{A}} = \frac{\mu_0}{4\pi r^3}\vec{\mathbf{Q}} \times \vec{\mathbf{r}} \tag{3.10}$$

or in terms of components

$$\begin{aligned} A_x &= \frac{\mu_0 Q}{4\pi r^3}(dl_y r_z + dl_z r_y) \\ A_y &= \frac{\mu_0 Q}{4\pi r^3}(dl_z r_x + dl_x r_z) \\ A_z &= \frac{\mu_0 Q}{4\pi r^3}(dl_x r_y + dl_z r_x) \end{aligned} \tag{3.11}$$

These components can be substituted into equation 3.6 to give

$$\begin{aligned} \Phi_{coil} &= \frac{\mu_0 Q}{4\pi}\left\{\int_{Y_1}^{Y_2}\frac{dl_z X - dl_x Z_1}{(X^2+Z_1^2+r_y^2)^{\frac{3}{2}}}dr_y + \int_{Z_1}^{Z_2}\frac{dl_x Y_2 - dl_y X}{(X^2+Y_2^2+r_z^2)^{\frac{3}{2}}}dr_z\right. \\ &+ \left.\int_{Y_2}^{Y_1}\frac{dl_z X - dl_x Z_2}{(X^2+Z_2^2+r_y^2)^{\frac{3}{2}}}dr_y + \int_{Z_2}^{Z_1}\frac{dl_x Y_1 - dl_y X}{(X^2+Y_1^2+r_z^2)^{\frac{3}{2}}}dr_z\right\} \end{aligned} \tag{3.12}$$

Again these integrals are analytically soluble, but this time yield a simple geometric function rather than a trigonometric one. If we define a new function R_{rct} such that

$$R_{rct}(a,b,c,d) = \frac{c}{(a^2+b^2)\sqrt{a^2+b^2+c^2}} - \frac{d}{(a^2+b^2)\sqrt{a^2+b^2+d^2}} \tag{3.13}$$

Then the flux in the coil, due to a magnetic dipole can be written as

$$\begin{aligned}\Phi_{coil} &= \frac{\mu_0 Q}{4\pi}\{(dl_z X - dl_x Z_1)R_{rct}(X, Z_1, Y_2, Y_1) \\ &+ (dl_z X - dl_x Z_2)R_{rct}(X, Z_2, Y_1, Y_2) \\ &+ (dl_x Y_2 - dl_y X)R_{rct}(X, Y_2, Z_2, Z_1) \\ &+ (dl_x Y_1 - dl_y X)R_{rct}(X, Y_1, Z_1, Z_2)\}\end{aligned} \tag{3.14}$$

In the optimisation procedures described later in section 3.2, a current dipole is used in a simple configuration. The dipole is defined to be pointing along the y axis and is symmetrically placed beneath the bottom edge of the rectangular coil i.e. $Y_1 = -Y_2 = \frac{W}{2}$ and $X = 0$. In this situation the flux in the coil reduces to a simple expression which can be evaluated quickly, namely

$$\Phi_{coil} = \frac{\mu_0 Q}{2\pi}\left\{sinh^{-1}(\frac{W}{2Z_1}) - sinh^{-1}(\frac{W}{2Z_2})\right\} \tag{3.15}$$

The expressions presented in this chapter allow us to calculate the flux trapped in most gradiometer geometries, in response to the current sources that we are especially interested in. We must also insure that the gradiometers we design are balanced, and this is the subject of the next subsection of this thesis.

3.1.2 Balance calculations

In this part of this thesis, we investigate some of the issues that are important in balancing a gradiometer. We shall investigate only the theoretical considerations, and it is worth noting that even if a gradiometer is *designed* with a high balance, after construction the balance may be much worse than the theoretical prediction. This imbalance can occur because of lack of accuracy in fabrication, or because of the effect of mutual inductance with other coils/gradiometers.

A gradiometer which has been designed as an n^{th} order gradiometer should have no sensitivity to field-gradients of order less than n. For simple coil shapes such as rectangles and circles, the balance in a new, simulated gradiometer can be calculated by simply analysing the area of each coil. The $n = 0$ or field balance criterion can be expressed as follows

$$\sum_{k=1}^{coils} N_k A_k = 0 \tag{3.16}$$

Where A_k is the area of the A^{th} coil , and N_k carries the additional information of a plus or minus sign depending in which sense the k^{th} coil is wound.

A similar expression can be written for the $n = 1$ or first order gradient balance. If we define an axis, $\vec{d}$, to be the axis along which the gradiometer differentiates and d_k (which can be positive or negative) to be the displacement between the centre of the k_{th} coil and the geometric centre of the gradiometer, along the $\vec{d}$ axis, then this first order gradient balancing criteria can be written as:

$$\sum_{k=1}^{coils} N_k A_k d_k = 0 \tag{3.17}$$

The geometric centre is here taken to mean the centre of a line bounded by the ends of the flux gathering areas of the gradiometer and directed along the $\vec{d}$ axis. The above formula is valid only if the coils are symmetrical about this line.

For gradiometers such as the planar ones fabricated using thin film techniques, this type of balance analysis is not valid as the coils are flat spirals. For these types of gradiometer it is best to treat the whole gradiometer as a single flux gathering path rather than a set of discrete, serially connected coils.

Consider a planar gradiometer which consists of line segments distributed in the xy plane. This gradiometer will be sensitive to some function of the z component of the magnetic field. Suppose a field $\vec{\mathbf{B}} = (0, 0, B_z)$ where $B_z = \frac{1}{n!}y^n$ is applied to this gradiometer. We choose this form for the field because it fulfills the condition $\frac{\partial^n B_z}{\partial y^n} = 1$. If the gradiometer is to be balanced to the n^{th} order field then the total flux through the gradiometer from this applied field should be zero.

$$0 = \int_S \vec{\mathbf{B}}.\mathrm{d}\vec{\mathbf{A}} \tag{3.18}$$

Using Stokes' theorem we can replace the area integral with a line integral around the gradiometer path.

$$0 = \oint \vec{\mathbf{A}}.\mathrm{d}\vec{\mathbf{l}} \tag{3.19}$$

where $\vec{\mathbf{B}} = \nabla \times \vec{\mathbf{A}}$. We need to choose a form for $\vec{\mathbf{A}}$ which is consistent with the applied field. The cross product relationship between $\vec{\mathbf{A}}$ and $\vec{\mathbf{B}}$ can be expressed as a matrix determinant

$$\vec{\mathbf{B}} = (0, 0, B_z) = \begin{vmatrix} \frac{\partial}{\partial x} & \frac{\partial}{\partial y} & \frac{\partial}{\partial z} \\ A_x & A_y & A_z \end{vmatrix} \tag{3.20}$$

Or in terms of components

$$\begin{aligned} 0 &= \frac{\partial A_z}{\partial y} - \frac{\partial A_y}{\partial z} \\ 0 &= \frac{\partial A_x}{\partial z} - \frac{\partial A_z}{\partial x} \\ \frac{1}{n!}y^n &= \frac{\partial A_y}{\partial x} - \frac{\partial A_x}{\partial y} \end{aligned} \tag{3.21}$$

We can choose any $\vec{\mathbf{A}}$ which satisfies the above equations. For example,

$$\begin{aligned} A_x &= 0 \\ A_y &= \frac{1}{n!}xy^n \\ A_z &= 0 \end{aligned} \tag{3.22}$$

or

$$\begin{aligned} A_x &= -\frac{1}{n!(n+1)} y^{n+1} \\ A_y &= 0 \\ A_z &= 0 \end{aligned} \tag{3.23}$$

substituting the vector $\vec{\mathbf{A}}$ defined by equation 3.22 into equation 3.19 gives

$$0 = -\frac{1}{n!} \oint x y^n dy \tag{3.24}$$

or

$$0 = -\frac{1}{n!(n+1)} \oint y^{n+1} dx \tag{3.25}$$

Either of these (equivalent) conditions must be satisfied if a gradiometer is to be insensitive to the n^{th} y derivative of the field. The corresponding conditions for the x derivatives can be derived in exactly the same way

$$0 = -\frac{1}{n!} \oint y x^n dx \tag{3.26}$$

or

$$0 = \frac{1}{n!(n+1)} \oint x^{n+1} dy \tag{3.27}$$

These line integrals are evaluated numerically by dividing the gradiometer pathway into a set of small line elements. Equation 3.24 then becomes

$$0 = -\frac{1}{n!} \sum_{i=1}^{elements} x_i y_i^n \Delta y_i \tag{3.28}$$

In practice it is very difficult to design a complicated planar gradiometer which will give zero as the result of the above integrals. The actual result will be a measure of the imbalance to a particular field-gradient and the designer must seek to minimise this. At present, there is no automatic procedure to do this and the gradiometers designed so far have been the result of a 'juggling' of the dimensions to gain the best balance.

3.1.3 Inductance calculations

In this subsection we list the formulas used in calculating the inductance of a gradiometer. For simple coil shapes such as rectangles and circles there are simple analytical expressions for the inductance (see [11], p60 and p143)

$$L_{circle} = \mu_0 r \left[ln(\frac{8r}{\rho}) - 1.75 \right] \tag{3.29}$$

$$\begin{aligned} L_{rectangle} &= \frac{\mu_0}{\pi} \left[a ln(\frac{2a}{\rho}) + b ln(\frac{2b}{\rho}) \right. \\ &- a sinh^{-1}(\frac{a}{b}) - b sinh^{-1}(\frac{b}{a}) \\ &+ \left. 2\sqrt{a^2+b^2} - \frac{7}{4}(a+b) \right] \end{aligned} \tag{3.30}$$

Where r is the radius of the circular coil, b and a are the sides of the rectangular coil and ρ is the wire radius. Note that all the inductance formulae assume a wire of circular cross-section. However these formulae will be accurate to a few percent for wires (or thin films) of different cross-section ([11], p35).

If the coils have N turns then the inductance is increased by a factor $N^{(2-t)}$, where t is the 'tightness' of the coil. All the coils considered in this thesis are tightly wound and in this condition $t = 0$. If the coil turns were infinitely spaced, then t would equal 1. These simple formulae are perfectly adequate for most cases, but in the case of the spirals and other shapes used in thin-film gradiometers, it was not clear whether using a rectangle to simulate the coil shape was a valid approximation in the inductance calculation. As the balance calculations for these devices already involved breaking the gradiometer pathway down into line elements, it is possible to extend this approach to calculate the total device inductance. We consider the gradiometer to be constructed of line elements which lie *either* along x or y i.e the elements are parallel or anti-parallel. This is a valid restriction as thin-film processes often restrict the device geometry to be in this form. The inductance of the device is then the sum of the mutual inductances between each pair of (parallel) elements

$$L = \sum_{i=1}^{N} \sum_{j=1}^{N} M_{ij} \tag{3.31}$$

This expression includes the inductance a line element has with itself i.e the self inductance of that element

$$L = \sum_{k=1}^{N} L_k + \sum_{i=1}^{N} \sum_{j=1, i \neq j}^{N} M_{ij} \tag{3.32}$$

The self inductance of an element of length l, radius ρ is [11]

$$L = \frac{\mu_0}{2\pi} l \left[ln\left(\frac{2l}{\rho}\right) - 0.75 \right] \tag{3.33}$$

The mutual inductance of two elements l_1 and l_2 lying along the y direction, and separated by $\vec{r_0} = (r_{0x}, r_{0y}, 0)$ is

$$\begin{aligned} M &= \frac{\mu_0 r_{0x}}{4\pi} \left\{ f\left(\frac{r_{0y} + \frac{l_1}{2} + \frac{l_2}{2}}{r_{0x}}\right) - f\left(\frac{r_{0y} + \frac{l_1}{2} - \frac{l_2}{2}}{r_{0x}}\right) \right. \\ &+ \left. f\left(\frac{r_{0y} - \frac{l_1}{2} - \frac{l_2}{2}}{r_{0x}}\right) - f\left(\frac{r_{0y} - \frac{l_1}{2} + \frac{l_2}{2}}{r_{0x}}\right) \right\} \end{aligned} \tag{3.34}$$

Where

$$f(u) = u sinh^{-1}(u) - \sqrt{1 + u^2} \tag{3.35}$$

3.2 Optimisation

In this section we look at the forward problem optimisation of a gradiometer.

The problem is essentially to choose a gradiometer from the many valid ones that might be consistent with the designer's physical design constraints. For example the new three

channel probe we wish to build for our laboratory must fit into a cylindrical dewar tail of diameter 29mm and length 80 mm. This immediately suggests to us that we should use planar devices (which are less bulky than axial gradiometers), with the long axis of the gradiometer lying along the length of the dewar tail.

Having decided on the specific type of gradiometer, we must then decide which parameters we will use to characterize the gradiometer to allow us to choose from the many valid gradiometers of that form. The various parameters we can use are described in the first part of this section. They are mostly concerned with maximising the signal that is output from the coupled SQUID, given a particular signal source applied to the coils of the gradiometer. In addition there is a parameter which quantifies the ability of the gradiometer to separate two close localised sources.

The optimal design of gradiometers must be either a 'trial and error' operation or a numerical procedure; there is no simple function which can be maximised to give the 'best' gradiometer. There are two reasons for this. Firstly there are at least two desirable design features (namely spatial resolution and signal sensitivity) which are incompatible in any optimisation procedure e.g. a large coil gives poor spatial resolution but is able to gather more flux. Secondly, it is necessary to include boundary conditions such as the maximum dimensions of the device in the optimisation process.

We have found that for simple axial gradiometers, the designer is able to pick out a valid, balanced design which is likely to give a reasonable response to a particular source. For planar gradiometers with their more complicated shapes, this is more difficult and a numerical procedure has been found to be very useful in picking out the 'best' gradiometer.

3.2.1 Characterization parameters

The parameters that we have used to characterize the forward problem performance of a particular gradiometer are as follows.

- Gradient sensitivity
- Dipole sensitivity
- 'Signal to noise'
- 'Spread'

Gradient sensitivity

This has been one of the standard parameters for characterizing the performance of a gradiometer. It is the field gradient which gives a flux in the SQUID loop equal to the SQUID's intrinsic flux noise. Consider a standard second order axial gradiometer which produces a signal of the form $\frac{\partial^2 B_z}{\partial z^2}$. Equation 2.12 can then be written

$$\Phi_{SQUID} = \frac{M}{L_{total}}(N_1\Phi_1 + N_2\Phi_2 + N_3\Phi_3) \tag{3.36}$$

Where L_{total} is the total self inductance of the gradiometer, plus the input coil inductance. For this gradiometer to balance then $N_2 = -(N_1 + N_3) = 2N$. Suppose that we apply a field which has an n^{th} order gradient in the z direction i.e. $\frac{\partial^n B_z}{\partial z^n} = K_g$. Then the form of the field is $B_z = K_g \frac{z^n}{n!}$ where K_g is a constant. If the x and y variation of the field is the same in all three coils, the flux in each coil is a simple product of the area of each coil with the field at the centre

$$\Phi_{SQUID} = \frac{MAN}{L_{total}} \left(B_z(z_1) - 2B_z(z_2) + B_z(z_3) \right) \tag{3.37}$$

We can write the z coordinates of the centre of each coil as follows: $z_1 = 0, z_2 = d_1, z_3 = d_1 + d_2$, where d_1 and d_2 are the baselines of the gradiometer. For a standard symmetric gradiometer, $d_1 = d_2 = d$ and so

$$\Phi_{SQUID} = \frac{K_g MAN}{L_{total}} \frac{\left(-2d^n + (2d)^n\right)}{n!} \tag{3.38}$$

Note that if $n = 1$ in the above equation, Φ_{SQUID} equals zero, which is what we would expect from a second order gradiometer. If we set Φ_{SQUID} equal to the intrinsic flux noise Φ_{noise} then K_g becomes the sensitivity to gradients of order n. For a second order gradiometer we are interested in the $n = 2$ sensitivity, so rearranging for K_g gives

$$K_g = \frac{\Phi_{noise} L_{total}}{MAN} \frac{1}{d^2} \tag{3.39}$$

For the SHE axial gradiometer used in our laboratory,

$$\begin{aligned} M &= 0.019\mu\text{H} \\ L_{total} &= 4\mu\text{H} \\ N &= 2 \\ d &= 0.032\text{m} \\ \Phi_{noise} &= 3.8 \times 10^{-19}\text{Webers} \\ A &= \pi(0.012)^2\text{m}^2 \end{aligned}$$

Which gives $K_g = 8.6 \times 10^{-11}\text{Tm}^{-2}$

For planar gradiometers, the analysis is more complicated as the field is varying over each coil. Consider the second order planar gradiometer shown in figure 3.3. Equation 2.12 in this case becomes

$$\Phi_{SQUID} = \frac{MW}{L_{total}} \left(N_1 \int_{x_1}^{x_2} B_z + N_2 \int_{x_3}^{x_4} B_z + N_3 \int_{x_5}^{x_6} B_z \right) \tag{3.40}$$

Again we can apply a field of the form $B_z = K_g \frac{x^n}{n!}$

$$\begin{aligned} \Phi_{SQUID} &= \frac{MWK_g}{L_{total}(n+1)!} \left[N_1 \left(x_2^{n+1} - x_1^{n+1} \right) \right. \\ &+ \left. N_2 \left(x_4^{n+1} - x_3^{n+1} \right) + N_3 \left(x_6^{n+1} - x_5^{n+1} \right) \right] \end{aligned} \tag{3.41}$$

We are interested in the $n = 2$ sensitivity and so rearranging for K_g in this case gives

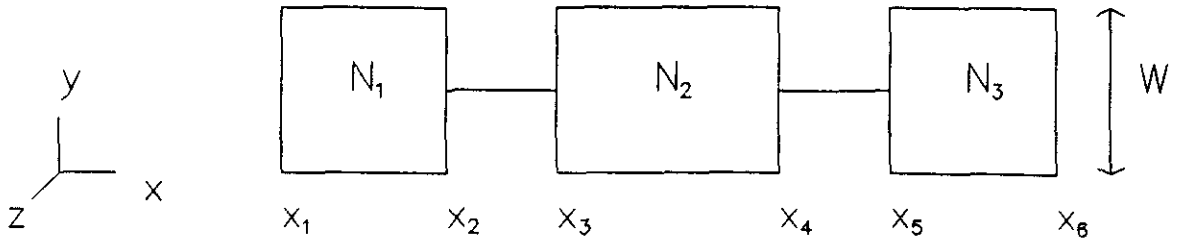

Figure 3.3 Second order planar gradiometer.

$$K_g = \frac{6L_{total}\Phi_{noise}}{MW\left[N_1\left(x_2^3 - x_1^3\right) + N_2\left(x_4^3 - x_3^3\right) + N_3\left(x_6^3 - x_5^3\right)\right]} \tag{3.42}$$

For the gradiometer used in our 3 channel system,

$$\begin{aligned}
M &= 0.019\mu\text{H} \\
L_{total} &= 4.25\mu\text{H} \\
N_1 &= 4 \\
N_2 &= -2 \\
N_3 &= 2 \\
W &= 0.022\text{m} \\
x_1 &= 0.0\text{m} \\
x_2 &= 0.01\text{m} \\
x_3 &= 0.0175\text{m} \\
x_4 &= 0.0575\text{m} \\
x_5 &= 0.060\text{m} \\
x_6 &= 0.080\text{m} \\
\Phi_{noise} &= 3.8 \times 10^{-19}\text{Webers}
\end{aligned}$$

Which gives $K_g = 1.02 \times 10^{-10}\text{Tm}^{-2}$.

The main advantage of using gradient sensitivity to characterize gradiometer performance is that it is an easy analytical expression to calculate and, in the automatic optimisation procedures described later, that is essential. However it does have the disadvantage that it is not always clear whether a small gradient sensitivity is a desirable property. A device which is sensitive to small field gradients will give a large signal from a nearby source, but it will also be sensitive to distant noise sources. In this sense the gradient sensitivity is a rather ambiguous parameter. A more meaningful approach is to look at which sources we want to detect and which sources we want to reject.

Dipole sensitivity

For any gradiometer a vector field $\vec{D}$ may be used to describe the sensitivity of that gradiometer to current dipole sources. For example, $\vec{D}.\hat{e}$ is the sensitivity to a dipole at $\vec{r}$ pointing along the $\hat{e}$ direction and is the dipole moment that this source must possess to give a signal in the SQUID loop equal to the SQUID intrinsic noise. $\vec{D}$ is a vector function which is defined at all points in space but, for practical purposes, we choose to look at a particular component, usually $\hat{e} = \hat{y}$, at one defined point. For example, if we consider the simulated experiment shown in figure 3.4 we can imagine scanning any gradiometer in the plane shown. Somewhere in that plane the gradiometer will give a maximum signal due to the dipole. For some gradiometer configurations that maximum will be directly above the source, in others the maxima will be distributed elsewhere in that plane. Wherever the maxima is, it can be related to the dipole sensitivity, D using the flux transformer equation, 2.12. Here Φ_{max} is the maximum signal expressed as flux in the SQUID loop.

$$\Phi_{max} = \frac{M}{L_{total}} Q \sum N_i \Phi_i(\vec{r_i}) \tag{3.43}$$

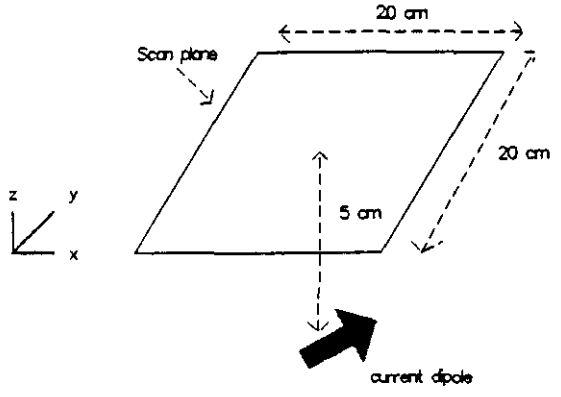

Figure 3.4 Current dipole source and the test scan plane.

The symbols M and L_{total} have the same meaning as before. N_i is the number of turns on the ith coil, and $\Phi_i(\vec{r_i})$ is the flux in the ith coil due to a current dipole in the required orientation. The current dipole has a dipole moment of magnitude Q and is a displacement $\vec{r_i}$ away from the ith coil. Note that these position vectors relate the dipole position to the position where the gradiometer gives a maximum signal. If we make Φ_{max} equal to the intrinsic flux noise in the SQUID, then Q is equal to the dipole sensitivity D. Rearranging gives

$$D = \Phi_{noise} \frac{L_{total}}{M \sum N_i \Phi_i(\vec{r_i})} \tag{3.44}$$

All the terms in the above equation can be calculated in simulation and for certain dipole configurations the flux can be calculated rather quickly using analytical expressions. Again, this is desirable for the numerical optimisation procedures described later.

The main advantage of this parameter is that it is possible to get some feel for the types of physiological source that the gradiometer can detect. For example, a typical dipole

moment for a population of neurons might be around 10^{-8} Am [62] and so if a gradiometer is to detect cortical signals from a depth of around 3-5 cm below the bottom coil, the dipole sensitivity at this depth should be smaller than this figure. These kind of estimates have to be treated very carefully however, because the extrinsic noise (for example in an unshielded room) might be much more important than the SQUID intrinsic noise. A safer approach is to treat dipole sensitivity as a parameter for testing the comparative sensitivities of different gradiometers.

'Signal to noise'

If we simply wanted to maximise the dipole sensitivity, then the simplest approach would be to have a large single coil rather than a gradiometer. This is a rather extreme example of the trade-off between detecting a signal from a particular source, and rejecting environmental noise. One useful parameter we have therefore investigated is the ratio between the signal from a nearby signal source, and the signal from a far noise source. Again using the flux transformer equation, 2.12,

$$S/N = \frac{\Phi_{SQUID}(signal)}{\Phi_{SQUID}(noise)} = \frac{\sum N_i \phi_i(signal)}{\sum N_i \phi_i(noise)} \tag{3.45}$$

In most of the optimisations performed so far the signal source has been a dipole 5 cm below the gradiometer, and the noise source another dipole 2m away.

'Spread'

As well as giving a reasonably large signal, one useful ability we would like to have in our gradiometers is high spatial resolution. As described in chapter 2, gradiometers can give spatially very complicated patterns, and this can limit the ability to resolve two close sources. To quantify this the concept of 'spread' was used. If we refer back to the scan plane shown in figure 3.4, after identifying the position of the maximum signal within this plane, the simulating program moves radially away from this point until it identifies a boundary circle, outside which the signal is at all points less than $\frac{1}{\sqrt{2}}$ of the maximum. The smaller the radius of this circle (known as the 'spread'), the more spatially localised the response is and the better the gradiometer is at resolving two close sources.

3.2.2 Numerical optimisation

Using fast computing techniques it is possible to do a brute force search through all valid gradiometers. Although not very elegant, it is has the great strength that physical design constraints can be easily included in the search. For example in thin-film circuits, devices are often limited by the size of the silicon substrate that the device is fabricated on. In the case of a new 3 channel magnetometer being designed here at the Open University, the overriding design limitation was the small amount of space available in the dewar tail. A standard dewar which normally houses a single axial gradiometer is to be used for all three channels.

An algorithm was implemented to allow the optimal design of the particular type of gradiometer which was to be used both in the thin-film project and the 3 channel system. These gradiometers are second-order, planar, and measure the tangential components of the field. Figure 3.5 shows the general design of one of these devices. The algorithm consists es-

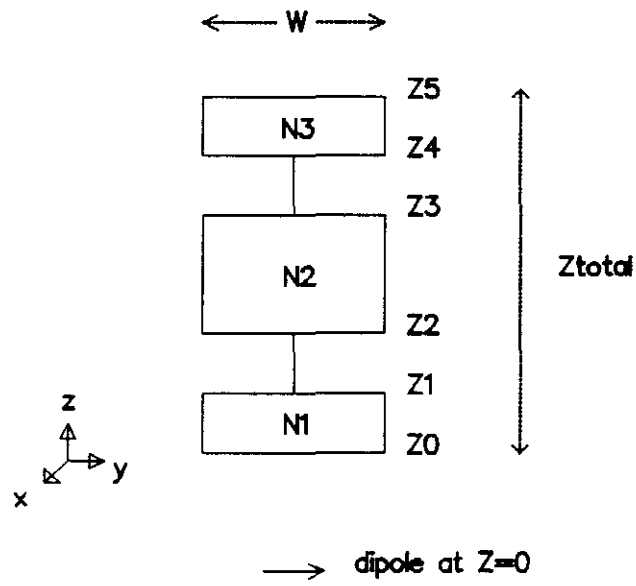

Figure 3.5 General design of the numerically optimised gradiometers.

sentially of a set of nested loops within the program which vary $N_1, N_2, N_3, Z_1, Z_2, Z_3, Z_4, Z_5$ between limits set by the operator. The maximum number of turns allowed on each coil is specified, as is the total device length and the maximum allowable length of each coil. For simplicity, the width of all three coils, W, is assumed to be the same and is specified by the operator. The operator also controls the 'resolution' of the search by specifying a step value.

Note that the dipole orientation and position is fixed to be pointing along y directly below the centre of the bottom edge of the gradiometer. This was picked for two reasons. Firstly, this particular gradiometer gives its maximum signal when the source is in this orientation and position, so there is no need to 'hunt' around in a scan plane to find the maximal point. Secondly, this position and orientation allows the use of a very fast flux calculation formula described in equation 3.15.

The program only evaluates gradiometers which are balanced to uniform fields and uniform first-order gradients. Equation 3.16 shows that a particular design will be balanced to fields if

$$N_1(Z_1 - Z_0) - N_2(Z_3 + Z_2) + N_3(Z_5 - Z_4) = 0 \tag{3.46}$$

The corresponding equation for the gradient balance, derived from equation 3.17 is

$$N_1(Z_1 - Z_0)(Z_2 + Z_3 - Z_1 - Z_0) - N_3(Z_5 - Z_4)(Z_4 + Z_5 - Z_3 - Z_2) = 0 \tag{3.47}$$

After it is established that the gradiometer is valid, the program calculates either the nth order gradient sensitivity or the dipole sensitivity. Before the search the operator can

specify either the gradient to maximise or the depth at which the dipole sensitivity is to be maximised.

If the procedure is to be completed in a reasonable amount of time, the practical limit to the resolution of the search has been found to be around 0.25 cm in the various z values. On our VAX cluster mainframe an optimisation was run with the following parameters

$$N_{max} = 4$$
$$Z_{total} = 8\text{cm}$$
$$Z_{max} = 5\text{cm}$$
$$W = 2.2\text{cm}$$

These were consistent with the design constraints of the three channel system. The program was told to maximise the sensitivity to a current dipole pointing along y at a depth of 5 cm (i.e. $Z_0 = 5$ cm). Below is an extract from the log file which shows the first few valid gradiometers that were found. A total of 2171 valid gradiometers were found using a step size of 0.25 cm. The execution time was around 20 minutes.

```
****************************************************************
Optimisation started  1-OCT-1990 at 18:16:41.33
This is a maximisation of sensitivity to a bare dipole.
Distance to source (cm):5.00
Current noise in input coil: 2.00000E-11
Input coil inductance: 2.00000E-06
Maximum number of turns: 4 4 4
coil width (cm):2.20
Maximum coil length (cm):4.00
Total device length (cm):8.00
Wire radius (microns):25.00
z step (cm):0.25
Coil tightness:0.00 0.00 0.00

****************************************************************
Num  n1 n2 n3  z1   z2   z3   z4   z5  induct      sensitivity
----------------------------------------------------------------
1: 1  1  1 5.50 5.50 6.25 7.00 7.25   1.69520E-07  1.61694E-07
2: 1  1  1 5.50 5.50 6.50 6.50 7.00   1.88602E-07  1.75643E-07
3: 1  1  1 5.50 5.75 6.50 7.75 8.00   1.69520E-07  9.67383E-08
.
.
.
```

The end of the log file shows the optimised gradiometer

```
.
.
.
2169:4 4 4 6.75 7.00 10.50 10.75 12.50 5.46112E-06 1.01695E-08
2170:4 4 4 6.75 7.25 10.75 11.25 13.00 5.46112E-06 9.27049E-09
2171:4 4 4 7.00 7.00 11.00 11.00 13.00 5.92339E-06 9.70520E-09
************************************************************

Optimisation finished  1-OCT-1990 at 18:36:37.82

Most sensitive gradiometer is number 1906.
Which is:-

N1=4
N2=2
N3=2
Z0=5.00
Z1=6.00
Z2=6.75
Z3=10.75
Z4=11.00
Z5=13.00

Inductance is  2.25112E-06 henries.
Dipole sensitivity is  7.84341E-09 Am at a depth of 5.0 cm
Signal to noise parameter is 375049
************************************************************
```

This is the gradiometer used in the new three channel system. Note how the inductance is quite close to the input coil inductance of $2\mu H$. However the log file shows that there are quite a few gradiometers with inductances close to this optimal value, and the algorithm was able to pick this one as the best solution.

For comparison sake, we can show the simulated performance of the standard axial gradiometer (the SHE gradiometer, see figure 2.4) used in our lab. This device has a dipole sensitivity of 1.3×10^{-8}Am, which is a factor of 1.6 worse than the optimised planar gradiometer shown above. This can be accounted for by the fact that an axial gradiometer does not achieve its maximum signal directly above the source. The gradiometer is therefore further way from the source and the maximum signal amplitude is reduced. The signal to noise parameter for SHE is 440465 which is a factor of 1.2 better than the optimised planar gradiometer.

So, this planar gradiometer (which we call OPTBIG2) should be more sensitive to dipolar

sources at depths relevant to cortical structures, than the standard axial gradiometer already in use in our lab. Its ability to reject distant noise sources should be similar. Figure 3.6 shows a single scan over a 3 cm deep dipole for both OPTBIG2 and SHE. The dipole, located at $x = y = 0$, has a dipole moment of 10^{-8}Am and is pointing along the y axis.

As well as showing the difference in maximum signal strength, the graph shows that OPTBIG2 has a spatially 'tighter' pattern for this dipole. The 'spread' parameter for OPTBIG2 is 1.5 cm, while for the SHE gradiometer it is 3.5 cm.

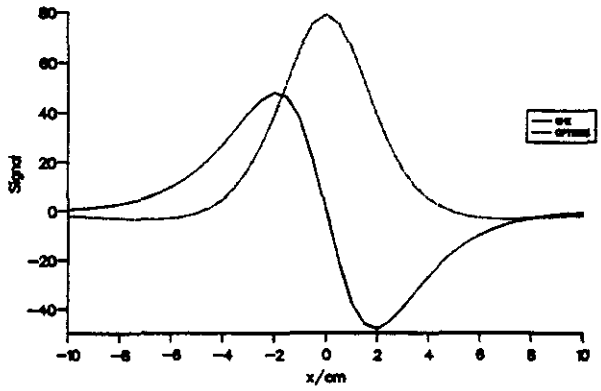

Figure 3.6 Graph of response of SHE and OPTBIG2 gradiometers to a 3 cm deep dipole.

Figure 3.7 shows a graph of the dipole sensitivity for all 2171 valid gradiometers found in the optimisation. The axis represents the gradiometers, sorted into descending order of sensitivity i.e the gradiometers on the far right of the graph have the smallest values of dipole sensitivity, and are therefore the most sensitive gradiometers to this particular source. The y-axis shows the actual value of the dipole sensitivity. The graph shows that there are a few gradiometers which are several hundred times less sensitive than OPTBIG2, but which are valid gradiometers. The graph falls very sharply to a slowly falling plateau in which by far the majority of the gradiometers reside. This would suggest that there are a large number of gradiometers with sensitivities within an order of magnitude of that of OPTBIG2 and hence there is no real need to carry out a proper optimisation analysis. However, the problem is in making sure that we choose a gradiometer that is within this plateau region, and there does not seem to be a hard and fast rule for making this choice. Even if the gradiometer is within this region, our optimisation analysis (in this example at least) provides us with a gradiometer which may be a factor of 5 more sensitive than another plateau gradiometer, and this is obviously desirable.

Another strength of this type of optimisation procedure is that it allows the SQUID parameters to be varied. The newest DC SQUIDs to be developed [51] have intrinsic noise values 100 times smaller than the RF SQUIDS we are using. An optimisation was run using these SQUIDS and the result is shown below

```
************************************************************
Optimisation started  2-OCT-1990 at 12:08:14.97
```

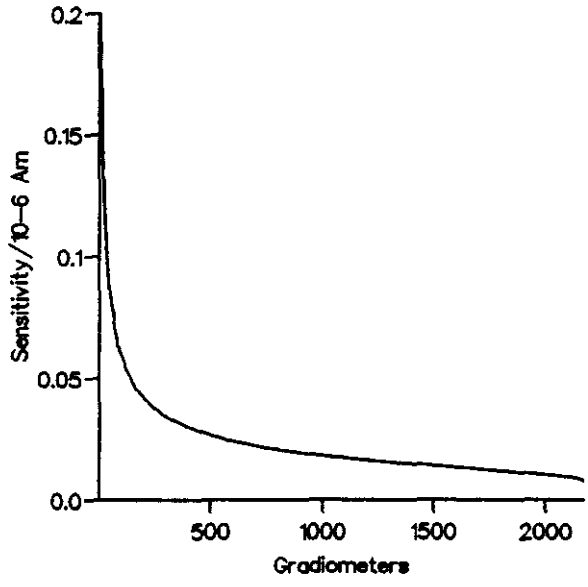

Figure 3.7 Sorted graph of the dipole sensitivities of all 2171 gradiometers.

```
This is a maximisation of sensitivity to a bare dipole.
Distance to source (cm):5.00

Current noise in input coil: 1.20000E-12
Input coil inductance: 7.00000E-07
Maximum number of turns: 4 4 4
coil width (cm):2.20
Maximum coil length (cm):4.00
Total device length (cm):8.00
Wire radius (microns):25.00
z step (cm):0.25
Coil tightness:0.00 0.00 0.00
************************************************************
    .
    .
    .
************************************************************
Optimisation finished  2-OCT-1990 at 12:37:45.75

Results of parameter hunt
-------------------------
Most sensitive gradiometer is number 846.
Which is:-
```

```
N1=2
N2=1
N3=1
Z0=5.00
Z1=6.00
Z2=6.75
Z3=10.75
Z4=11.00
Z5=13.00

Inductance is  5.62779E-07 henries.
Dipole sensitivity is  2.79583E-10 Am at a depth of 5.0 cm
Signal to noise parameter is 375049
**************************************************************
```

One interesting thing about the chosen gradiometer is that it is identical to OPTBIG2, but the number of turns on each coil has been halved. This is because the input coil inductance of these DC SQUIDs is only 0.7μH, and the optimisation has tended to pull the design towards an inductance matched device. Note also that although the intrinsic noise in the SQUID is 100 times better in these SQUIDs, the dipole sensitivity is only 28 times better (still a remarkable improvement!). This is due to a combination of two effects. Firstly as the inductance matching criterion is rather strong, the number of turns on the coils has been halved, and hence the total amount of flux gathered by the gradiometer has also halved. Secondly, with these SQUIDs the coupling between the input coil and the SQUID loop is rather weak i.e the mutual inductance is only $2.88 \times 10^{-9} H$. We can write the flux transformer equation 2.12 as follows

$$\Phi_{SQUID} = F \sum N_i \Phi_i \tag{3.48}$$

Where F is known as the flux transformer factor and is equal to $\frac{M}{\sum L}$. It quantifies the fraction of flux gathered by the gradiometer which is carried into the SQUID loop. For our RF SQUIDs and OPTBIG2, $F = 4.5 \times 10^{-3}$ while for the DC SQUID and the above gradiometer, $F = 2.3 \times 10^{-3}$ i.e. the RF SQUIDs get roughly twice as much flux from the gradiometer.

The combination of these two effects means that the DC SQUID and gradiometer configuration is only 28 times more sensitive, rather than 100 times.

The numerical optimisation algorithm was also used to design a gradiometer for a test thin film project (see chapter 7). The design limitations for this device came again from the dewar tail size but also there was a severe size restriction which came from the silicon wafers that the device is constructed on. For the thin-film laboratory we used, the wafers are 3 inches in diameter and the total device length, Z_{total} was restricted to 5 cm. Shown below is an extract from the log file for this optimisation

```
*****************************************************************
Optimisation started  2-OCT-1990 at 14:12:49.90

This is a maximisation of sensitivity to a bare dipole.
Distance to source (cm):5.00

Current noise in input coil: 2.00000E-11
Input coil inductance: 2.00000E-06
Maximum number of turns: 4 4 4
coil width (cm):1.80
Maximum coil length (cm):3.00
Total device length (cm):5.00
Wire radius (microns):25.00
z step (cm):0.25
Coil tightness:0.00 0.00 0.00

*****************************************************************
Num  n1 n2 n3     z1    z2    z3    z4    z5  induct    sensitivity
-----------------------------------------------------------------

1:1   1  1   5.50 5.50 6.25 7.00 7.25   1.43261E-07  1.91741E-07
     .
     .
     .
543:4 4 4 6.00 6.50 8.50 9.00 10.00   3.53727E-06  1.91827E-08
544:4 4 4 6.25 6.25 8.75 8.75 10.00   3.99595E-06  1.99809E-08
*****************************************************************

Optimisation finished  2-OCT-1990 at 14:20:50.00

Results of parameter hunt
-------------------------
Most sensitive gradiometer is number 442.
Which is:-

N1=3
N2=3
N3=3
Z0=5.00
```

```
Z1=6.00
Z2=6.50
Z3=8.50
Z4=9.00
Z5=10.00

Inductance is  1.98971E-06 henries.
Dipole sensitivity is  1.84287E-08 Am at a depth of 5.0 cm
Signal to noise parameter is 599148
************************************************************
```

Surprisingly, the optimisation picked a design with the same number of turns on all three coils. This is probably because if there were too many turns on the bottom coil (to enhance sensitivity to close sources), there would be insufficient space to accommodate the two larger middle and top coils that would be needed to balance the gradiometer. The particular number of turns i.e. 3 reflects the move towards an inductance matched device.

As expected the dipole sensitivity is around 2 times worse than that for OPTBIG2, but this insensitivity is offset to a certain extent by a high signal to noise factor of close to 600000.

Thin-film gradiometers are usually restricted to single turn coils as multi-turn coils have to be fabricated as flat spirals. These are difficult to balance, unless line integral methods are employed (section 3.1.2). Our approach was to use the numerical optimisation procedures to design the gradiometer (as if it were constructed from multi-turn, rectangular coils), and then use line integral determination of the balance to slightly adjust the critical dimensions to perfect the balance. More details of the design and construction of this device are outlined in chapter 7

If a gradiometer is restricted to 1 turn on each coil, then not surprisingly the optimum gradiometer is one where all three coils are expanded to totally fill the available space i.e. in our notation a balanced gradiometer would have $Z_1 = Z_2 = Z_0 + \frac{Z_{total}}{4}$, $Z_3 = Z_4 = Z_1 + \frac{Z_{total}}{2}$ and $Z_5 = Z_4 + \frac{Z_{total}}{4}$. These simpler thin-film gradiometers have been investigated in simulation using the optimisation algorithm. They are ideally suited to the DC SQUIDs mentioned earlier. This is because they cannot hope to inductance match to the RF SQUIDs with their $2\mu H$ input coil. Shown below is an extract from the log file for these devices.

```
************************************************************
Optimisation started  2-OCT-1990 at 15:23:45.76

This is a maximisation of sensitivity to a bare dipole.
Distance to source (cm):5.00

Current noise in the input coil: 1.20000E-12
```

```
Input coil inductance: 7.00000E-07
Maximum number of turns: 1 1 1
coil width (cm):1.80
Maximum coil length (cm):2.50
Total device length (cm):5.00
Wire radius (microns):25.00
z step (cm):0.25
Coil tightness:0.00 0.00 0.00


**************************************************************
Num   n1 n2 n3  z1    z2    z3    z4    z5   induct      sensitivity
--------------------------------------------------------------

1:1   1   1    5.50 5.50 6.25 7.00 7.25  1.43261E-07  4.52641E-09
2:1   1   1    5.50 5.50 6.50 6.50 7.00  1.60713E-07  4.97308E-09
.
.
.
26:1  1   1   6.00 6.50 8.50 9.00 10.00 2.21079E-07  7.65814E-10
27:1  1   1   6.25 6.25 8.75 8.75 10.00 2.49747E-07  7.59586E-10
**************************************************************

Optimisation finished  2-OCT-1990 at 15:24:13.89


Results of parameter hunt
-------------------------
Most sensitive gradiometer is number  27.
Which is:-

N1=1
N2=1
N3=1
Z0=5.00
Z1=6.25
Z2=6.25
Z3=8.75
Z4=8.75
Z5=10.00
```

```
Inductance is  2.49747E-07 henries.
Dipole sensitivity is  7.59586E-10 Am at a depth of 5.0 cm
Signal to noise parameter is 597967
*************************************************************
```

The optimum design has a rather good dipole sensitivity (because of the tight matching of the gradiometer to the DC SQUID) and a very good noise rejection figure (because of the small device size). The table below summarises some of the sensitivity results from this chapter.

Type	SQUID	Dipole sensitivity/Am	S/N
Wire/Planar	RF	7.8×10^{-9}	375049
Axial	RF	1.3×10^{-8}	440465
Wire/Planar	DC	2.8×10^{-10}	375049
Thin-film	RF	1.8×10^{-8}	599148
Thin-film, 1 turn	DC	7.6×10^{-10}	597967

These simulations seem to show that the most powerful gradiometers are simple one turn thin-film gradiometers coupled into low intrinsic noise DC SQUIDs and this is indeed the route being followed by many groups [22,27,48]. The main problem with this approach is that the yield on thin-film gradiometers is very low. This is because they are large (compared to most microelectronic devices) and so dirt contamination on the wafer has to be kept to extremely low levels across the whole wafer surface.

Given any particular SQUID (RF or DC), the fabrication mode (one turn thin-film, spiral thin-film, or multi-turn wire-wound) and the physical design constraints, it is possible to come up with an optimum geometry using the procedures described in this chapter. It would be a simple matter to extend the concept of numerical optimisation to other planar geometries (e.g gradiometers measuring the x and y derivatives of B_z), and for other sources, so long as the combination of the gradiometer and source geometry meant that it was possible to identify the position of maximum signal within the test plane.

For gradiometers which produce a signal maximum which varies in position within the test plane, as the dipole depth changes (for example axial gradiometers), this simple type of numerical search will not work and a more complex algorithm would be needed. In principle this can be done, however the run-time for the search may be prohibitive. We have done some preliminary research on 'parallelizing' this type of algorithm on our 30 Transputer array which may make these more sophisticated algorithms more viable.

In this chapter we have looked at the forward problem optimisation of a gradiometer. We shall continue the optimisation theme in the next chapter by considering how effective different gradiometers are at providing the information needed to solve the inverse problem. In simple terms, forward problem optimisation maximises the *quantity* of information (i.e large signals), whereas, with the inverse problem, we are concerned with the *quality* of the information i.e what the gradiometer tells us about a particular current distribution.

Chapter 4

Inverse problem methods and their dependence on gradiometer geometry

In the previous chapter we looked at the optimal design of gradiometers with regard to the forward problem i.e the maximising of the signal that the simulated gradiometer would produce in response to some test current distribution. Having designed a gradiometer which we know will produce a reasonable signal and which has a useful noise rejection characteristic, we now have a further problem to consider; will the gradiometer design perform well in our chosen inverse problem algorithm?

In this chapter we first outline the inverse problem in general terms, and then present a new inverse problem technique that is unique in its ability to produce 'images' of the current density rather than representing the current activity using models such as the single current dipole. The technique was developed here at the Open University.

In the next section we then present some test results on the inverse problem performance of three simulated multichannel systems. Two of the systems use planar gradiometers; one uses an axial gradiometer. For each of these multichannel systems we attempted to recover trial current distributions (consisting of single current dipoles), using our inversion technique. The performance of each system is assessed by the ability to locate the position of each of the dipoles; the recovery of the dipole direction is not studied, but in general this is reproduced more or less correctly.

In the final section we look briefly at how well three simultaneously active dipole sources are recovered by the three different gradiometer systems.

The results of the trial inversions seem to suggest that our inversion method is not particularly sensitive to the type of gradiometer used, but that the distribution of gradiometer positions within the simulated multi-channel system is critical. It should be stated that, at the present time, this apparently *ad-hoc* analysis offers the best way of evaluating the performance of a system comprising an array of gradiometers and our inversion algorithm. In the future it may be possible to develop an analytical formulation which will give a quantitative analysis of such a system. However, at the moment we make no strong claims for the generality of the results in this chapter, rather we show that, before constructing a system, it is possible to evaluate the efficacy of that system using an empirical computer model, and that our inversion technique seems valid for the gradiometer geometries currently being

used (or under development) in our laboratory.

4.1 The biomagnetic inverse problem

The biomagnetic inverse problem can be stated as follows. Given the measurement of the magnetic field (and/or spatial gradients of the magnetic field) outside some living system, can we work back to obtain the primary current density distribution within that system? In general the answer is no, as the problem suffers from non-uniqueness i.e. there are many possible current distributions which could generate the observed signals.

There are several reasons for this non-uniqueness. Firstly, as we saw in chapter 2, any one gradiometer will only be sensitive to 2 out of 3 components of the current density, so some sources are 'silent' for particular detector geometries. Of course, by using many different detectors it is possible to reduce this effect, but in most practical systems the problem of silent sources will remain.

Secondly, the source may be rendered silent by return current cancellation. The systems we study consist of the primary current sources (such as a population of neurons) in a conducting geometry. Return currents are set up in the conducting medium and these currents generate a magnetic field which can mask the field from the primary source. Consider the situation shown in figure 4.1. The heavy arrow represents a primary source such as an active region of the brain, the dotted lines represent the return currents. The head is approximated by a homogeneous conducting sphere. In the configuration shown, with the dipole pointing radially, the return currents are such that they exactly cancel the magnetic field from the primary source [55].

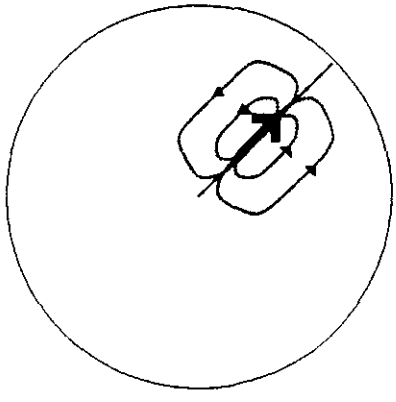

Figure 4.1 A radial primary source, with its associated return currents.

Thirdly, it is possible for a complicated system of currents to mimic the magnetic field from a simple primary source. Figure 4.2 shows a contour map of the radial component of the magnetic field from a dipole tangential to the sphere surface. Again, the heavy central arrow shows the primary source. In this configuration it is easy to associate this field pattern with a single dipolar source. However, this is not the only solution. If the dipole was not present but we had a primary current distribution which was identical to the return currents

that this dipole would generate, then an identical magnetic field map would result. However it is clearly more probable that there is in fact a single localised primary source and this is the generally accepted interpretation . If a magnetic field map is produced which looks as if it is generated by one or more highly localised sources, then the assumption is made that the true generating distribution is a simple localised source (or set of localised sources), even if mathematically there are other valid configurations.

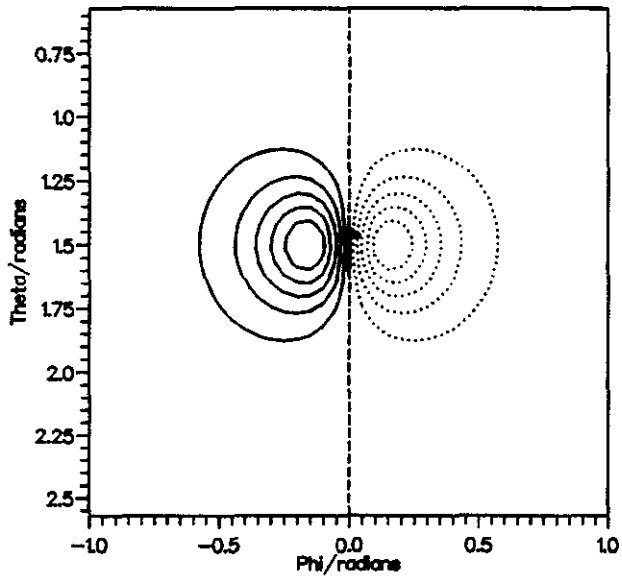

Figure 4.2 Signal from a tangential dipole.

If we restrict the family of possible solutions in this way, then we are adding new *a priori* information to the inverse problem which may destroy the non-uniqueness. Another example of *a priori* information which we might incorporate is the probable location of the sources. If, for example, we are looking at an experiment involving the stimulation of the visual cortex, it seems safe to restrict the sources associated with the response to this region.

The concept of *a priori* information is used in a more formal way in the distributed current inversion technique recently implemented here at the Open University.

4.2 Distributed current analysis

In this section we describe a probabilistic approach to solving the biomagnetic inverse problem that can produce 'images' of the primary current density in a specific region of the brain.

In the past the biomagnetic inverse problem has usually been solved by modelling the target current distribution as a single current dipole. The inversion then consists of a least squares algorithm, which seeks to find the dipole which is most consistent with the observed signals. Of course, this model is only valid if the generating activity is a single, localised region, and in practice there are many occasions where a single dipole is not appropriate [34]. More sophisticated algorithms try to fit multiple current dipoles to the data; such a

system is described in chapter 5. However even this assumption (of multiple, highly localised sources of activity) may be incorrect.

In the distributed current analysis (DCA) method, the rather artificial model of current dipole sources is dropped in favour of a more general current distribution. The primary currents are constrained to lie within some source space, and probabilistic arguments are used to find the expectation of the current distribution, given all the *a priori* information. The advantages are threefold. Firstly, the method can analyse magnetic field maps which are clearly non-dipolar in origin. Secondly, the method can in principle be used with any detector geometry and, hence, can be used to invert data from planar and axial gradiometers. Finally, and perhaps most importantly, the method provides an 'image' of the current density over a whole region, and this, together with time evolution of the image, provides a uniquely powerful way of visualising activity in the cortex.

This probabilistic approach was first introduced by Hämäläinen [35], was developed further by Clarke and Janday [36], and a working imaging system was developed here at the Open University by Ioannides et al [37].

The magnetometer readings and any physiological information which might be available is considered as partial information about the source and can be represented as a probability distribution over the space of all possible source configurations.

If we have a set of detectors measuring the field from an unknown current distribution, $\mathbf{j}(\mathbf{r})$, constrained to lie within a region Q, the signal m_i from detector i can be written as follows

$$m_i = \int_Q \boldsymbol{\phi}_i(\mathbf{r}) \cdot \mathbf{j}(\mathbf{r}) d^3r \tag{4.1}$$

Where the $\boldsymbol{\phi}_i(\mathbf{r})$ are a set of vector valued functions known as the lead fields. The lead field for a particular detector is defined at all points in space and relates the sensitivity of that detector to a current element at a point. They can be found by solving the above forward problem for delta function sources.

As these functions define precisely which current sources the detectors are sensitive to, it is convenient to express the current solution as a linear combination of these lead fields. Although we could choose any basis set, it is appropriate to use the lead fields as this ensures that the contribution of silent sources vanishes. The current density can then be written in the following form,

$$\mathbf{j}(\mathbf{r}) = \sum_{k=1}^{s} A_k \boldsymbol{\phi}_k(\mathbf{r}) w(\mathbf{r}) \tag{4.2}$$

where $w(\mathbf{r})$ is the *a priori* probability density function, and s is the number of measurements.

Combining equations 4.2 and 4.1 gives a set of linear equations which can be inverted to give the A_k and hence the current density:-

$$P_{ik} = \int_Q \boldsymbol{\phi}_i(\mathbf{r}) \cdot \boldsymbol{\phi}_k(\mathbf{r}) w(\mathbf{r})\, d^3r \tag{4.3}$$

$$m_i = \sum_{k=1}^{s} P_{ik} A_k \tag{4.4}$$

If we have a large number of measurements (and hence $\phi_i(\mathbf{r})$ functions), the inversion can run into numerical difficulty. This is because some of the basis functions will be close to linear combinations of other basis functions, making the matrix P very nearly singular. There are three possible approaches to solving this problem.

Firstly, we could simply drop a set of measurements and their associated basis functions. This is obviously not desirable as we are ignoring potentially useful information. Secondly, we could construct a linear combination of the basis functions to generate a new, orthogonal set of basis functions [35]. This approach has the disadvantage that if we want to change the probability weight, or use the solution as a probability weight for a new inversion (see below), we must re-compute a new set of orthogonal basis functions. A more elegant solution used at the Open University is to use regularisation i.e. we add an extra term to the matrix equation. This prevents numerical difficulties.

The matrix equation is then written in the following form

$$\tilde{m}_i = \sum_{k=1}^{s} \tilde{P}_{ik} A_k \qquad (i = 1 \ldots s) \tag{4.5}$$

where the quantities $\tilde{m}_i$ and $\tilde{P}_{ik}$ are defined by

$$\tilde{m}_i = \sum_{k=1}^{s} P_{ik} m_k \quad , \quad \tilde{P}_{ik} = \sum_{j=1}^{s} P_{ij} P_{jk} + \zeta P_{ik} \tag{4.6}$$

The extra term has the additional effect of smoothing the solution and can be controlled by our choice of ζ. We could imagine making ζ as small as possible without encountering problems with a singular matrix. However, the smoothing effect can be considered as spatial filtering which may be beneficial. It can be shown from probability arguments ([39]) that ζ is in fact equal to σ^2/kJ_{max}^2. J_{max} is the maximum current density that we allow in our solution, and is set by physiological constraints. The σ term is a measure of the noise in the measurements to be inverted, and k is a known constant. Given J_{max} and σ we can therefore calculate an optimum value for ζ.

For the sake of simplicity we introduce the parameter $\bar{\zeta} = \zeta s/TrP$. Then, $\bar{\zeta} = 1$ represents the mid-point between large and small values of ζ. It has been shown that around this point, the solutions are rather independent of the actual value of ζ [38].

One problem with the distributed current approach is that when the signal is produced by a highly localised source (such as a current dipole), the solution chosen tends to be a more distributed one than the true solution. So it might seem that we have simply traded one problem for another. Instead of having an inversion system which is only valid for a highly localised source, we now have a method which seems to be inappropriate when the sources are localised.

However, the problem can be cured to some extent by *iteration*. In this approach we use our initial solution as the *a priori* probability weight for a new inversion of the data.

This has the effect of reinforcing any regions of high activity in the original solution, at the expense of other regions within the solution space, and hence localises the solution to a greater extent.

Using iteration, DCA can localise current dipoles almost as well as a method specifically designed to look for these types of sources [38].

4.3 Trial inversions using different gradiometer geometries

The aim of the section is to see if the particular choice of gradiometer significantly affects the ability of DCA to locate active regions within the head. We have chosen to look at three different types of gradiometer; the planar geometry in use at Helsinki University of Technology, the standard SHE axial gradiometer currently in use in our laboratory, and the OPTBIG2 planar gradiometer which is to be used in our 3 channel system.

A comprehensive analysis of how DCA is affected by the choice of gradiometer is outside the scope of the thesis, here we look at a restricted problem i.e. the location of a single active region (represented by a single current dipole). For each geometry we shall perform three separate inversions with the dipole at three different positions. We shall also show how iteration improves the localisation of the dipole.

Although full three dimensional source spaces can be handled by our inversion system, these can be very time-consuming. Instead, we have chosen to use the fact that most detectors are preferentially sensitive to the cortical surface close to the detectors. We use a two-dimensional disk to represent the primary source-space, positioned and oriented at a reasonable distance from the detectors. The solution can then be thought of as a projection of the true current distribution onto this disk. To recover depth information, we move the source space to various positions on the depth axis, perform an inversion at this level and then solve the forward problem for this solution and detector geometry under study. These simulated data are compared with the actual data to give a standard deviation. Ioannides et al have shown [38] that the standard deviation usually shows a minima when the source space is postulated close to the true depth of the primary sources.

In these trials, we have chosen a set of three current dipoles as our target current distribution. Dipoles are used because we know that DCA is not particularly suited to this type of distribution and, therefore, that this is a stringent test of the inversion system. We have chosen the three dipoles so that all three are contained in a plane which is roughly parallel to each array of gradiometers. In this way we can split our investigation of the localisation into two parts; Firstly, we look at how well DCA recovers the lateral position within the plane. This will indicate if there is a significant variation in localisation accuracy with the lateral position of the dipole.

Secondly we look at how easy it is to recover the true depth (which should be the same for all three dipoles). Again, this will indicate if dipoles at the edge of the source plane are harder (or easier) to locate in depth than more central ones.

All of the inversions are carried out using a conducting sphere geometry, with the centre

of the sphere roughly 10 cm below the plane of detectors. The simulations were carried out assuming no noise.

In the first trial we look at the Helsinki 24 channel system.

4.3.1 The Helsinki 24 channel system

We now investigate the use of DCA in inverting data from the 24 channel system developed at the Helsinki University of Technology [40].

The gradiometers used in this system are first order planar gradiometers measuring either $\partial B_r/\partial\theta$ or $\partial B_r/\partial\phi$. Figure 4.3 shows the form and dimensions of one of these devices. The 24 sensors are arranged in 12 modules, with each module containing one gradiometer measuring the θ derivative, and one gradiometer measuring the ϕ derivative. In this sense the Helsinki system can be considered either as a 24 channel system, or a 12 channel 'vector' system. The 12 modules are uniformly distributed over a spherical surface with radius of curvature 12.5 cm. The detectors cover an area of approximately 12.5 cm in diameter. Note that, in the notation above, the r direction is the local normal to the curved surface, for each gradiometer module.

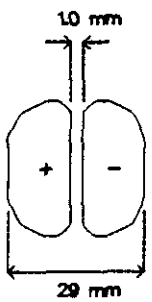

Figure 4.3 First order planar gradiometer, used in the Helsinki 24 channel system.

To test the distributed current analysis method for this system, we constructed in simulation a set of three current dipoles. Figure 4.4 shows the geometry used in the inversions. The curved surface represents the surface over which the detector modules are distributed, the source disk is the plane containing the dipole sources.

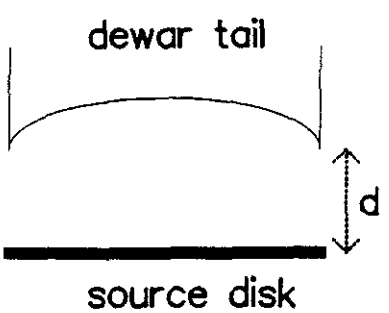

Figure 4.4 Source disk and detector geometry for the trial inversions.

The first test had d=3 cm i.e the three dipoles were fairly superficial and are contained in the source disk plane, roughly normal to the gradiometers' axes. If we perform an inversion

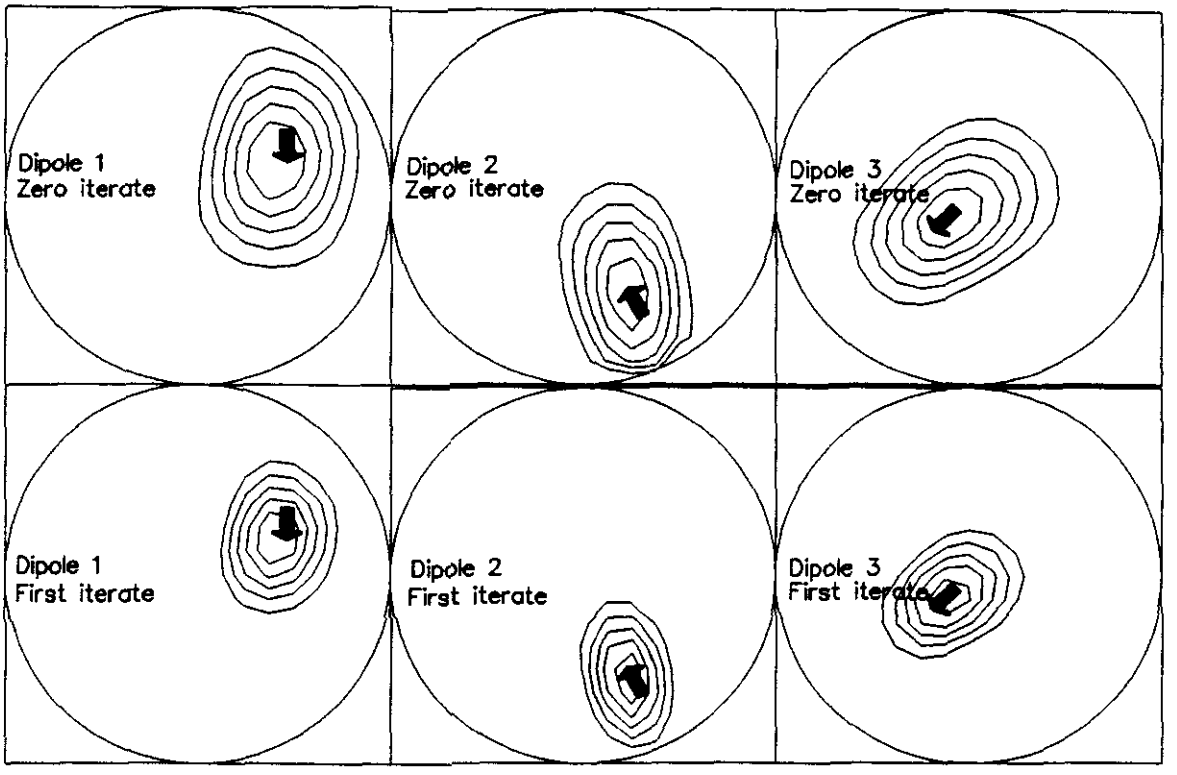

Figure 4.5 Helsinki geometry, current density solutions, zero and first iterates, d=3cm.

assuming that we know the depth distance d correctly we obtain the solutions shown in figure 4.5. We show the current density solutions as a set of contour maps which represent the magnitude of the current density. The heavy black arrows represent the dipole sources, and the circle represents the edge of the source disk. Note how the iterated solutions (bottom row of three contour maps) are 'tighter' than the non-iterated solutions.

For each contour plot, we can use the maxima as our postulated location of the current dipole. This gives the following errors in dipole locations,

Dipole	Error (zero iterate)/cm	Error (first iterate)/cm
1	0.6	0.4
2	0.3	0.1
3	0.1	0.1

The dipoles are located in the source plane to an accuracy of at worst, 0.6 cm, with higher accuracy achieved using iteration. The use of iteration is more than just a procedure to improve the 'sharpness' of the image (squaring and re-normalising the solution would have a similar effect), but seems to increase the amount of valid information in the final solution, if we are certain that the features within the current solution should be localised. At the moment the decision to use iteration is controlled entirely by the operator, but an extension to the system might include the use of an expert system to decide whether there are localised sources within a particular image.

The above solutions were performed assuming the correct depth, d, for the source disk and in a real situation we would need to estimate this. Figure 4.6 shows a plot of the

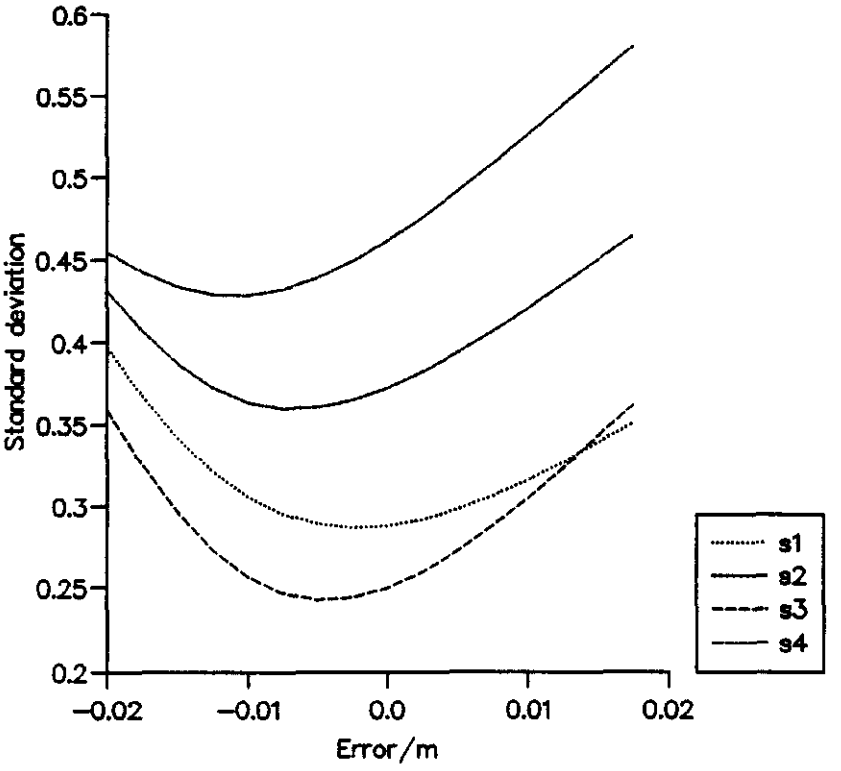

Figure 4.6 Helsinki geometry, depth estimates, zero iterate, d=3cm.

standard deviation (between the calculated measurements and the actual measurements) as a function of the positional error for the zero iterate. Figure 4.7 shows the corresponding curves for the first iterate solution.

The 4 curves (s4 corresponds to all 3 dipoles being active) show minima close to the true position of the sources, but the estimates of the depth using this solution would all be smaller than the true value. The actual errors in the depth parameter would be

Dipole	Error (zero iterate)± 0.25 / cm	Error (first iterate)± 0.25 / cm
1	-0.25	-0.5
2	-0.75	-0.5
3	-0.5	-1.0
all 3	-1.0	-1.0

This seems to show that the non-iterated solution is slightly better at estimating the true depth. Note that we do seem to be able to recover the depth when all three sources are active, although the accuracy is not as great. In section 4.4 we discuss the imaging of all three sources in more detail.

Similar inversions were performed for d = 5cm, and the solutions are shown in figure 4.8. Note how the solutions are less localised than the corresponding solutions for the 3 cm case, but again iteration has improved the 'tightness' of the localisation. The lateral errors in the dipole position were

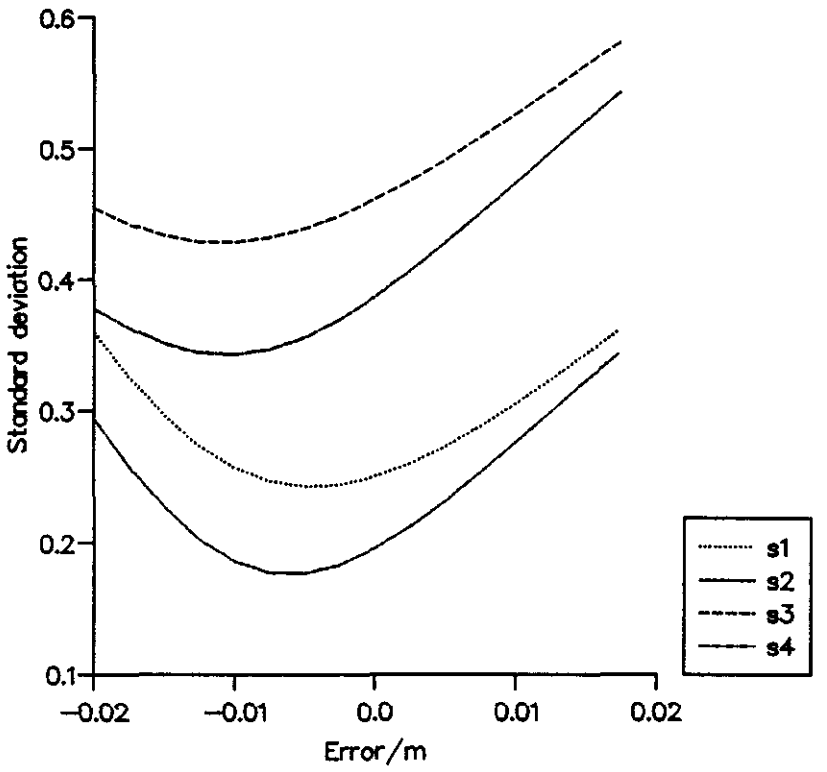

Figure 4.7 Helsinki geometry, depth estimates, first iterate, d=3cm.

Dipole	Error (zero iterate)/cm	Error (first iterate)/cm
1	0.9	0.9
2	1.0	0.7
3	0.4	0.4

As before, the first iterate has slightly improved the accuracy of the lateral position estimate for the second dipole.

The errors on the depth parameter are calculated as before,

Dipole	Error (zero iterate)± 0.25 / cm	Error (first iterate)± 0.25 / cm
1	-1.0	-1.0
2	-1.25	-0.75
3	-1.0	-2.0
all 3	-2.0	-2.0

To see how the actual distribution of the detectors affects the kind of accuracy we can get from these inversions, we constructed in simulation a hypothetical variant on the Helsinki system with the gradiometer modules twice as far apart as the actual design. At first sight this is a rather attractive design as the array then covers a larger fraction of the area of the head (and is thus sensitive to more of the brain's surface). However, the lead field functions for each gradiometer are then quite far apart and do not overlap to the same extent. This results in sources appearing in the solutions preferentially closer to the detector positions

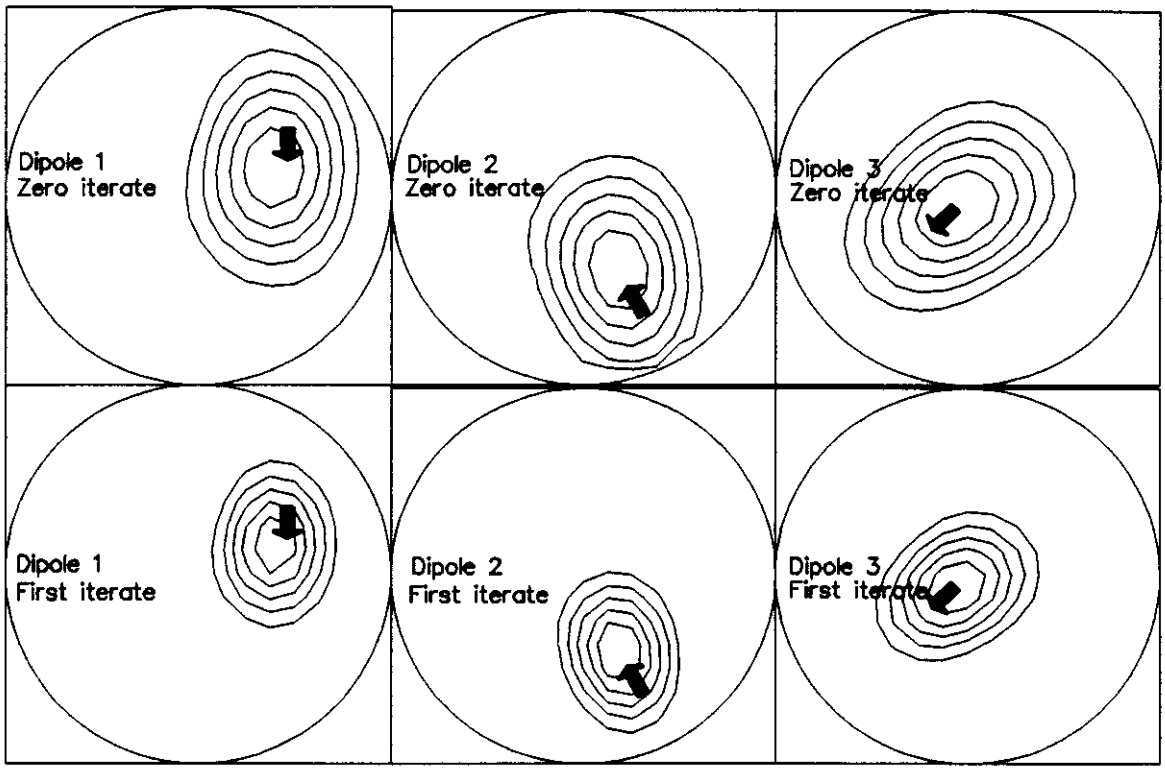

Figure 4.8 Helsinki geometry, current density solutions, zero and first iterates, d=5cm.

than their true position. For the d=3 cm case studied earlier the lateral errors varied between 1.6 cm and 2.3 cm for the same three dipoles.

The design of multichannel systems so that the lead fields are optimally placed is a rather complicated problem, but one approach is to use some of the ideas of Information Theory [41].

Summary

In the trial inversions we performed for this system, the first iterate was the most accurate at finding the lateral position. However, in the depth estimates, the non-iterated solution usually gave the best results. With the dipole sources roughly at the superficial level of the visual cortex, the lateral errors were less than 0.5 cm, while the depth was estimated to an accuracy of around 1cm. For a deeper set of sources, these errors were roughly doubled.

It should be noted that although the dipole orientation was not studied in detail, the orientations of the sources were reproduced reasonably well.

4.3.2 An array of symmetric axial gradiometers

In this next subsection, we present results from the same trial sources carried out using data from a hypothetical multichannel system. This consists of a regular array of second order axial gradiometers (SHE gradiometers as described earlier). In the first test using these gradiometers we used a 4x4 matrix of gradiometers.

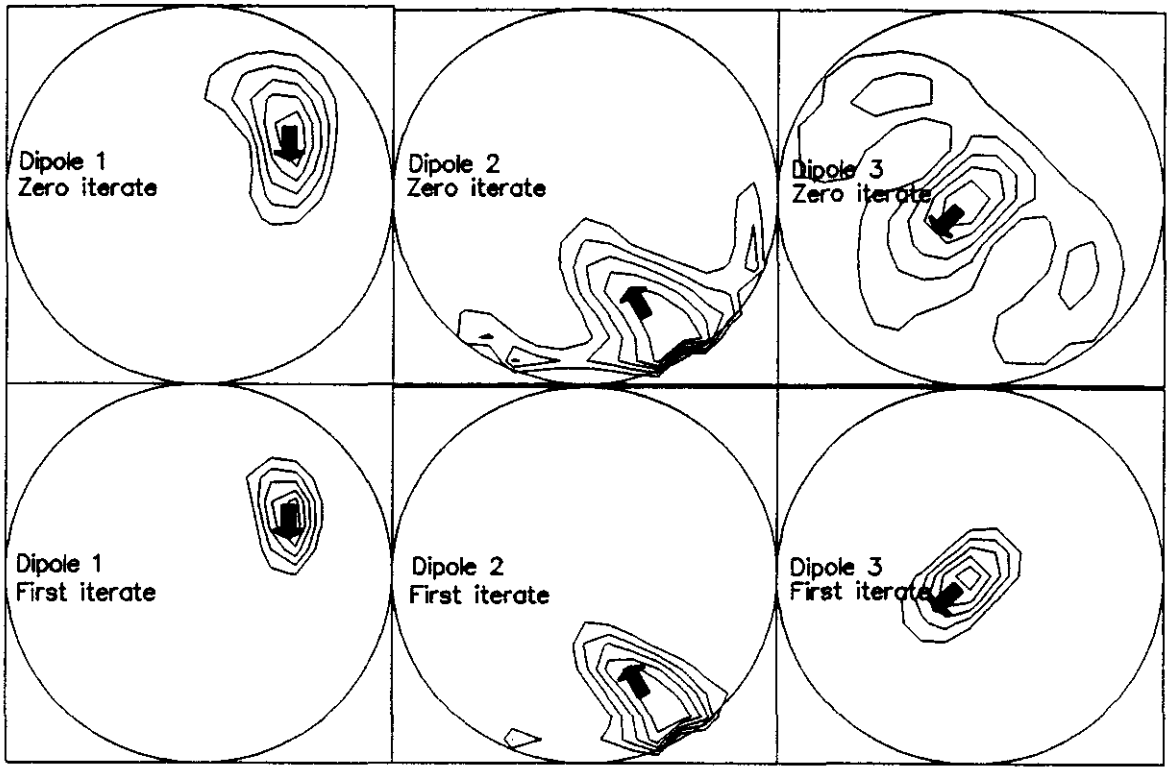

Figure 4.9 Axial geometry, current density solutions, zero and first iterates, d=3cm.

The detector geometry was similar to that used for the Helsinki system except that, for the sake of simplicity, the detectors were distributed on a plane rather than a curved surface. The detectors were uniformly spaced in x and y by 3 cm, giving a coverage area of diameter 11cm (including the width of the coils).

Figure 4.9 shows the zero and first iterate solutions for d=3 cm, using a conducting sphere. The solutions are less localised than the solutions for the Helsinki system, although the first iterate does improve this. The lateral errors for the zero and first iterates were

Dipole	Error (zero iterate)/cm	Error (first iterate)/cm
1	0.4	0.3
2	1.3	1.5
3	0.5	0.5

Notice how there seem to be significant errors in the solution, occurring around the edge of the source space. This effect has made the error on the lateral location of dipole 2 (which is close to the edge) much larger. Also, iteration appears to have increased the error for this particular dipole.

In contrast, the depth estimates are better than those for the Helsinki system. Figure 4.10 shows the standard deviation/depth graphs for the first iterate estimates. The graphs are more sharply minimised, but again all the estimates are more superficial than the true depth. The errors on the depth estimates for the zero and first iterates are

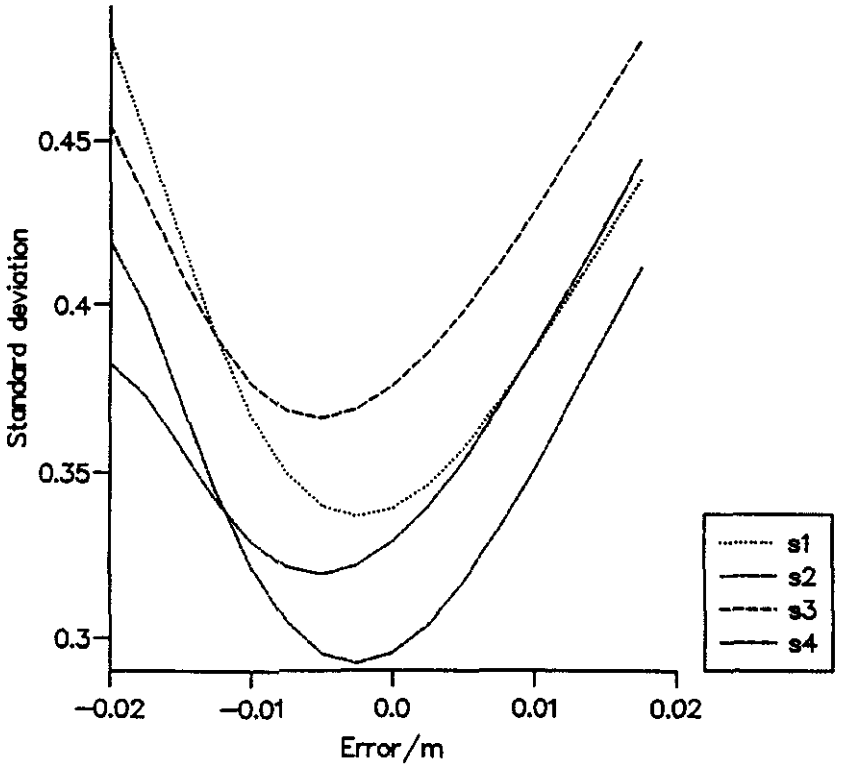

Figure 4.10 Axial geometry, depth estimates, conducting sphere, first iterate, d=3cm.

Dipole	Error (zero iterate)± 0.25 / cm	Error (first iterate)± 0.25 / cm
1	-1.0	-0.25
2	-0.5	-0.25
3	-0.25	-0.5
all 3	-1.0	-0.5

In this system, the first iterate seems to give the best results for the depth localisation.

For the d = 5 cm case, the solutions for the zero and first iterate are shown in figure 4.11. The solutions are poorly localised and now have severe edge errors. However, we can still identify the maxima of the plots and associate this with a dipole. The lateral errors for the zero and first iterates were

Dipole	Error (zero iterate)/cm	Error (first iterate)/cm
1	0.7	0.7
2	2.0	2.0
3	1.1	1.1

Iteration has no effect on the accuracy of localisation. Dipole 3 has the worst edge distortion, with rather large signals around the edge of the source disk. This distortion can be cured to some extent by using an initial probability distribution which falls off from the centre of the disk. Of course this approach could be dangerous as we might be biasing the solution in an inappropriate way. However, if we know the form of the distortion at this level, some judicious use of initial probability weights is justified. It is probably fair to say though, that with this system, it is difficult to make an image at this deep level.

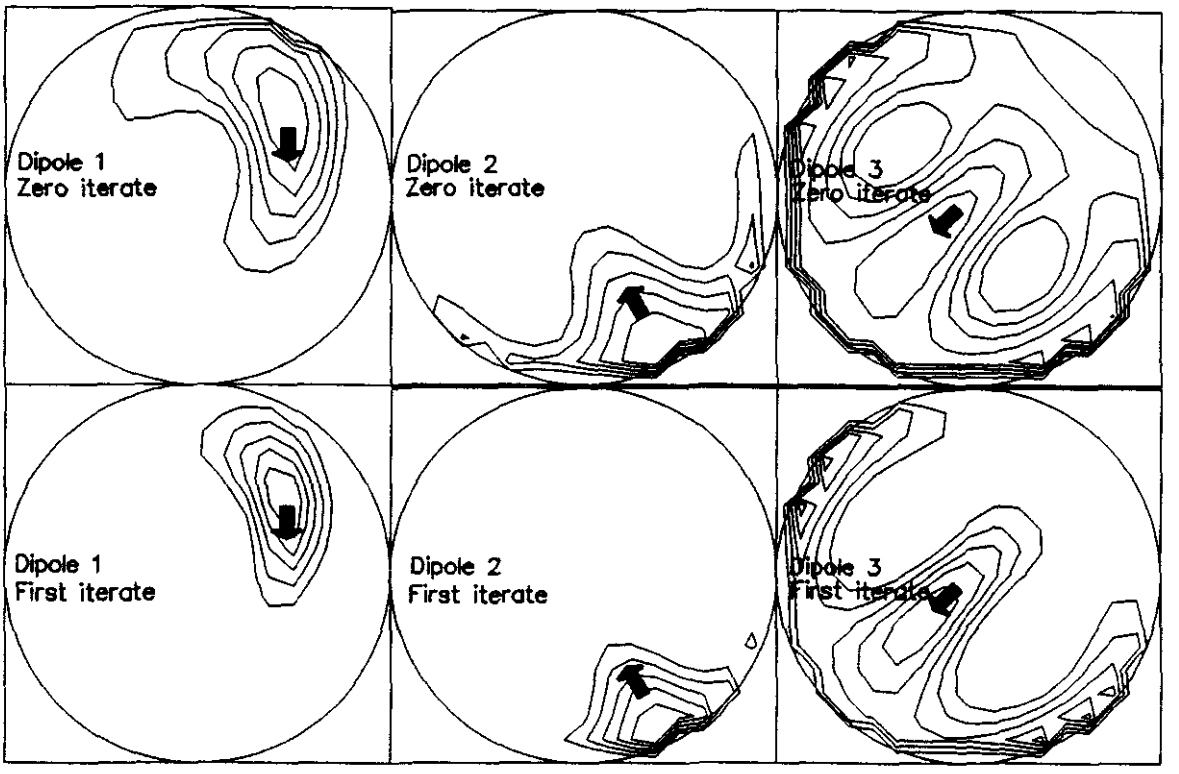

Figure 4.11 Axial geometry, current density solutions, zero and first iterates, d=5cm.

Surprisingly, the depth estimates are still rather good. Figure 4.12 shows the graph for the zero iterate and the corresponding errors on the depth estimates were

Dipole	Error (zero iterate)± 0.25 / cm	Error (first iterate)± 0.25 / cm
1	-0.75	-1.5
2	-0.75	-1.0
3	-1.25	-0.75
all 3	-1.25	-1.25

Note that this time, the zero iterate gives the better depth estimate.

The lateral localisation ability of this system is rather disappointing and is certainly worse than that achieved by the Helsinki system. It might be argued that this is not surprising as we are comparing a 16 channel system with a 24 channel system, but it must be remembered that the Helsinki system actually samples the field at only 12 positions.

We constructed another array of SHE gradiometers, this time in a six by seven matrix covering the same area as before. Figure 4.13 shows the first iterate solution for the d=3cm case. The solution is much 'tighter' with less edge distortion. However, the lateral errors are largely unchanged,

Dipole	Error (first iterate)/cm
1	0.3
2	1.5
3	0.6

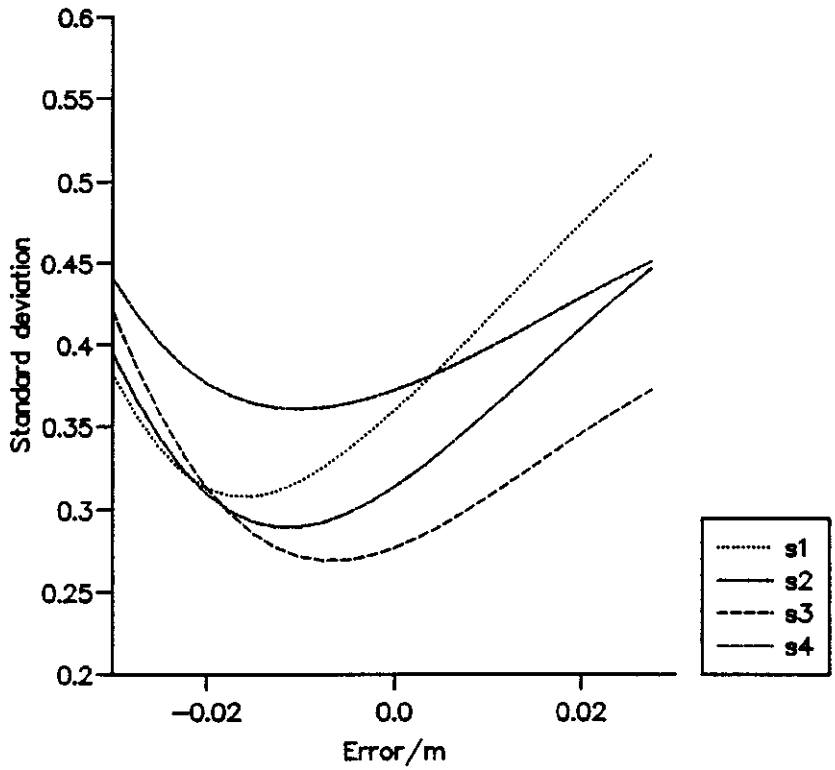

Figure 4.12 Axial geometry, depth estimates, conducting sphere, zero iterate, d=5cm.

Figure 4.14 shows the solution for the d=5 cm case. The lateral errors are

Dipole	Error (first iterate)/cm
1	0.3
2	2.0
3	1.1

So dipole 1 is located with higher accuracy. The amount of distortion in the dipole 3 image is not as pronounced as for the 4x4 array, but is still significant.

Summary

For a few measurements sites, spaced by 3 cm, an array of axial gradiometers was able to locate single dipoles with a lateral positional accuracy of between 0.5 and 1.5 cm in the d=3 cm case, and between 0.5 and 1.6 cm in the d=5 cm case. The depth location errors were of similar magnitude. In terms of providing a true image of the current density, serious distortion effects occurred for the deeper set of inversions.

For this system, the use of iteration seemed to have only a marginal effect on the location accuracy, however the images were sharpened noticeably.

The major problem with this particular array is that the solutions were not highly localised but tended to spread away from the source, especially near the edge of the source disk. This effect is probably due to the relatively large spacing between the detectors. An array of similar gradiometers on a finer, six by seven matrix, covering the same area, gave

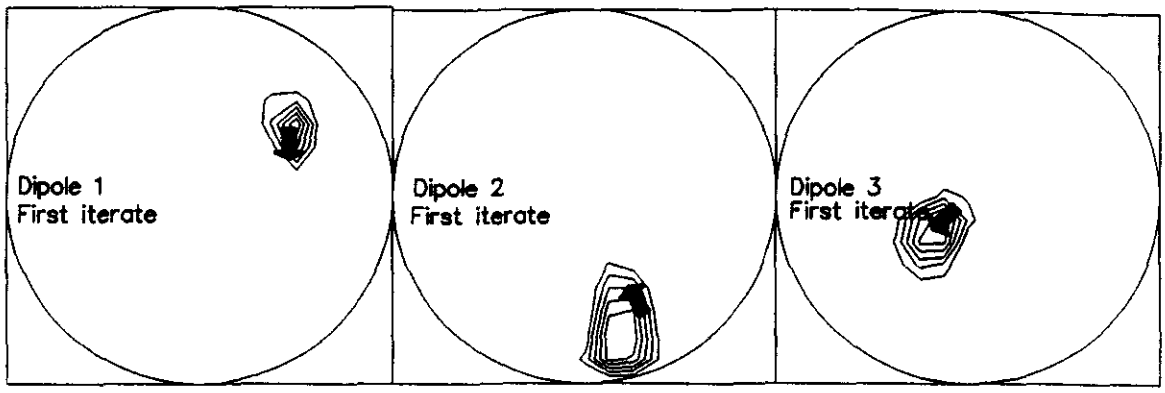

Figure 4.13 6x7 Axial geometry, current density solutions, first iterate, d=3cm.

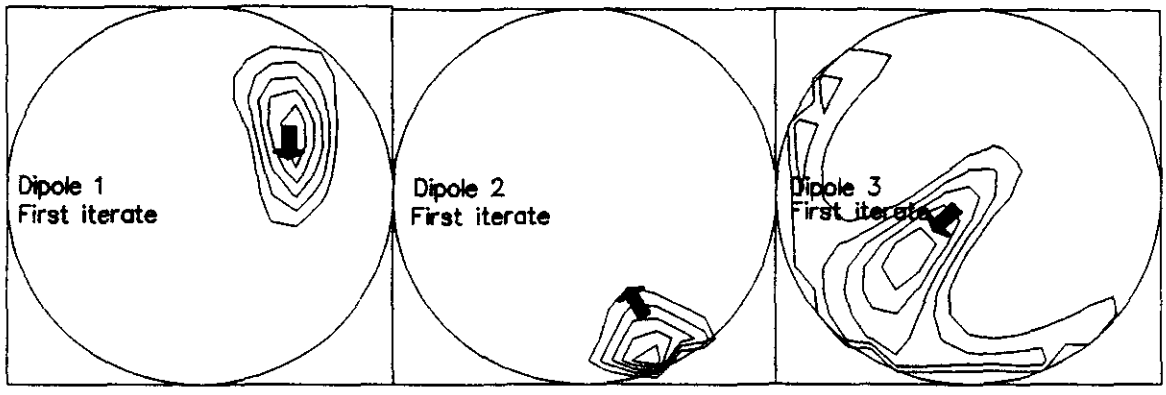

Figure 4.14 6x7 Axial geometry, current density solutions, first iterate, d=5cm.

a much tighter image in which the dipoles were much more localised. This reduced the amount of distortion around the edge of the disk.

This seems to suggest that it is not the *type* of gradiometer that is important, rather their number and distribution.

4.3.3 An array of planar 3 channel probes

In this final subsection we again present trial inversion results, using a planar gradiometer system.

The new three channel system under construction here at the Open University consists of three OPTBIG2 gradiometers (see section 3.2) arranged on the sides of a triangular prism. The probe is shown in figure 4.15. Any experiment carried out with this system would involve moving the probe from measurement site to measurement site and averaging many samples at each site. In this way an array of 3 channel probes can be simulated in the laboratory, however, there is no reason why a full multichannel system could not be constructed.

The same inversion tests were carried out using a 4 by 4 square array of 3 channel probes with the spacing between probe centres equal to 2.5 cm. Figure 4.16 shows the zero and first iterate solutions for the d=3 cm case, in a conducting sphere. The lateral errors for

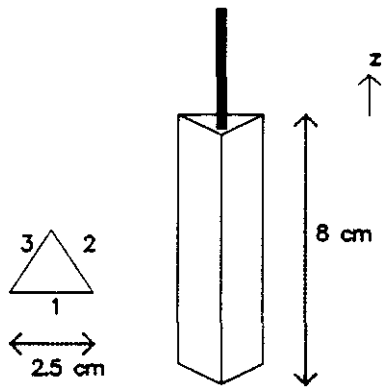

Figure 4.15 The three channel probe.

these two solutions were

Dipole	Error (zero iterate)/cm	Error (first iterate)/cm
1	0.3	0.3
2	0.5	0.1
3	0.0	0.0

So iteration has again tightened the image, and improved the location accuracy of dipole 2. The first iterate depth estimates are shown in figure 4.17 and the errors were

Dipole	Error (zero iterate)$\pm$ 0.25 / cm	Error (first iterate)$\pm$ 0.25 / cm
1	-0.75	-0.5
2	-0.75	-0.5
3	-0.5	-0.5
all 3	-0.5	-0.75

So the first iterate slightly improves the depth localisation.

Figure 4.18 shows the zero and first iterate solutions for the d=5 cm case. The corresponding lateral errors were

Dipole	Error (zero iterate)/cm	Error (first iterate)/cm
1	0.7	0.3
2	2.1	1.6
3	1.6	1.1

So iteration has significantly improved the localisation accuracy, as well as sharpening the image. As with the SHE gradiometers, their are some serious distortions in the images, especially for the central dipole.

The first iterate depth estimates are shown in figure 4.19 and the errors were

Dipole	Error (zero iterate)$\pm$ 0.25 / cm	Error (first iterate)$\pm$ 0.25 / cm
1	-1.5	-0.5
2	-0.5	-0.5
3	-0.5	-1.0
all 3	-1.0	-1.0

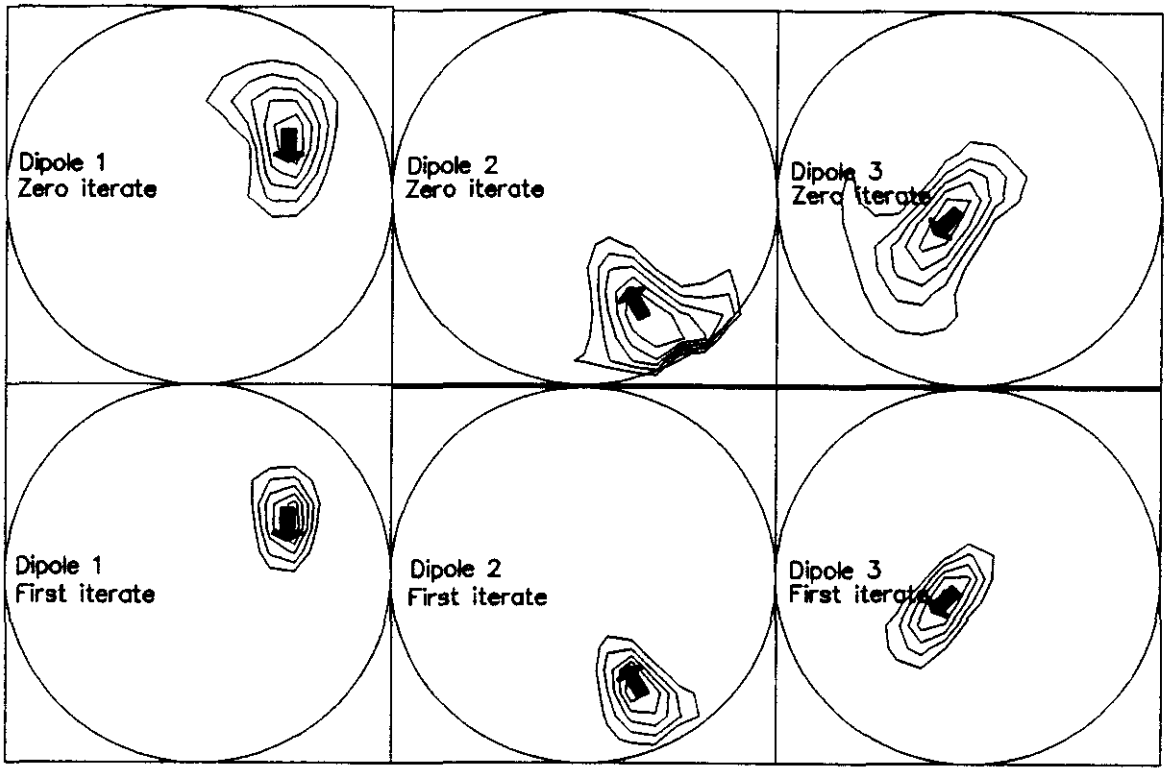

Figure 4.16 Plane of 3 channel probes, current density solutions, zero and first iterate, d=3cm.

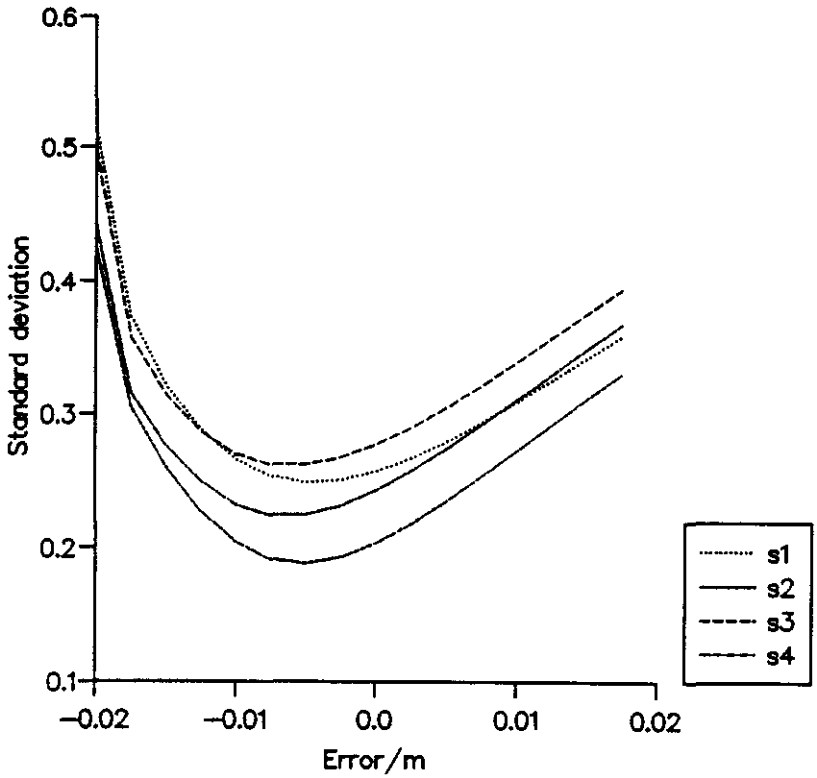

Figure 4.17 Plane of 3 channel probes, depth estimates, conducting sphere, first iterate, d=3cm.

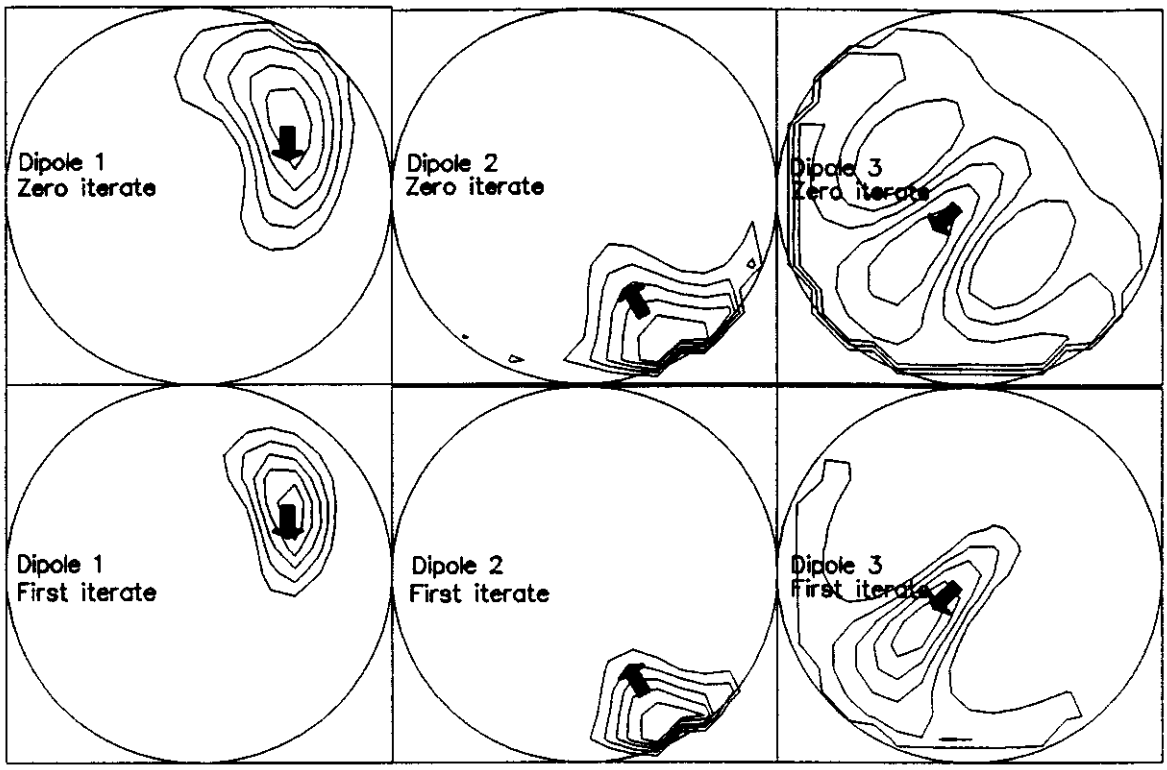

Figure 4.18 Plane of 3 channel probes, current density solutions, zero and first iterate, d=5cm.

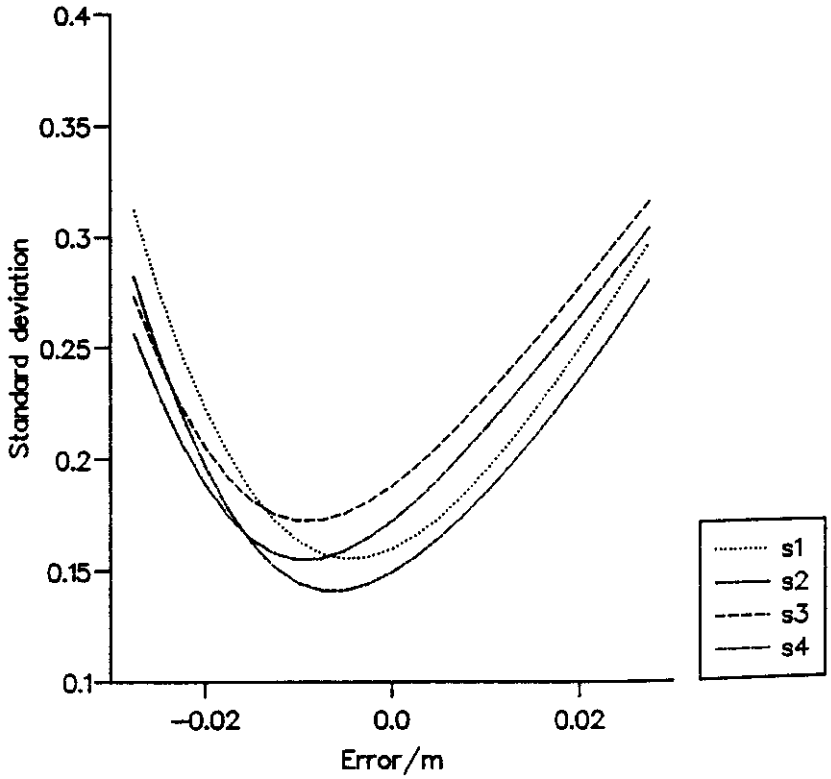

Figure 4.19 Plane of 3 channel probes, depth estimates, conducting sphere, first iterate, d=5cm.

Summary

A four by four array of these 3 channel probes seems to be rather good at localising separate dipolar sources. In the superficial d=3 cm case, the lateral errors were between 0.3 cm and 0.5 cm, with the first iterate giving the better localisation. The depth localisation errors varied between 0.5 and 0.75, with the familiar 'pull' towards a more superficial solution. Iteration did not make a significant impact on this.

In the deeper 5 cm case, the lateral errors varied between 0.7 and 2.1 cm, with iteration improving this to between 0.3 and 1.6 cm. The depth errors were between 0.5 and 1 cm with again iteration making only a slight difference. For the central dipole, there was some distortion of the image, with activity being spread to the edge of the disk.

4.4 Trial inversions with three simultaneously active dipoles

In the previous section, we showed how the three different gradiometer systems were able to recover single dipolar sources. Of course, in the brain there might be more than one region active at the same time and so we need to investigate whether the different systems would be able to resolve these regions. We have already mentioned briefly that when the three dipoles were all activated, it was still possible to gain a reasonable estimate for the depth. In this section we look at the current density images which DCA produces, at the superficial d=3 cm level. We have chosen to look only at the superficial case as we already know that there are serious problems in making an image of the current density at deeper levels than this.

It is worth emphasizing that this is an even more extreme test for DCA than single dipole localization. Figure 4.20 shows a set of 4 colour contour plots for the 4 systems looked at in the previous section. We show the zero iterate because iteration in this case might lead to over-emphasis of one particular source at the expense of the others.

The Helsinki system clearly has trouble resolving two of the three sources. This is almost certainly because the system only measures the field at 12 discrete points. However, even though it has failed, the image is not totally misleading as it has elongated the single dipole region in the bottom right of the image into a larger region. What also must be remembered is that the current dipole is physiologically unreasonable and in reality the active regions within the brain would be distributed over a finite space. DCA would find it much easier to recover these kinds of distributions.

The 4x4 array of SHE gradiometers manages to miss completely the dipole in the bottom right of the picture. The fact that this is because of the small number of measurement sites is graphically illustrated by the contour map for the 6x7 array, which clearly shows the presence of the three areas of activity.

The array of 3 channel probes seems to provide a very good image of the current density, with three discrete maxima close to the true dipole positions.

4.5 Conclusions

The trial inversions we have presented here do seem to suggest that the distributed current analysis method can be used irrespective of the gradiometer geometry, especially for superficial sources (d=3cm). At the deeper level, problems were encountered with the SHE gradiometer and the OPTBIG2 gradiometers, with the image of the current dipole being spread out towards the edges of the disk. This might be correctable with careful use of an initial Gaussian probability weight.

Although the inversion technique is more suited to finding distributed source distributions, the trial inversions we present here seem to show that iteration can be used to locate dipolar like sources. The actual type of gradiometer (axial, planar, tangential or radial) does not seem to affect significantly the location accuracy (of the order of 1 cm), but the actual distribution of detector positions is critical. The detectors must be close enough to have a significant amount of overlap in their lead field functions, otherwise the solution is pulled toward the detector positions. With sufficient numbers of carefully placed detectors, a good image of the current density can be obtained for superficial sources. For deeper sources the construction of an accurate image is much more difficult.

One difference between various gradiometers seemed to be in the depth calculations. The Helsinki system produced standard deviation curves which were not as sharp as the other two gradiometers studied. The reason for this is not clear but may be because the baseline of the Helsinki gradiometers is small i.e. the device is not very sensitive to deep sources.

The depth calculations always seem to provide a solution which is more superficial than the true depth. It may well be that some correction regime may be developed in the future.

What seems clear is that, at the moment, a full understanding of this method is in its infancy so there is no substitute to performing trial solutions with a particular experimental geometry before inverting real data. These will give a clear understanding of the kind of localisation accuracy we can expect, and what iteration regimes are appropriate.

For example in chapter 6 we present the results from an experiment carried out using the Helsinki system. The trial inversions seem to tell us that we can laterally locate primary regions of activity to within 0.5 to 1 cm, and find the depth to around 0.5 to 1.0 cm. The presence of more than one active region should be clear, if the regions are not too close together. However, perhaps it should be pointed out that this method allows the time-evolution of the current density to be studied, in the form of an image. So its primary strength is not in its ability to locate dipolar like active regions (although it does seem able to do this), but the investigation of how active regions develop in time.

The ability of our system to produce these images with a very high time resolution does create another difficulty as there is a huge amount of information contained within the solution set. To make maximum use of this information, we need to develop software tools which present the information in an easily understandable format, and make clear the dynamic evolution of active regions.

In the next chapter we describe such a software tool, IMAGE, that we have developed to deal with this specific problem. We also describe other large software systems that have been developed, and which we consider to be essential in the analysis and presentation of the large amount of data generated by multichannel biomagnetic measurements.

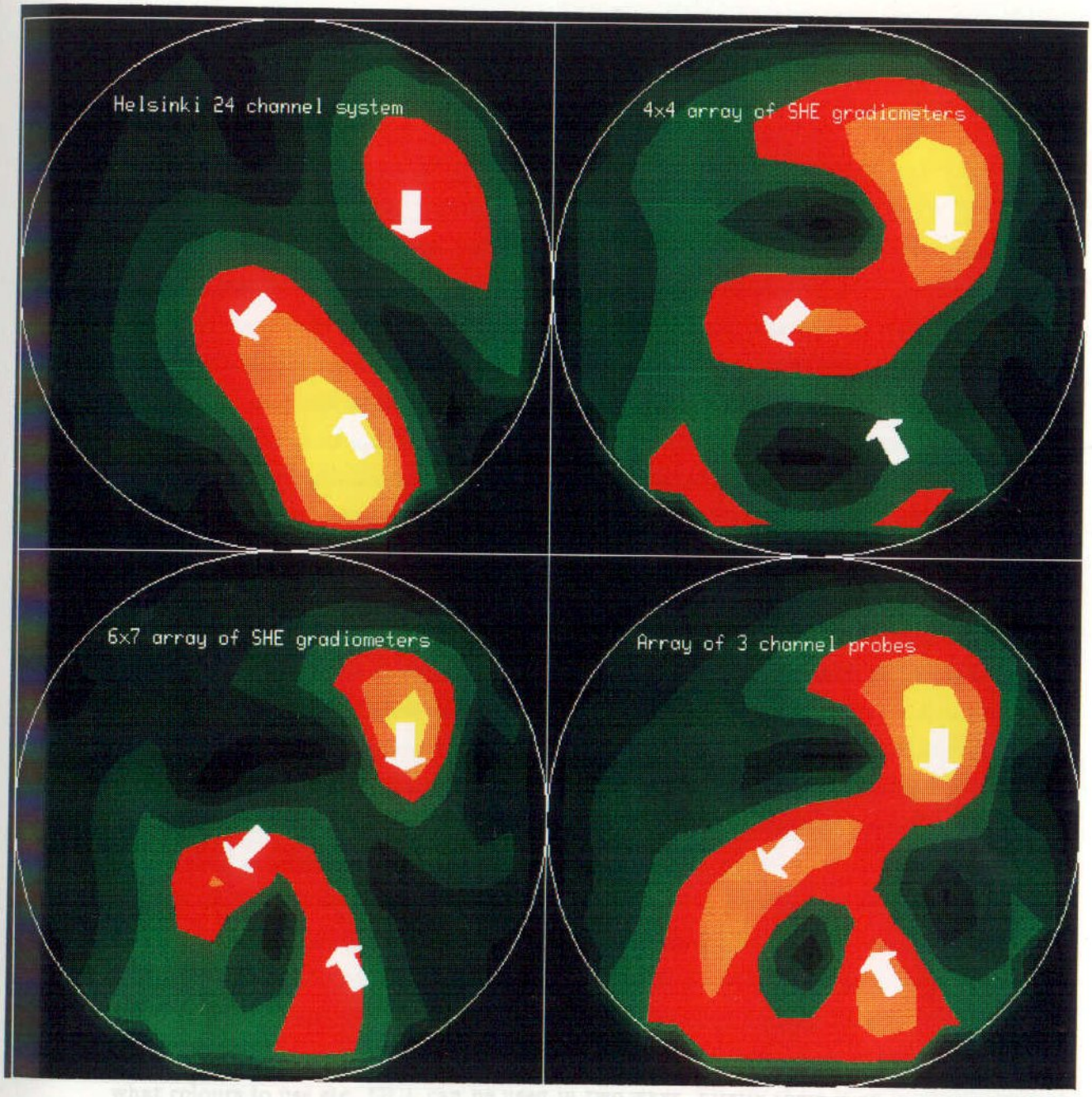

Figure 4.20 Contour maps showing the current density images obtained when all three dipoles are active.

Chapter 5

Software tools

In this chapter we describe four software tools i.e four large software systems which have been designed to allow easy manipulation of biomagnetic data.

In the early days of biomagnetism, when single channel instruments were the only systems available, the need for comprehensive software analysis tools was not as great as it is today. The magnetic signals recorded from, for example, an evoked response experiment, could be displayed as a simple scan on a computer screen or a pen-plotter. However, the development of multi-channel systems with many simultaneous measuring sites has meant that the amount of data generated by even a single experiment requires sophisticated analysis and presentation software if the maximum amount of information is to be extracted from the measurements.

The first software tool that we have developed, DataView, allows magnetic data to be viewed and manipulated by the user, immediately after the experiment. This allows the user to identify regions of interest in both the spatial and temporal domains, and to decide on what software filtering regimes (if any) are applicable. The software can be easily configured to work with any multichannel arrangement. The system will also produce interpolated contour maps and arrow maps (i.e. maps where the vector values of any signal values are represented as arrows) of the data.

The next software tool described in this thesis is a graphics environment known as GCL (Graphics Control Language). GCL has been developed to allow the user to produce contour maps, arrow maps and 3-dimensional surface maps of any regular grid of data. It can therefore be used to view both magnetic field data and current density solutions. The user can control all the 'style' parameters of the various plots, such as whether to plot axes, what colours to use etc. GCL can be used in two ways. Firstly there is an interactive mode which allows the user to construct the image using simple typed commands. The second interface allows other programs to 'drive' GCL using a control file. The expert system described below makes extensive use of GCL in this way.

The other two systems presented in this thesis both address the problem of presenting and summarizing the current density solutions to the inverse problem. To do this we use the concept of an *active region*. This is a small part of the entire current density space (for example the visual cortex) which has a relatively large and localised current density, active

at a particular time in the response. Hopefully, in the future we will be able to correlate these functionally active structures with physiological structures in the brain.

The first approach to active region location described in this thesis is an expert system, ABIS, which uses some pattern recognition ideas (applied to the *magnetic* field map) to identify the position and orientation of a limited number of current sources.

Within ABIS, each active region is represented by a current dipole. This means that we are assuming a highly localised region of activation; an assumption which may or may not be justified. In this thesis we do not address in detail the validity of the current dipole model. It is perhaps worth noting that the model has had some success in clinical applications [50], but problems arise in identifying exactly when a highly localised source is appropriate.

The advantage of the expert system is that is uses a conceptually simple idea to find this set of current dipoles. It does suffer from two disadvantages. Firstly it is rather sensitive to noise in the data, and secondly a new rule-base must be constructed for every gradiometer used (for some gradiometers with rotationally unstable responses this could be very difficult).

The second system, IMAGE, is used to look at the dynamic behavior of active regions by analysing the full distributed current solutions described in chapter 4. The method used to produce these solutions is computationally very intensive but does not appear to be particularly sensitive to the type of gradiometer used.

One problem with these current 'images' is the vast amount of data in the current density solutions. Here the concept of an active region can be thought of as 'summarizing' this large amount of information.

In just one experiment carried out using the Helsinki multichannel system, 300 current density images (representing the current density over the visual cortex every 2 ms, in response to a visual stimulus) must be analysed. The software we have developed (IMAGE) allows a detailed investigation of this data block, and we can attempt to identify a limited number of regions which are active at any one time.

We believe that such tools have now become indispensable in the analysis of brain function. They allow all relevant information to be extracted from the data and present the results in a clear and attractive way. They are all designed to have a 'user friendly interface' but retain a large amount of flexibility. These features are essential if biomagnetism is ever to become a routine diagnostic tool in a clinical environment.

Note that in appendix B.1 there is a full listing of all the commands available in each of these software tools.

5.1 DataView

DataView is a program that allows the user to inspect the gradiometer signal data immediately after they have been collected in the laboratory. The system can be configured to work with data from any multichannel system, but in this thesis we shall illustrate the abilities of the system with data collected by the Helsinki 24 channel system described in chapter 4.

The gradiometers in the Helsinki system are planar ones and are arranged in 12 pairs, with one gradiometer in the pair measuring $\partial B_z/\partial x$ and the other measuring $\partial B_z/\partial y$.

The experiments considered in this thesis consist of a set of visually evoked responses and data were collected every 2 ms for a total of 600 ms. Figure 5.1 shows a typical display from the program. Each channel of data is represented as a single scan, with the relative positions of the scans corresponding roughly to the gradiometer position on the dewar bottom. Note how the scans are arranged in 12 pairs, with the upper scan showing data from the y derivative gradiometer, and the lower one data from the x derivative gradiometer. The vertical bar on each scan represents 40 fT/cm in this experiment.

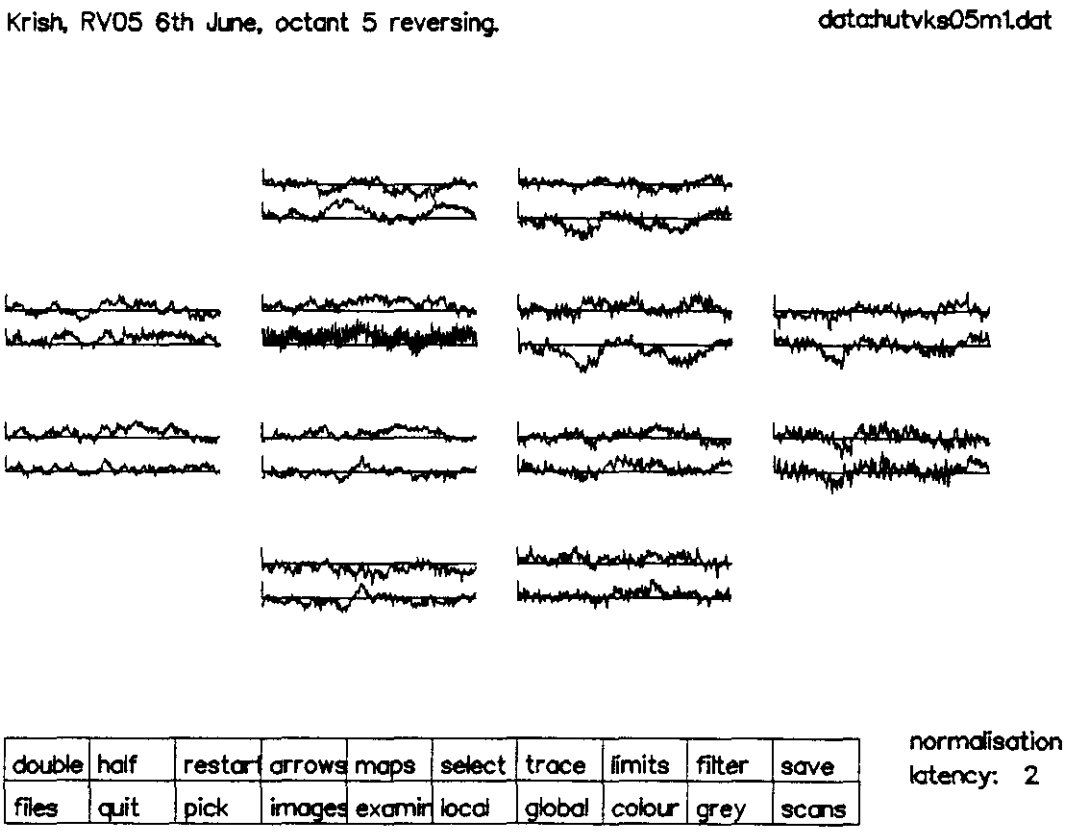

Figure 5.1 DataView: 24 channels displayed as scans.

The boxes at the bottom of the figure show the commands that are available to the user at this point. We have chosen a graphical user interface for this system so the user selects commands by moving a pointer using a mouse or graphics tablet. We have found this interface to be a very friendly and efficient way of guiding the user through the available

options. Some of the commands shown will execute directly when the user selects the relevant box, other commands result in a new set of options being displayed i.e there is a tree-like menu structure.

DataView is invoked by typing the following at the user prompt:-

```
DataView 'experiment'
```

Where 'experiment' is the name of a control file which defines the initial startup parameters for this experiment. For example, in one experiment carried out in Helsinki, three different stimuli were randomly presented to the subject (see chapter 6 for more details). Either the left visual field was stimulated, the right visual field or both together. In each experiment, roughly 100 presentations of each stimulus were used, generating 300 time series or *epochs*. These epochs were then sorted into three sets; m1,m2 and m3 according to which stimulus mode was used. Each set was then averaged to provide a single file for each stimulus. In this experiment, each average file consists of 300 measurements (i.e. 600ms of data sampled every 2ms), in each of 24 channels.

The control file tells DataView how many of these files there are in each experiment set, and what the specific filenames are. This concept of a set of files corresponding to one experiment also allows DataView to view unaveraged epochs i.e. the control file can be written so that it includes the filenames of the unaveraged epochs, allowing the user to select these for plotting.

The control file also instructs DataView on the *normalisation constants* to be used. These constants are used to scale the plots that DataView produces. The system uses two types of normalisation. In the local normalisation mode, when DataView produces a plot from a specific data file, DataView will scan through this file to find the maximum signal value and use this value to scale each plot. In the global mode, DataView will scan through the entire set of files (in our example the m1,m2 and m3 files) to find the maximum value, and this value is used to scale all plots. The user can switch between each mode at any time. Local normalisation is useful in emphasizing features in a particular plot, global normalisation is useful when direct comparison is needed between each file in the set.

To give an idea of the abilities of the system we shall now describe some of the more useful commands available to the user.

scans

Shows a dataset as a set of simple line scans. The scans are normalised using the global constant unless local normalisation is selected.

pick

The user can move a pointer using the mouse or graphics tablet to any part of any of the displayed scans. The program will print the channel number, the latency (timeslice number) and the signal value of the selected point.

images

Instead of a set of scans, the entire dataset is represented as a set of tiny colour intensity plots, with each pixel representing the signal strength of one channel. This representation allows the user to immediately see which timeslices are important and require further investigation. This command can only be used on colour graphics terminals. Figure 5.2 shows a colour printout of an 'images' display. Again, the data are a visual evoked response, measured using the Helsinki system.

Using the 'pick' option described above the user can identify the exact time of any of the images.

filter

A software filter is used to remove noise from the data. The filter used is a band-pass filter and the lower and upper frequency limits can be set by the user. The algorithm used is a fast fourier transform, followed by modification of the frequency domain signal and an inverse fast fourier transform. To prevent ringing effects, the 'edges' of the filter are not sharp but fall off linearly over a few Hz.

map

As the program knows the coordinates of each gradiometer, and the gradiometers are distributed in a rough plane (actually a shallow curved surface in the Helsinki system), the program can calculate an interpolated contour map.

These interpolated contour maps are useful in that they use the necessary continuity of the magnetic field (and its gradients) over the measurement grid to bring out detail and structure which might not be apparent in a simple viewing of the data scans.

DataView can display either colour shaded contour maps, or line contour maps. It will also show a plot of the $\vec{V_3}$ function [28]. The components of this function are defined (in x,y coordinates) by the following

$$\begin{aligned} V_{3x} &= \frac{\partial B_z}{\partial y} \\ V_{3y} &= -\frac{\partial B_z}{\partial x} \end{aligned} \tag{5.1}$$

This function can be considered as giving a rough approximation to the current density in a plane under the detectors. Figure 5.3 shows a colour shaded contour map produced by interpolating the gradiometer signals from the 24 channels of the Helsinki multichannel system. The data again are from a visual evoked response, and this image shows the response 180 milliseconds after the stimulus. The actual function that is plotted is the modulus of the magnetic field gradients.

Note how the menu options displayed at the bottom of the screen have changed to those appropriate for contour map manipulation.

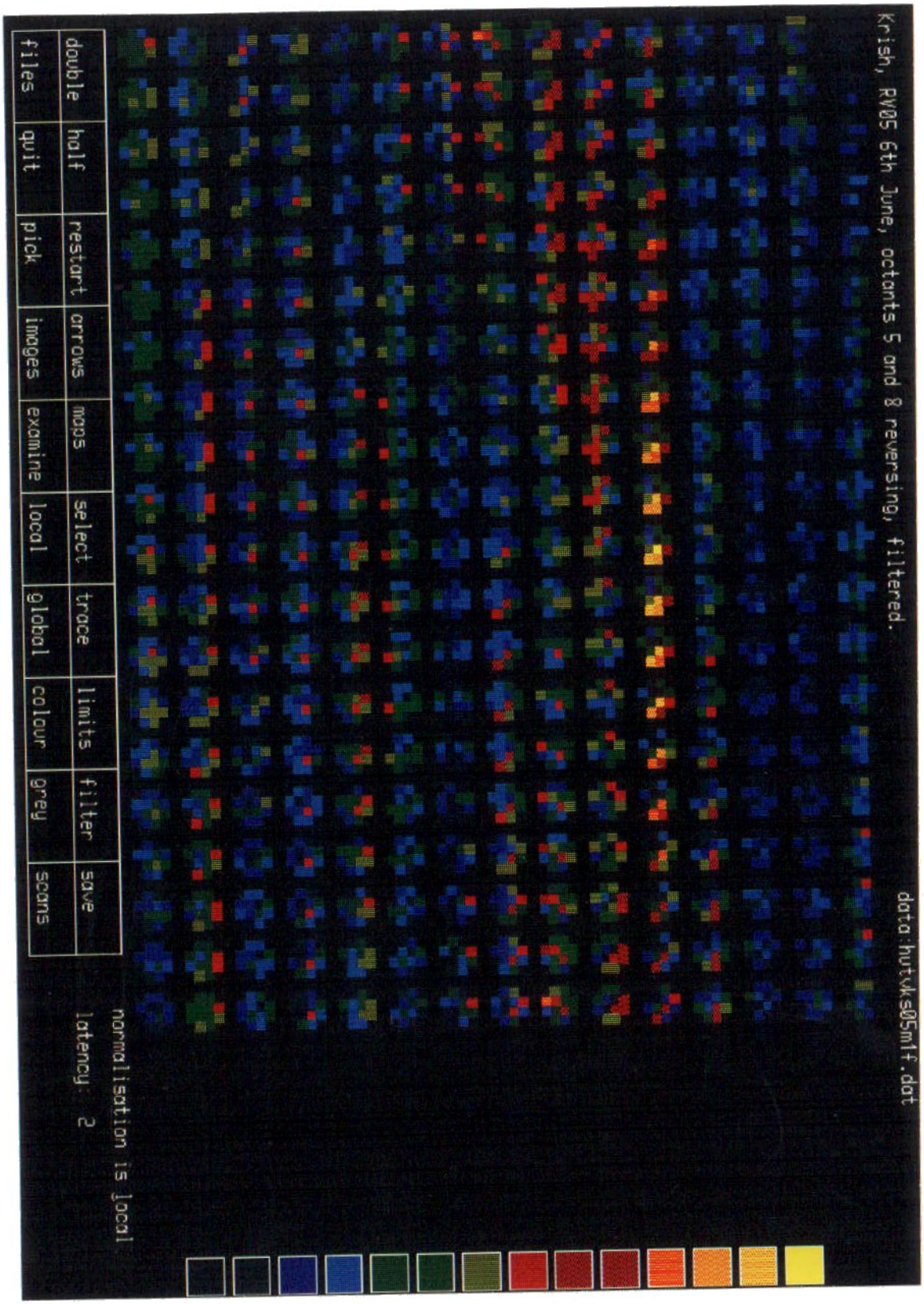

Figure 5.2 DataView: Montage of 300 tiny intensity images showing 300 timeslices for a visual evoked response.

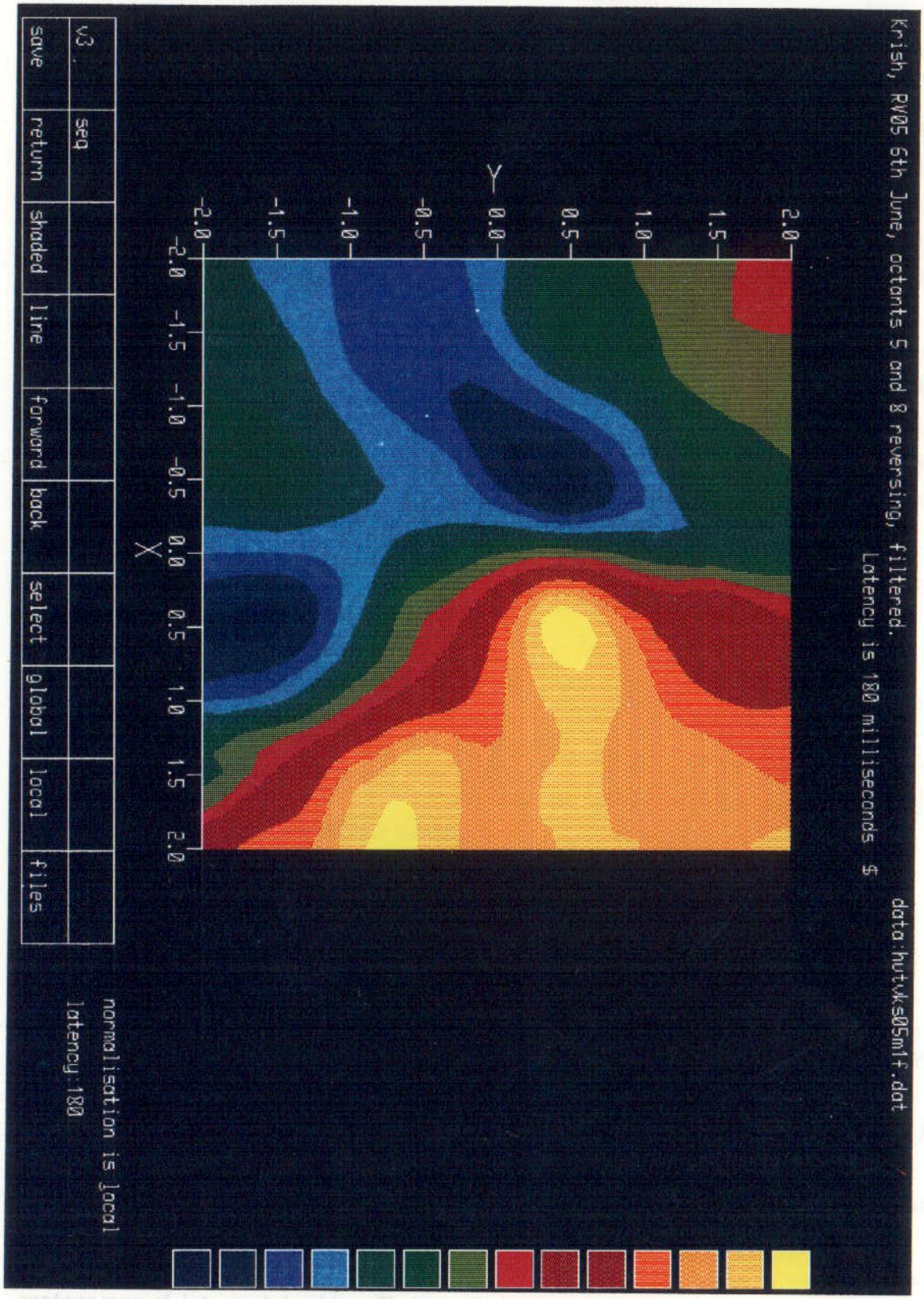

Figure 5.3 DataView: Colour shaded contour map.

5.2 GCL

GCL is a system for producing graphical representations of regular grids of data. GCL makes no assumptions about the origin of the data, only that they have been arranged in a regular grid. The data might therefore be a set of scans from a DC biomagnetic measurement, an interpolated grid of measurements from a multichannel system, or a current density solution. It is up to the user to make sure the data are in the correct form (and that this is a valid representation).

Up to now there have been two major applications for GCL. As it is a system which can be programmed in a special interpreted language, it is ideally suited to the production of large numbers of contour maps, and this was especially useful for a recent publication on dc measurements of chick embryos [8]. The other major application relies on the fact that GCL can be controlled by other programs and hence was used as the graphics environment for the ABIS rulebase (see below).

GCL can produce the following types of picture, given a regular grid of data:-

- line contour maps
- shaded contour maps
- colour coded intensity maps
- arrow maps of the v3 function
- superimposed mixtures of the above
- 3D line pictures
- 3D shaded pictures
- a set of line scans

It also lets the user control the style of the plot, for example which colour palette to use, whether to plot axes and titles etc.

Background images such as line drawings and frame 'grabbed' video images can also be used as backdrops for the data representations.

The finished images can be either displayed on a graphics terminal, or sent to a hard copy device. Images can also be saved in a file for inclusion in a LaTeX document.

The user interface for GCL is a simple command line interpreter. For example to draw a contour map of data contained in a file 'maps:bt16ss.map', the user would type the following at the GCL prompt

```
contour(bt16ss)
```

Note that GCL assumes the directory 'maps', and the file extension '.map'.

To construct a GCL program the user simply creates a text file which contains a list of valid GCL commands. Consider the following GCL program:-

```
set_device(laser)
set_limits(-1.25 3.45)
set_axes(off)
contour(bt10ss)
contour(bt11ss)
contour(bt12ss)
contour(bt13ss)
grad(bt14ss,gbt14ss)
arrow_map(gbt14ss)
end_execute
```

The first command sets the output device to be a hardcopy laser printer. The second command establishes global normalisation limits for all further plots (by default GCL calculates local normalisation limits for each picture it produces). The next command turns off the axes option. Four contour plots are then sent to the laser printer. The 'grad' command produces no output but calculates the two-dimensional gradient of the map 'bt14ss' and stores it in a two-dimensional regular map 'gbt14ss'. The program then draws an arrow representation of this map.

This ability to build up complex sequences of plots has been extremely useful. The main disadvantage of GCL is that it does require data in the form of a regular, orthogonal grid. Note that this does not mean that the data must be from planar measurements as (for example) ABIS produces data in a regular grid in the theta and phi coordinate system (i.e. around the surface of a sphere).

5.3 ABIS, An expert system for localisation of active regions

This software tool enables a limited number of localised current sources to be identified from the magnetic field data measured in some experiment. The basic tool is an expert system known as ABIS, which uses some simple pattern recognition ideas to find the active regions. The expert system is controlled by a rulebase which allows the user to specify the strategy to be used for the localisation in a high level, flexible way. In this section we shall illustrate the abilities of ABIS with a rulebase (SPHERE) designed to locate current sources in a homogenous conducting sphere, using data collected using the standard SHE gradiometer described earlier.

Like GCL, ABIS assumes that we have magnetic signals over a regular grid of data so some pre-processing of the data (i.e interpolation etc) might be needed. In the case of ABIS/SPHERE, the data are distributed over a spherical surface in a grid which is regularly spaced in the theta and phi coordinates.

Unlike the distributed current model used in chapter 4 to test gradiometer geometries, the method assumes that the current sources are a set of current dipoles right from the

beginning of the analysis. In a sense, no inverse problem calculation is performed by ABIS. Instead, we use the fact that the shape of the magnetic field generated by a current source can provide a useful indication of the position, orientation and strength of that current source. The first stage of the analysis, therefore, is to extract some basic features from the magnetic field data which somehow summarize the salient features in the data. In this section of the thesis we shall first illustrate the use of feature extraction by ABIS/SPHERE using a single current dipole as a simple example. We shall then show the extension of this type of analysis into the full expert system to locate multiple current sources.

5.3.1 Feature extraction

The approach used by ABIS is based on some simple pattern recognition ideas. Consider the simulated magnetic field pattern shown in figure 5.4 (produced by GCL). The signal was measured radially by the SHE gradiometer outside a conducting sphere of radius 11cm and was produced by a dipole whose position and orientation are given by

r/m	θ/rad	ϕ/rad	Q_r/Am	Q_θ/Am	Q_ϕ/Am
0.09	1.7	0.4	0.0	-7.1×10^{-9}	7.1×10^{-9}

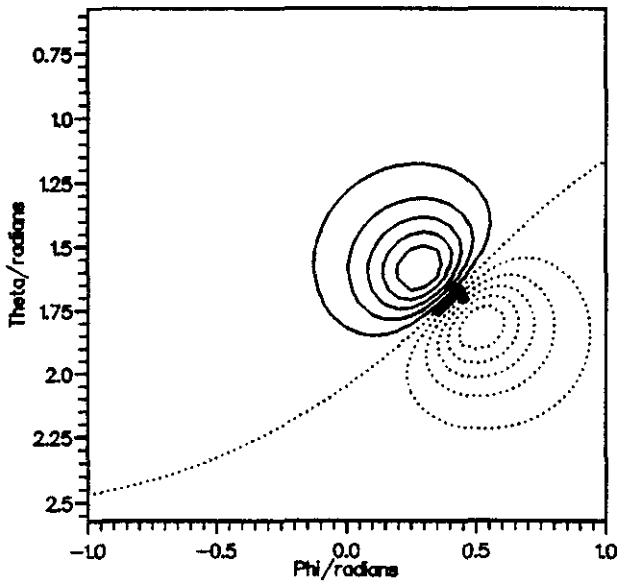

Figure 5.4 Dipolar signal pattern.

A human operator finds it very easy to locate the theta and phi coordinates of the dipole and the direction of current flow. If we look at the contour map, there are two peaks within the 'image', a positive one and a negative one. The dipole is positioned symmetrically between these two peaks, and is oriented along a line perpendicular to the line joining the two maxima. The depth coordinate is more problematical but can be calculated using a function which relates the depth to the distance between the two maxima in the image. In the case of a magnetometer this is a simple linear function, but in the case of a practical gradiometer, the function is more complex.

ABIS tries to emulate the human expertise described above by using a common pattern recognition technique which breaks the target image down into a set of primitive features [33]. In our case we choose three; edges, dots and weights

Edges

If we take the function $\nabla S(\theta, \phi)$ of the signal map, where $\nabla = (\frac{\partial}{\partial \theta}, -\frac{1}{\sin\theta}\frac{\partial}{\partial \phi})$ and $S(\theta, \phi)$ is the signal, we obtain the vector field $\vec{V_3}$ [28]. The modulus of this field is shown in figure 5.5. There is a local maximum of this vector function within the image at the same theta/phi position as the dipole and with the same direction as the dipole. We call this feature an *edge*. Note that we cannot say that every edge in a field map is a dipole, as there are in fact three edges in figure 5.5, shown as heavy arrows. In practice, we postulate that the strongest edge in each map is a dipole.

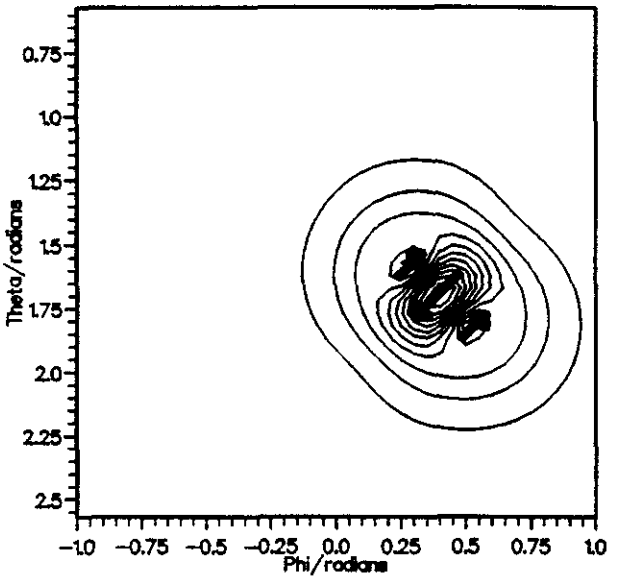

Figure 5.5 Modulus of the $\vec{V_3}$ vector gradient function, showing the three edges associated with a single dipole source.

Dots

To obtain the depth coordinate of the dipole we could simply use the distance between the positive and negative signal extrema. There is a relationship between these two parameters which is defined by the particular gradiometer in use. However, the identification of the signal extrema in the presence of noise could be rather inaccurate and so we use the concept of a *region*.

The first step in delineating a region is to construct the *convexity* of the signal map, $-\nabla^2 GS(\theta, \phi)$, where ∇^2 is the standard Laplacian in polar coordinates and G is a Gaussian weighting function. This operator has the effect of spatially 'tightening' the contour map and the result is shown in figure 5.6. Note that associated with the dipole are a positive and a negative region which the algorithm identifies by starting from the convexity maximum

and travelling outwards until it reaches some preset threshold value. The region boundaries are shown as heavy lines in figure 5.6. The position of each dot, r_d, is defined to be the center of gravity of each region i.e $r_d = (\overline{x}, \overline{y})$ where

$$\begin{aligned} \overline{x} &= \frac{1}{M}\int\int xC(x,y)dxdy \\ \overline{y} &= \frac{1}{M}\int\int yC(x,y)dxdy \\ M &= \int\int C(x,y)dxdy \end{aligned} \tag{5.2}$$

Where C is the value of the convexity function. The integrals in the above equations range over the whole of the dot region (i.e within the heavy lines in figure 5.6).

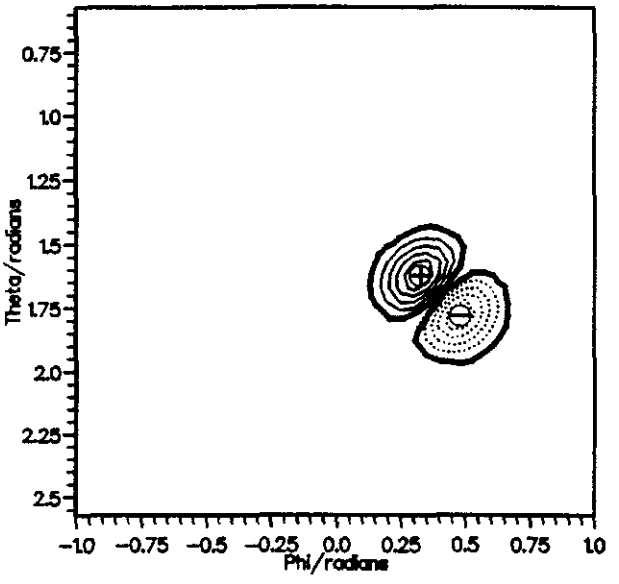

Figure 5.6 Convexity function, with delineated dot regions.

Weights

Within any one contour map, associated with several dipoles there will be several edges and dots. The dipole location process must identify which dots are associated with which edges. For each edge-dot pair we define a weight function, which consists of three items of information. Firstly, there is the distance in radians between the two items, secondly there is the *relevance* parameter, and finally there is the *contribution* parameter. The relevance parameter is defined by the angle between the edge direction and the line joining the edge to the dot ($\theta_{edge-dot}$) , by the simple expression

$$relevance = sin(\theta_{edge-dot}) \tag{5.3}$$

If there is zero angle, then the edge and dot under consideration cannot be generated from the same dipole. If the angle is 90 degrees then the relevance parameter is deemed to be 1.0.

The contribution parameter gives the proportion of signal within each dot region which could be generated by a dipole positioned under the relevant edge. This parameter is needed

as two dipoles could contribute to the same dot region. If there are n edges in the map, then the contribution from the jth edge to this dot is given by

$$C_j = \frac{1}{\sum_{i=1}^{n} \frac{R_i}{D_i}} \frac{R_j}{D_j} \tag{5.4}$$

where the D parameters in the above equation are the distance components of the weight function for this dot, and the Rs are the relevance parameters. The contribution parameter is defined in the above way so that the sum of all contributions to a particular dot is always 1.

ABIS/SPHERE can be used to provide a feature based description of figure 5.4. The strongest edge was found to have the following parameters

Edge	θ/rad	ϕ/rad	D_θ	D_ϕ
1	1.7	0.4	-0.70	0.71

It is clear that the angular position of the dipole is found correctly. $\vec{D}$ is the unit orientation vector for the edge, and is the same as the original dipole (to within 1.4 percent).

The two strongest dots were found to be

Dot	θ/rad	ϕ/rad	Strength
2	1.63	0.33	1.0
3	1.77	0.47	-1.0

and the associated weights were

Edge,Dot	Sepn/rad	Relevance	Contribution
1,2	0.097	1.0	1.0
1,3	0.097	1.0	1.0

The dots are symmetrically placed either side of the edge, are equally relevant to that edge, and receive 100 percent of their strength from that edge. To obtain the dipole depth we use a lookup table which relates the depth of the dipole to the edge-dot separation. For a 11 cm radius sphere and the SHE gradiometer the table is as follows (R is the radial distance from the sphere origin to the dipole, expressed as a fraction of the sphere radius).

R	Edge-Dot Sepn, Δ/rad	Gradient, $\frac{dR}{d\Delta}$
0.909	0.094	-91.0
0.818	0.095	-5.2
0.727	0.112	-3.138
0.636	0.141	-2.844
0.545	0.173	-2.162
0.455	0.215	-1.753
0.364	0.267	-1.444
0.273	0.330	-0.989
0.182	0.420	-1.011

The most striking aspect of this table is that it is in fact highly non-linear, especially when the dipole is close to the detector. The reason for this is that the axial gradiometer exhibits mixed modes of behavior. When the source is far from the gradiometer, we are measuring an approximation to the second derivative of the field. When the source is very near to the bottom coil, the signal is an approximation to the field. To compensate for this non-linearity, we store the gradient, $\frac{dR}{d\Delta}$, at each point in the table and use linear interpolation around the fixed points. Having established the depth, the program can then calculate the dipole moment of the source.

Using this lookup table, the inverted dipole parameters were found to be

r/m	θ/rad	ϕ/rad	Q_r/Am	Q_θ/Am	Q_ϕ/Am
0.0904	1.7	0.4	0.0	-6.5×10^{-9}	6.6×10^{-9}

For convenience the previously listed, correct dipole parameters are repeated below.

r/m	θ/rad	ϕ/rad	Q_r/Am	Q_θ/Am	Q_ϕ/Am
0.09	1.7	0.4	0.0	-7.1×10^{-9}	7.1×10^{-9}

As expected, the algorithm finds the angular position exactly and the depth is accurate to better than 1 percent. However the magnitude of the dipole source is only 93 percent of the true value. This inaccuracy comes about because the magnitude of the source is very strongly dependent on the depth parameter. The system has actually placed the dipole slightly nearer to the detector than it should be, and has compensated by reducing the signal magnitude.

The link between depth and magnitude always causes problems in dipole inversions, but we believe an improvement in the depth lookup table (more points, or a full polynomial fit), would reduce these problems.

In summary, feature extraction provides a computationally very quick method of identifying the position of a dipole. To extend this approach into multiple-dipole inversions we used an Expert System approach.

5.3.2 Expert system approach to Multiple Dipole Location

In this method, an expert system is used to analyse the features extracted from a signal map, in order to locate a set of dipoles. The advantage of an expert system is that it allows the designer to specify how the dipoles should be located by specifying a set of high-level rules contained in a rule-base.

The expert system we use, ABIS, was developed by Palfreyman et al [31], and is coded in Prolog, a *declarative* language. Most programming languages such as Fortran and Pascal are *procedural* i.e. the programmer specifies exactly the sequence of operations that the computer must go through to achieve a certain function. In a declarative language, the programmer specifies exactly the logical relationship between the input variables and the required output variables, and the language system chooses the algorithm for evaluation

of that result i.e the function becomes a 'black-box' to the programmer. A language like PROLOG forces the programmer into defining these logical relationships in a very formal, structured way.

In a pattern recognition system, we could imagine making a set of declarative statements relating the features in an image to the initial generating objects, and then allowing the expert system to find these objects. In the biomagnetic inverse problem however there is a difficulty in that two adjacent objects (e.g two current dipoles) will distort each other's magnetic field (in the extreme case, cancelling each other out completely). This problem is known as context sensitivity and can only be solved by injecting a procedural aspect into the inversion.

ABIS first identifies the primary source (using feature extraction) and subtracts the signal this source produces from the signal map. This leaves a new signal map which can then be analysed in the same way. The procedure continues until either the signal values within the map are below some threshold or a specified number of sources have been identified. Having identified this initial set of dipoles, ABIS refines its estimates. If, for example, there were 3 dipoles, ABIS would take the original signal map and subtract the simulated signal generated by dipoles 2 and 3. This should leave a map within which the only current source is dipole 1. ABIS can adjust the dipole parameters for dipole 1 to provide the best fit to this map. The procedure is then repeated for dipole 2 (i.e 1 and 3 are kept fixed), and finally for dipole 3.

Of course, the whole procedure outlined above could be coded in Fortran, but we have chosen to link the procedural code needed to identify and refine the dipole positions and locations into a declarative rulebase which controls the system. This allows us to specify the approach to be used in modular, high level rules. One particular rulebase that we have developed is the SPHERE rulebase which instructs ABIS on how to find dipoles within a conducting sphere geometry, given signals measured by the SHE gradiometer.

Consider the following three dipoles, again contained in a conducting sphere of radius 11 cm.

r/m	θ/rad	ϕ/rad	Q_r/Am	Q_θ/Am	Q_ϕ/Am
0.090	1.7	0.4	0.0	-7.1×10^{-9}	7.1×10^{-9}
0.080	1.5	-0.25	0.0	-5.0×10^{-9}	0.0
0.076	2.0	-0.75	0.0	1.0×10^{-9}	6.9×10^{-9}

Figure 5.7 shows the simulated signal contour map produced by these dipoles (note we are assuming that no noise is present). It is dominated by the strong superficial source on the top right.

ABIS/SPHERE was instructed to find all the dipoles in this map (without any operator intervention) by using the following command

```
solution1 underlies problem-map
```

This is a PROLOG-like command which relates an input variable (in this case a signal map called problem-map) to an output variable (a set of current dipoles called solution1).

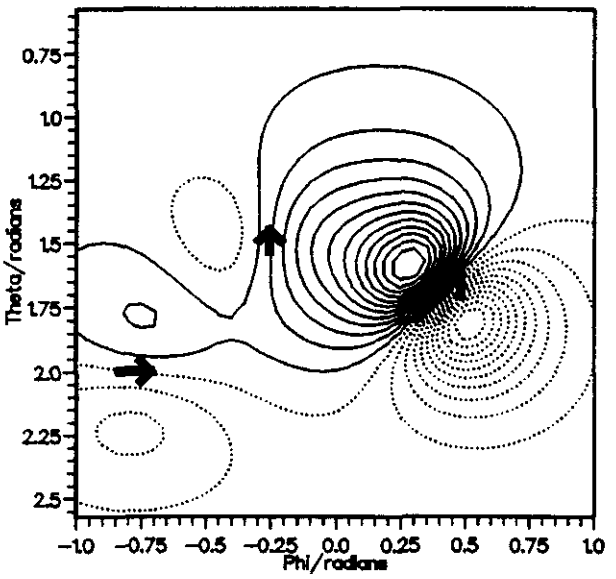

Figure 5.7 Signal map produced by three test dipoles.

The logical operator 'underlies' which links the two arguments is known as a predicate and is defined within the rulebase. As described above the predicates defined in ABIS/SPHERE are a mixture of procedural code and declarative statements.

When the above command is submitted to ABIS/SPHERE, the PROLOG environment attempts to solve the logical relationship, and thus produces the following set of dipoles

r/m	θ/rad	ϕ/rad	Q_r/Am	Q_θ/Am	Q_ϕ/Am
0.091	1.70	0.40	0.0	-6.2×10^{-9}	6.2×10^{-9}
0.083	1.50	-0.25	0.0	-3.3×10^{-9}	0.2×10^{-9}
0.078	2.00	-0.76	0.0	0.6×10^{-9}	4.8×10^{-9}
0.073	1.64	0.44	0.0	2.5×10^{-9}	-2.1×10^{-9}

Again, the angular positions and orientations of the three dipoles are found rather well, but there is some inaccuracy in the depth and magnitude values. Note also how the inversion has postulated a deep, weak dipole to 'mop up' some of the signal residue. The interesting thing about this spurious source is that it is at roughly the same angular position as the strongest dipole (which ABIS/SPHERE postulated as being weaker than its true value). It may well be that with a more accurate depth/magnitude calculation this phantom source might not be considered necessary by ABIS/SPHERE and would not appear. However, this is a common problem in ABIS i.e it can have trouble deciding where to stop in the inversion procedure. We have included commands in ABIS which look for a specified number of dipoles, rather than allowing the expert system to estimate how many sources are active. This option must be used with some care, as telling ABIS that there are an inappropriate number of dipoles may lead it to make false estimates for the sources that it does find.

In a recent paper [32], results of a blind test of ABIS were presented. Ten different three dipole configurations were presented to ABIS and in all cases it was able to find the radial position of each dipole to better than 5mm, and the angular positions to better than 0.03

radians. The test configurations were not completely random in that the person defining the set did not place dipoles too close to the edge of the map. Despite this qualification however, it is still a rather impressive performance.

5.3.3 Limitations

ABIS provides a very fast and accurate system for locating a few dipolar sources given a signal map. Apart from the problems with depth/magnitude and creation of spurious sources, the major problem with ABIS is that is sensitive to noise in the signal map. This leads to difficulties. Firstly, if there is a lot of noise with a high spatial frequency within the map, ABIS will find it difficult to know where to stop in the inversion process. It may continue to fit spurious sources, even after it has identified the true solution. Fortunately, there is a strategy for dealing with this specific noise problem (although it has not been implemented yet within ABIS), which uses the fact that the spatial frequency content of a dipole map is dependent on the depth of the dipole i.e the deeper a dipole is the 'smoother' the pattern. It follows from this that there is a maximum spatial frequency which can be present in the signal map, and this corresponds to the most superficial dipole that we can postulate. This means we can spatially filter the signal map above this cutoff.

The second noise problem occurs if there are (for example) very deep dipoles which generate a low spatial frequency noise in the image. These dipoles cannot be identified by ABIS, as the full contour pattern may not appear within the image, but their effect is to distort the patterns produced by the more superficial dipoles, making their identification difficult. Again, spatial filtering is one solution, but the exact filtering regime is not as easy to define in this case.

Another disadvantage of ABIS is that, for each gradiometer design, a completely new rulebase must be created. This is especially problematic for planar geometries which in almost all cases produce maps in which the features are not stable to rotation of the source. A much more complicated rulebase must then be constructed which can deal with all possible angular orientations of the source. As the main advantage of ABIS is its fast and simple identification of active regions, it is therefore doubtful whether it is particularly useful for non-axial geometries.

As we hope that biomagnetism will eventually become a routine clinical tool, the user interface of any software tool is of paramount importance. At the moment ABIS retains a command-line interpreter, which accepts the PROLOG like predicates which control the dipole location process. This is a very efficient and flexible way of interacting with ABIS, but is rather unhelpful for the inexperienced user. A better interface for such users is a menu-based one, which guides them through the available options in a sensible way. The addition of such an interface to ABIS has not been implemented yet, but would be an essential first step in extending the usefulness of this tool.

5.4 IMAGE

IMAGE was developed with a specific task in mind, namely the presentation and summary of the large amount of information contained in the full distributed current solutions described in chapter 4.

One advantage of the current dipole method of inversion is that the dipole provides a very neat way of summarising the current activity. The dipole can be thought of as representing the centre of gravity of the active region, and can be expressed as a set of six numeric parameters, or as a simple arrow on a contour map. The problem is that the simplicity of representation that makes the dipole so attractive also means that the model is only really applicable in a limited number of cases (although until recently it was the only model used). If there is only a single region of superficial activity, then it is reasonable to use a current dipole as the representation. As we described in chapter 4 we have developed a more general inverse problem algorithm which can solve for the current density, even if it is distributed in a complicated, non-localised way.

The problem with these distributed solutions is that they contain a large amount of information that must be presented in a way that makes the salient features easily apparent. The problem is compounded by the fact that the major application we are interested in is the time evolution of activity in the brain. With MEG (MagnetoEncephalography) it is possible to achieve time resolutions as small as 1 millisecond. Of course, this means that we may have a current density solution every millisecond , for several hundred milliseconds. So, as well as presenting the distribution of current in some meaningful way, we somehow have to show how the activity develops in time.

When the distributed current method was first developed, the solutions were saved as video images. When the video was played back, the viewer could see how the activity varied in time. The problem with this type of presentation is that it can only provide a qualitative 'feel' of the dynamics of the activity. Also, video cannot be used for publication.

IMAGE was designed to replace the video technique by extracting the dynamic information from a series of current density solutions and present it on a single static image. It also allows the user to segment the current density images into a set of active regions (of any size), and follow the activity within these regions. These localised regions replace the current dipole model in summarizing the activity.

In a typical analysis of an evoked response, the current density solution will be represented as a 'map' over a 2-dimensional disk. One of these disks will be produced for every timeslice in the response. For example in the Helsinki visual evoked responses presented in chapter 6, data were taken every 2ms over a 600 ms period. So for this particular experiment there are 300 current density solution disks, or timeslices. These slices are can be considered to be stacked in a cylinder of data, with the axis of the cylinder representing time.

IMAGE allows the user to view any timeslice from this cylinder in a variety of representations. Secondly, it can identify active regions within the data cylinder, and then it can plot the activity in these regions as a function of time.

We shall now present some of the most useful features of IMAGE in order to give a brief overview of its capabilities. By way of example, figure 5.8 shows a typical colour image generated by the system.

Timeslice representation

The types of timeslice representation that can be produced are

- colour shaded contour maps of either the current density or of the dot product with an arbitrary unit vector (this allows any of the components of the field to be examined).
- line contour maps of the above.
- colour shaded arrow maps which show the magnitude and xy direction of the current density.

5 separate images can be simultaneously displayed in 5 different windows on the screen. Each of these windows has its own set of parameters such as normalisation constants and data filenames. The physical size of the window on the screen can be modified by the user.

In the top left of figure 5.8 there is a colour shaded contour map, representing the modulus of the current density in a disk roughly at the level of the visual cortex. This particular timeslice corresponds to 100 ms after a visual stimulus was presented in the left visual field of the subject. We can see from the contour map that there are is a primary region of activity on the right side of the cortex, with perhaps a second smaller region to the lower left.

Region identification and activation curves

IMAGE has a set of commands specifically designed to identify regions within the data cylinder which are active at particular latencies. The first of these 'plot peaks', asks the user for a start and end latency. It will then plot a colour shaded dot, for each timeslice in this range, at the point in the disk where the modulus of the current density is a maximum. This option often shows dots clustering for a few timeslices in a particular location, before moving onto a new locale. A second command 'plot snake', will join the dots with arrows indicating the direction of movement. This option is useful for showing any loop like structures. Examples of the use of these commands can be seen in chapter 6.

When the user has identified a timeslice which is likely to have an active region, a colour shaded contour map (or any other representation) can be drawn for that timeslice. The next stage is to draw what is known as an *activation curve* for that region. The user first defines the extent of the active region, within the currently defined timeslice. On figure 5.8, a rectangle can be seen superimposed on the contour map. This limits of this rectangle were defined by the user using a mouse pointer. In the figure two regions have been selected, the first from the left contour plot which shows the 100 millisecond response, the second from the right hand contour plot which shows the 300 millisecond response.

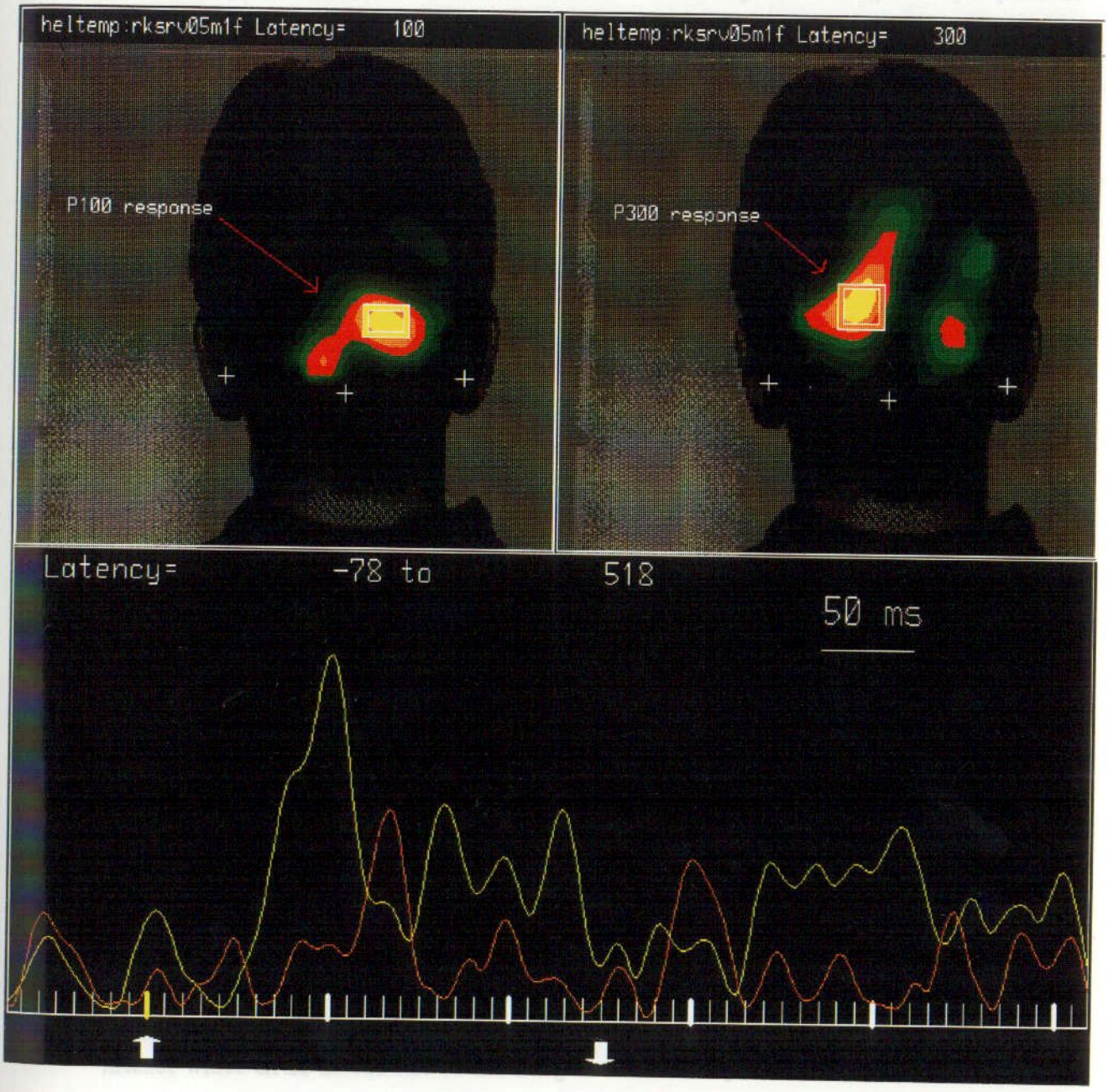

Figure 5.8 IMAGE: Two activation curves.

Underneath these plots, IMAGE has plotted two curves which represent the average current density within each of the two regions, plotted over a selected time range. The curves show the user exactly how the activity within a localised region varies over time. Similar plots have been produced in the past for single/multiple current dipole models [59], but this approach to dynamic localisation has the advantage of limiting the assumption of a localised region to the very end of the analysis procedure.

The plots show some interesting features, including a possible anti-phase relationship between the two regions.

This form of analysis has proved to be uniquely powerful, and we feel it combines in a reasonable way the full distributed current analysis approach to the inverse problem, and the necessary 'summarizing' tool we call an active region.

Annotation

One of the main uses for IMAGE is to produce high quality images for publication and presentation. With this in mind, we have included many commands for annotating the data images. These include

- text
- user specified lines (such as the red arrows on figure 5.8).
- any line drawing.
- circles.
- rectangles.
- background raster images.
- automatic inclusion of experimental details

Potentially the most useful form of annotation is the use of MRI (Magnetic Resonance Imaging, [63]) to provide anatomical correlates for the current density solutions. Figure 5.9 shows an MR image of a subject, which has been loaded into one of IMAGEs graphics windows. This particular image is a sagittal slice through the middle of the head. The intense white circle at the left of the image is a vitamin pill marker, which was taped to the subject's inion to provide a reference point. At the moment we have not linked the MR coordinates to the current density solutions, but in the near future we expect to superimpose the current density representations directly onto a relevant MR representation.

To prevent the image becoming too cluttered, we would pre-process the MR image to extract the basic physiological details from it. Figure 5.10 shows a simplified representation of the full image, where the user has traced round the important structures, such as the cortex and cerebellum, using different colours. This can be carried out using the line drawing function from within IMAGE.

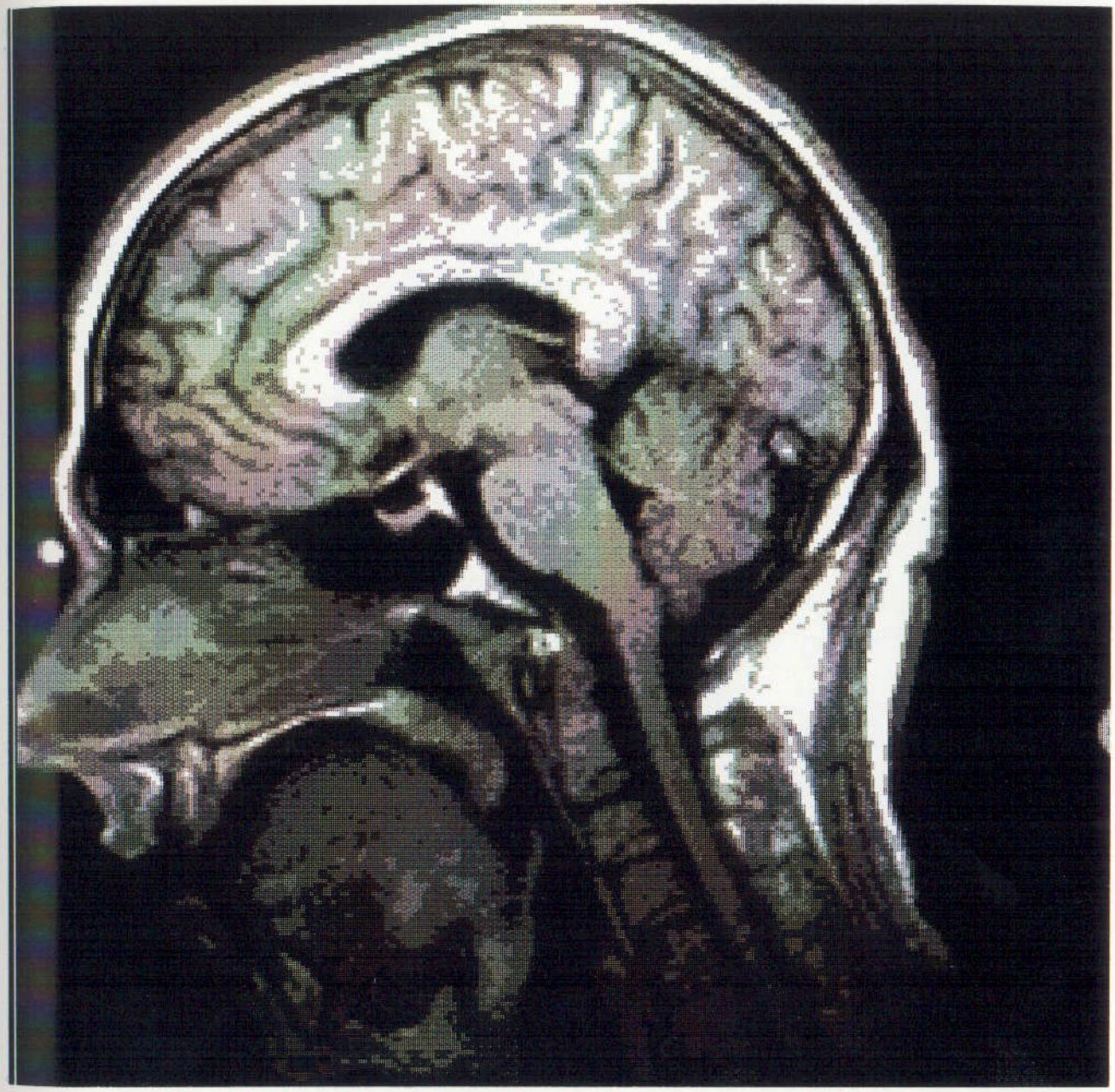

Figure 5.9 IMAGE: MR image.

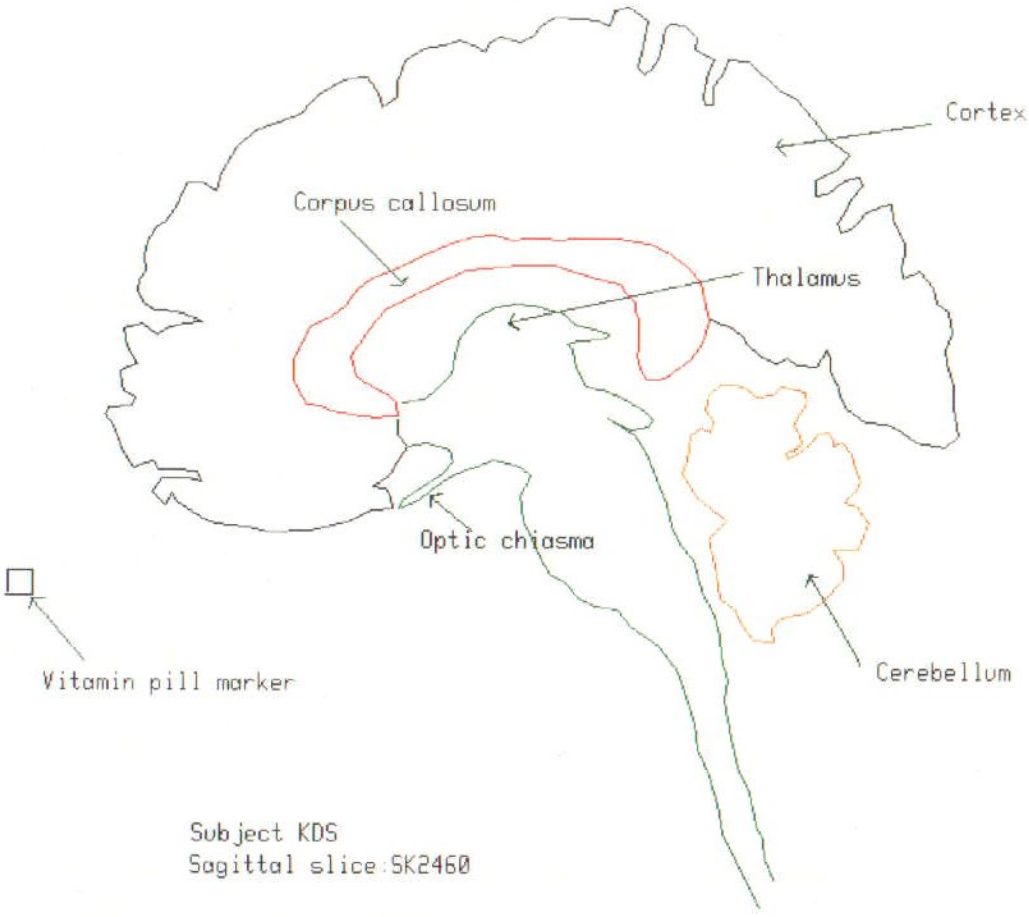

Figure 5.10 IMAGE: Summarised MR image.

The user interface and programmability

Like DataView, IMAGE has an interactive interface which uses a tree-like menu structure, together with a mouse or graphics tablet to select commands. The interface is much more sophisticated however, in that, as the user interactively builds up a complex image, the program is converting each selected command into a special interpreted language, IIL. These IIL commands are stored in a file and can be used to recreate the image at a later date.

When IMAGE is first run, it asks the user for the name of an image file containing a set of IIL commands. These commands set the style for the whole image the user is to create and contain details such as the data filename. As the user selects new commands using the menu system the new IIL commands are appended to the original ones.

In fact, the user does not have to work with IMAGE interactively at all, but can write the entire image specification as a set of IIL commands. By way of example consider the following example of an IIL program (which could have been written directly as a text file by the user, or constructed by IMAGE in response to interactive commands by the user).

```
vuda 0.0 0.0 1.0 1.0
stim 80
step 2
root 1 data:helsinki
root 2 data:helsinki
arro 1 100
arro 2 300
exit
```

The first command establishes the position and size of each contour map, within each of the five physical graphics windows. The next two commands tell IMAGE that the stimulus occurs at 80 milliseconds and data are presented every 2 milliseconds. The 'root' commands tell IMAGE which data file to use for each of the five windows. The first 'arro' command tells IMAGE to draw a colour shaded arrow map, representing the current density 100 milliseconds after stimulus, in window 1. The second command displays the arrow map for a latency of 300 ms, in window 2. The exit command then leaves IMAGE. If 'exit' was not present, then IMAGE would go into its interactive mode and allow the user to modify or extend the current image.

A full listing of the IIL commands can be found in the appendix of this thesis.

Hardcopy

IMAGE supports three hardcopy devices

- Colour printer
- Laser printer

- Latex file

When the user selects one of the above options, IMAGE takes the IIL commands defining the current image and submits a batch job, essentially re-running itself. This method of implementing hardcopy means that the operation takes place in the 'background' i.e. the user does not have to wait for the hardcopy operation to finish before continuing. Also an unlimited number of hardcopies can be generated one after the other (to different devices if required).

IMAGE automatically adjusts the image to take account of the limitations of the hardcopy device. For example, all colour shaded commands will be converted to line contour plots and monochrome arrow maps when the laser printer or Latex file devices are selected.

Future development

IMAGE is constantly being upgraded on a day to day basis with minor modifications such as extending the annotation options etc. The first major upgrade that is planned will allow the user to inspect full three dimensional current density images, rather than the 2-dimensional disks used at present. The use of other imaging modalities such as MRI to provide automatic correlation of our functional images with anatomy will also be included in the system.

Another extension that is being planned is to make IMAGE more intelligent. At the moment the process of region identification is carried out by the user, however algorithms have been developed which provide some automatic detection of where and when a region is active within the data cylinder (see chapter 6).

Chapter 6

A visual evoked experiment using the Helsinki 24 channel system

6.1 Aims of the experiment

This chapter reports the results of an experiment carried out using the 24 channel system at the Helsinki University of Technology. This multichannel system uses planar gradiometers; the design and organisation of the channels has already been described in chapter 4. Visually evoked responses were provided by computer generated checkerboard patterns. The aims of the experiment were:-

- to investigate the retinotopic organisation of the cortex, by stimulating different parts of the visual field.
- to add to the experience already gained here at the Open University in using the distributed current model to analyse data from conventional axial gradiometers.
- to develop some new methods of post-inversion localisation of functional areas.

In the first section we describe the basic operation of the human visual system in terms of the connection pathway between the retina and the visual cortex. We then introduce the concept of the Visual Evoked Response (VER) and discuss its usefulness in both clinical and research applications.

In the next section the details of the experiment are described. In this thesis we present data from two different stimulus modes (a left visual field stimulus, and a right visual field stimulus), for a single subject.

In the final section we discuss first the data and then our analysis approach, by which we seek to identify separate activated areas within the cortex (for each stimulus mode). We then look how this activity varies as a function of time. We conclude that the two different stimuli are indeed mapped onto different parts of the visual cortex, but that the time activation of these two regions is remarkably similar. We are also able to show that the response when both areas of the visual field are stimulated is very similar to a linear sum of the responses to the two individual stimuli.

6.2 The visual system

The initial processing of a visual stimulus begins in the cells of the retina, where inhibitory and stimulatory connections between neurons allow functions such as edge detection to be carried out [42].

After these functions have been performed, the visual information is carried as a set of action potentials down the optic nerve. The visual pathway is summarized in figure 6.1. The evidence for these pathways come from microscopic analysis of the neuronal populations, such as dye injection, and radioactive tracing [42].

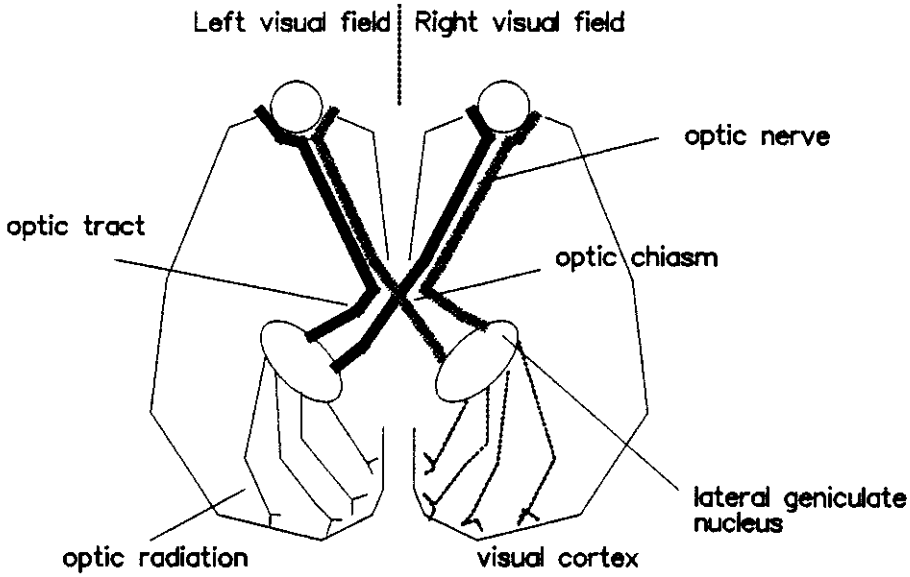

Figure 6.1 Visual pathways in the human brain, viewed from above.

At the optic chiasm, the optic nerves from each eye meet, and here signals from each side of the visual field are separated into two different optic tracts. Most neuronal fibres in each tract travel to a lateral geniculate nucleus, which performs some processing of the image. Geniculate nerve fibres then radiate out to the visual cortex, and terminate close to the central or *calcarine* fissure.

By stimulating different sides of the visual field we should be able to see localisation of the activity as it arrives at the cortex, with a left stimulus being represented to the right of the calcarine fissure, and vice versa.

One problem that we must be aware of, is that the cortex around the area we are interested in consists of a complex, folded structure. As activity moves around these folds it is possible that the source may appear and then disappear as it becomes magnetically silent to our detector geometry.

6.3 The visual evoked response

Using evoked responses, we seek to increase our understanding of brain function by studying how the brain responds to some external stimulus. The first such studies were carried

out using the measurement of the electric field at several places on the scalp (ElectroEncephaloGraphy). The general idea of evoked response measurement is readily transferable to magnetic studies and this is termed MEG (MagnetoEncephalography).

In an evoked response study some well characterized stimulus is repeatedly presented to a subject. In the so called transient evoked response, the repetition rate is not fixed, and enough time is left between stimuli for the subject's response to have ended before the next presentation. The EEG or MEG is measured for a fixed length of time (known as an *epoch*) after each presentation. Each epoch will contain information which correlates with the stimulus, and uncorrelated information (noise). By averaging many epochs the correlated signal is emphasized, while the noise is reduced [57].

In the steady state evoked response, the stimulus is presented at regular short intervals, with a view to setting up some kind of 'standing wave' activity within the brain. The analysis usually consists of a frequency analysis of the response. Nunez and co-workers have suggested that the brain has certain 'natural modes' of oscillation, and that the response to an oscillating stimulus is a resonance between the frequency of excitation, and these normal modes. Their argument for this theory is based on observations of the connection distances between neurons in the cortex, and the gross size and morphology of the brain (Chapters 10 and 11 in [43]).

They also suggest that the transient evoked response can be modelled as a Fourier synthesis of these 'normal modes' of brain activity. If this is true the frequency content of a transient response, and hence the way the response varies in time should be independent of the particular part of the cortex which is stimulated. Our results in this chapter give some support to this theory.

In this chapter we shall be concerned with the time variation of the spatial distribution of the activity produced by a transient VER. The stimulus we use is a reversing checkerboard octant. Checkerboards are used because they have been found to give good responses within the cortex [60] at around 100 ms after the reversal (the so called P100 response). This strong response probably arises because checkerboards contain very strong edges (i.e. lines separating regions of high contrast), and many neuronal populations within the retina and brain are connected in such a way as to be sensitive to such edges (chapter 2 in [42]). The reversal of the pattern is a stimulus mode which is easy to control and characterize. One major advantage is that the overall brightness of the image can be kept constant during the reversal, so eliminating any effects that a gross brightness change might produce.

In the experiment we performed, we were attempting to investigate what is known as the retinotopic mapping of signals. It is known from animal experiments that each part of the visual field is mapped onto a specific area of the visual cortex. We have chosen to use octant fields of view as a compromise between stimulating a small area to gain an accurate retinotopic map, and stimulating a large area of the visual field to elicit a large, measurable signal.

The investigation of this retinotopic mapping is something which EEG experiments

have been attempting to do for some time. The problem is that electrical measurements are very sensitive to the exact conductivity profiles of the brain, skull and scalp, and this makes accurate localisation (or even location to the correct hemisphere) difficult. This may explain the so called P100 paradox, where in certain cases the EEG procedure suggested that the cortical generators were on the ipsilateral side of the cortex (i.e. a left visual field stimulus was represented on the left side of the visual cortex) [61,60]. This of course does not correspond to what is already known from neuro-anatomy, namely that the neuronal connections indicate a predominantly contralateral distribution (see the previous section).

The analysis of these EEG experiments was also restricted to modelling the activity as a single current dipole, and as we shall see later there is some evidence for there being more than one region active simultaneously. In this case the single dipole method would fail to even summarize the true activity in a meaningful way. MEG does not suffer to the same extent as EEG from distortions due to the conductivity profile, but the same limitations of the single current dipole model apply. This is why we have chosen to use the distributed current analysis method described in chapter 4 to provide us with an estimate for the current density within the brain. We then look at these images, post-inversion, to see whether the response is localised to a specific region of the cortex.

We finish this introductory section with a discussion on the usefulness of evoked responses, both in terms of clinical applications and their ability to provide us with unique information on brain function.

Clinical applications usually involve looking at exactly when a response to a stimulus occurs in the cortex (the so called *latency*). In some diseases such as multiple sclerosis, the latency is increased as the neurons become damaged. Evoked responses can then provide a quantitative measure of the progress of the illness. We believe that the number of such applications is likely to rise, especially as MEG offers the ability to localise active regions more accurately [53].

Kaufman suggested in 1982 that many workers were attempting to use evoked responses to gain information on brain function that was already available from psychophysical experiments and single neuron recordings [56]. These experiments (usually EEG) were simple correlational studies, where the magnitude of the response (or the frequency distribution) is studied as the properties of the stimulus are changed.

It now seems clear however, that MEG evoked responses do provide a 'unique' window on brain function. The temporal resolution (of the order of 1 millisecond), together with a spatial resolution of 1-2 cm (at superficial levels) provides a way of looking at how different regions of the brain interact in response to a stimulus. In this way it does provide complementary information to psychophysical experiments (which treat the brain as a 'black box'), and single neuron studies (which yield no information about the interconnection of neuronal populations). A good example of this is a recent experiment involving a 40 Hz steady state evoked response, carried out at the New York University Medical Center [6]. The preliminary analysis of these results seem to show that certain intrinsic properties of

individual neurons (determined by single neuron studies) can be extrapolated into the behavior of large scale neuronal populations in the cortex. If these results are confirmed then they may have important consequences for the modelling of brain function.

6.4 Experimental protocol

The stimulus

The checkerboard stimulus was provided by an Apple Macintosh computer running the Hypercard environment. The screen and computer were placed just outside the shielded room, and the subject viewed the stimulus through a specially cut hole.

Figure 6.2 shows the two octants which are to be considered in this thesis. The background grey is chosen so that the average brightness over the whole image is constant, and remains so during the reversal. The angular size of the checks increases outwards from the centre in an attempt to compensate for the fact that the central regions of the visual field are represented over a larger cortical surface. The diameter of the whole presented image was 14cm and the central dot is used as a focus point by the subject.

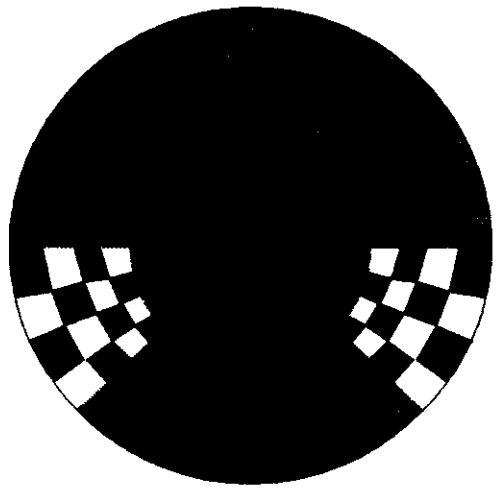

Figure 6.2 Checkerboard octants used as to produced the Visual Evoked Response

The three stimulation modes used in the experiment were left octant reversing, right octant reversing and both octants reversing together. In each experimental run, 300 stimulations were performed with roughly 100 of each stimulus mode. The computer chose which octant(s) to reverse, at random. The gap between each stimulation was also randomly chosen, between 0.6 and 1.0 seconds, to prevent subject anticipation. To allow the subject to rest, there was a rest time of 5 seconds after each group of three reversals, and during this time the subject was encouraged to look around the room without moving his head. Although data from several subjects were collected, in this thesis we present the results of analysis of data from only one subject.

Head positioning

Figure 6.3 shows a schematic of the experimental setup. The subject's eyes were approximately 1.1m from the computer screen, so the total screen image subtended around 7 degrees at the eye.

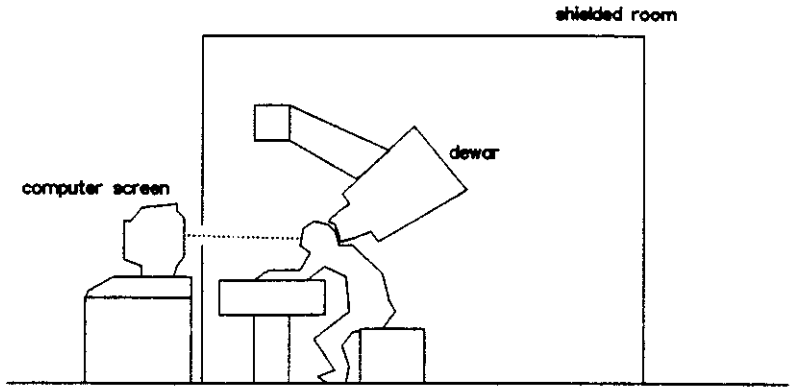

Figure 6.3 Experimental setup for the Helsinki experiment

The head position was related to the detectors by using a set of three small coils taped to the inion [44]. The three coils are arranged in a triangle around the inion, and constitute a set of three discrete magnetic dipoles. Before each experimental run these three coils are activated in sequence, and the signal from all 24 channels is inverted (using a least squares process) to give the subject's head position and orientation. At the time of the experiment, this device could give positions with a random error of around 0.5 to 1.0 cm. Systematic errors can also occur, for example the coils may be inaccurately positioned on the inion or may move slightly during the experiment.

Data collection

Data collection began at t=0 milliseconds with pattern reversal occurring at t=80 ms. The octant(s) were reversed back to their normal state at t=330 ms, and data collection ended at t=600 ms. Data were collected from the 24 gradiometer channels every 2 ms. This rather high sampling rate of 500 Hz was chosen in an attempt to identify fast acting 'transients' within the response, and hence the only analogue filters used in the experiment were a 60 Hz notch filter to remove mains noise and a 200 Hz low pass filter to reduce aliasing effects. Figure 6.4 shows a set of 5 typical scans that were obtained in this experiment. The signal to noise is generally quite good, especially in the bottom scan where the P100 response can be seen quite clearly.

One channel in the system that had a consistently bad noise performance was channel 9 (the top scan in the figure). This was probably due to this gradiometer being incorrectly balanced, and we were forced to use additional software filtering to reduce the problem. The filtering regime chosen was a band-pass filter with a sharp cutoff at 2 Hz to remove any low frequency trend, and a smooth linear cutoff between 30 and 40 Hz. The smooth cutoff was

chosen to reduce the likelihood of 'ringing' [45]. Before applying the filter to the data we tested it with a variety of test signals and impulse functions to ensure that no significant artefacts would be introduced into the signal data. Of course by using such a filter we are removing any chance of imaging fast transient responses, but the noise level was such that this was simply impossible.

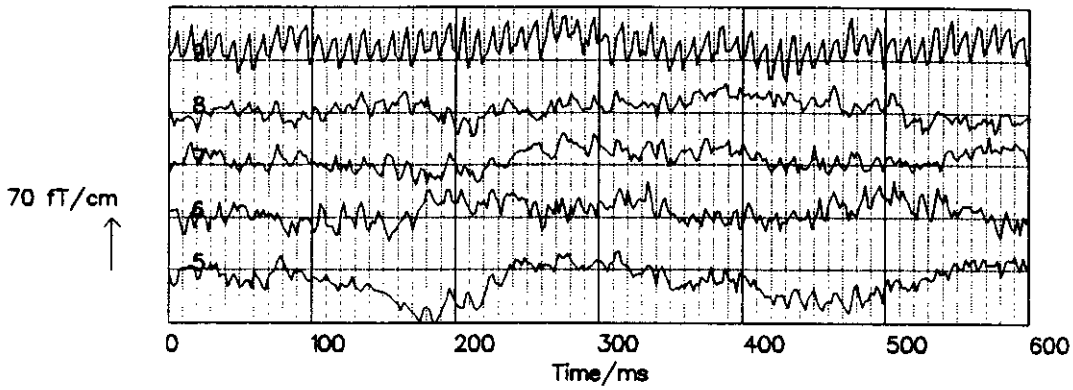

Figure 6.4 A set of five typical scans obtained in the left octant reversal experiment.

6.5 Results and analysis

In this thesis we concentrate on one particular experiment, KS05 (subject KS, run number 5). Figure 6.5 shows a flowchart of the steps followed in the analysis, with the arrows signifying the movement of data and/or information. The Transputer system consists of 30 processors working in parallel, and is therefore able to perform rapidly the large amount of numerical calculation needed to solve the inverse problem.

In this type of analysis regime, we transfer the current density solutions back to our mainframe computer for post-inversion analysis. The main reasons for doing this are that the solutions are then freely available to all members of the group, and users can make extensive use of the graphics packages and hardcopy devices supported on the mainframe. On the basis of this analysis, the user can of course re-invert the data with different parameters.

Signal viewing and filtering

The raw data were sorted according to which particular octant had been stimulated and then averaged to provide the visual evoked response. The data were zero-meaned to remove any dc baseline (which will be different on each gradiometer channel). The DataView software tool described in chapter 5 was then used to look at the data. Figure 6.6 shows the resultant 24 scans for the left octant reversal.

The scans are distributed over the figure in rough correspondence to their distribution over the bottom of the dewar. Within the dewar the 24 channels are arranged in 12 'modules', with one gradiometer measuring the x derivative of B_z and the other the y derivative. The scans are paired in figure 6.6 (and subsequent figures) to indicate this. In the figures

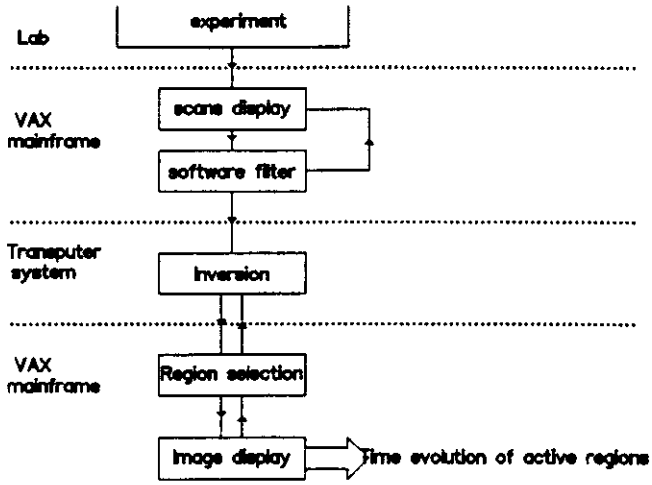

Figure 6.5 Flowchart of the data analysis path

shown, the subject's neck is to the left of the scans, the top of the head to the right (i.e the head is rotated by 90 degrees from the vertical on the page).

Even from the raw data it is clear that there is a significant response around 100 ms after the stimulus (known as a *latency* of 100 ms) , on the right of the subject's visual cortex (the top few scans in the figure). Figure 6.7 shows the filtered scans (renormalised to give the same maximum as before). Figure 6.8 shows a similar figure for the right octant reversal, and figure 6.9 shows the response for simultaneous reversal of both octants. Again, in both these figures it is possible to see the so called P100 response. The data for both octants reversing does show some evidence of being a combination of the two other responses, but this effect is more clearly seen in the solutions shown later.

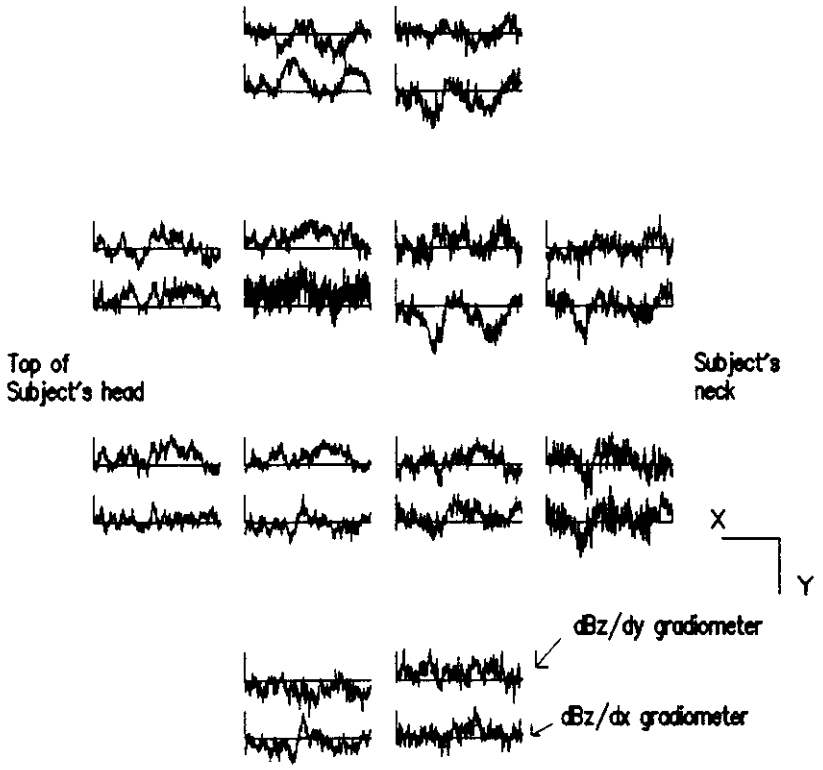

Figure 6.6 Experiment KS05, gradiometer signals for the left octant reversal, no filtering. Horizontal axis represents time from 0 to 600 milliseconds, with the stimulus occurring at 80 milliseconds. Vertical axis is signal strength, with the vertical bar at the scan start marking 40 fT/cm.

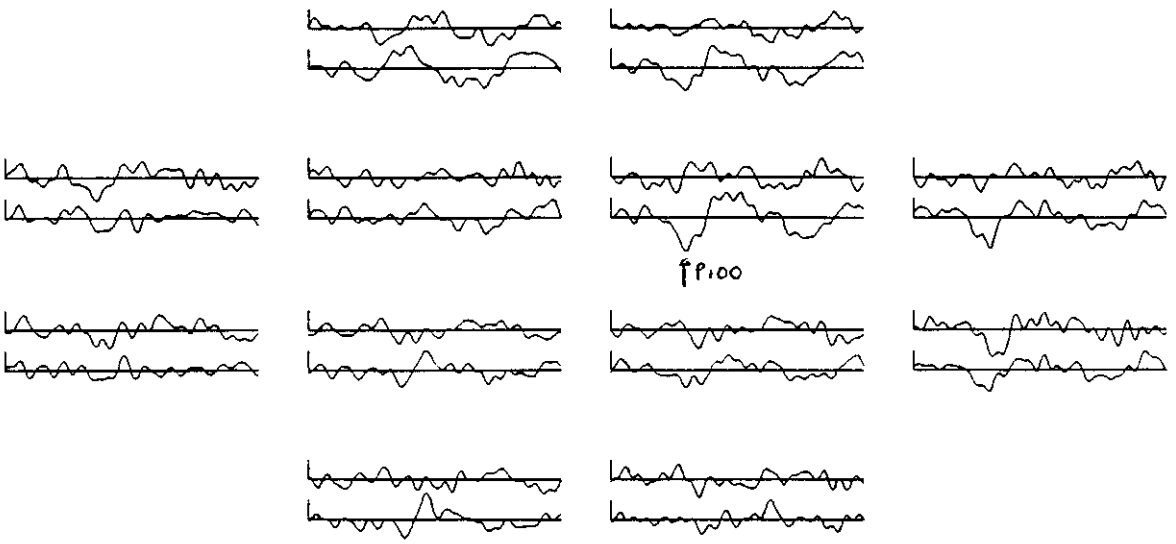

Figure 6.7 Experiment KS05, gradiometer signals for the left octant reversal, band pass filter 2-40 Hz

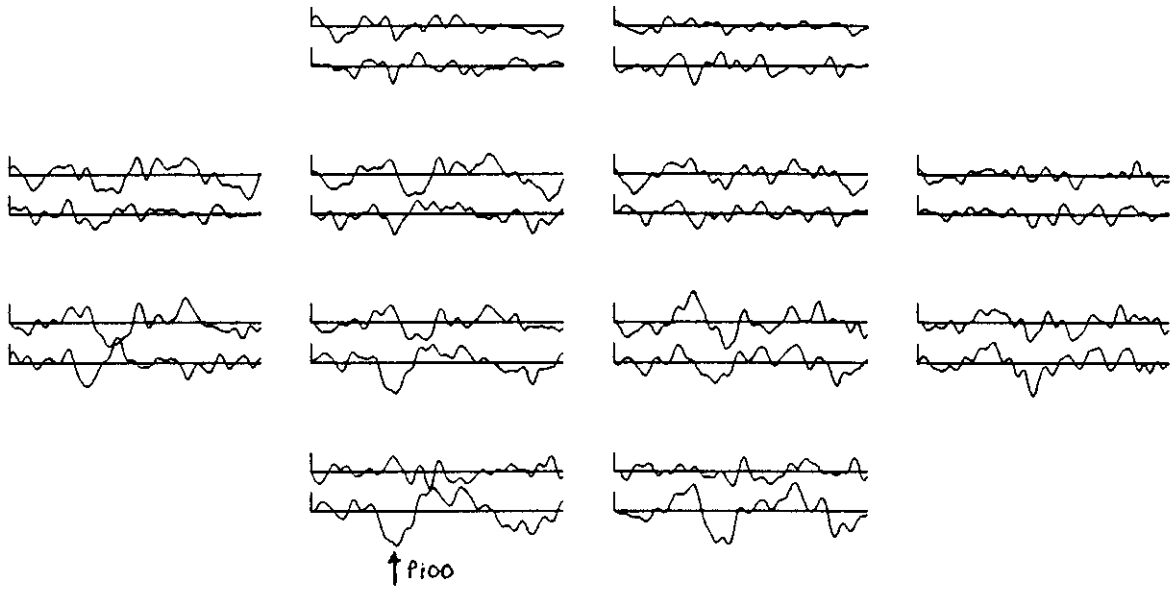

Figure 6.8 Experiment KS05, gradiometer signals for the right octant reversal, band pass filter 2-40 Hz

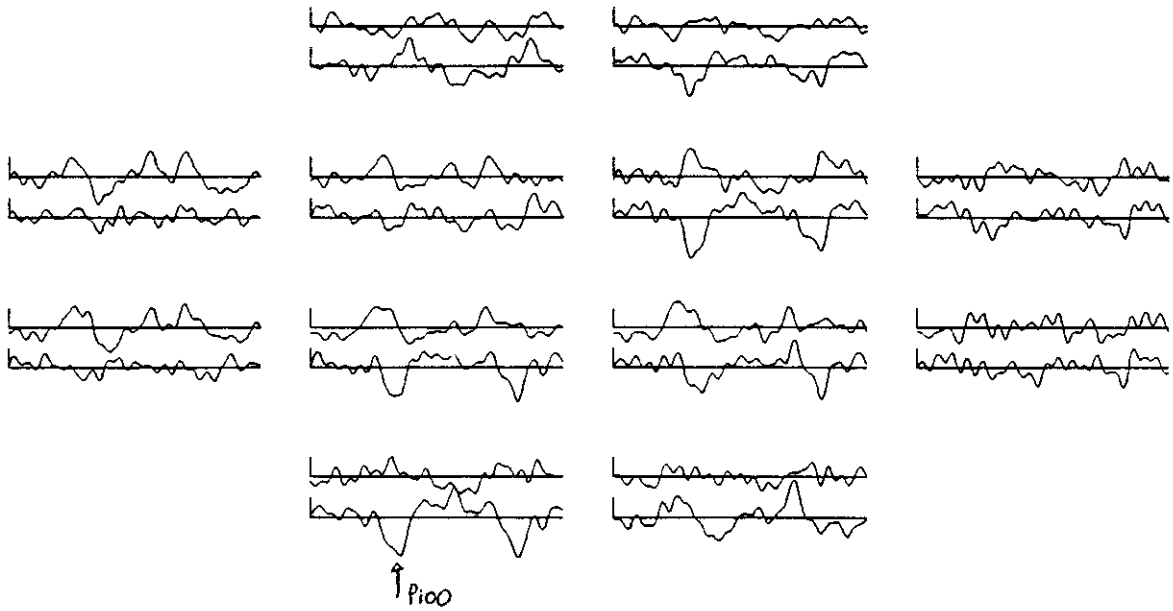

Figure 6.9 Experiment KS05, gradiometer signals for the reversal of both octants, band pass filter 2-40 Hz

Distributed current solutions

The data were inverted using the same source space geometry as was described in chapter 4 i.e. the source space was a two dimensional disk roughly 3 cm below the bottom of the detectors.

The 'end product' of the inversions on our Transputer system is a set of 300 maps of the current density and we must somehow choose how we wish to use these data. In this thesis, we use the concept of an *active region* , the location and extent of which is determined semi-automatically. This is performed post-inversion. We look for localised regions of activity after solving the inverse problem (as opposed to following the time evolution of a number of current dipoles, the approach used by Scherg [59]). The first stage in this identification is achieved by a crude automatic program which hunts through the entire data space and identifies the centre of the strongest region (i.e. where and when the magnitude of the current density is greatest). The spatial size of this region is presently supplied by the operator as a parameter but a better system would be if the computer were to grow the region outwards from the centre until the data values were below a certain threshold (exactly the way it is done in the expert system analysis). The computer then sets this region to zero in every timeslice, and begins to hunt for the next region. It repeats the process until the data space has been completely zeroed. The table below shows three regions which have been identified in the solutions for the left octant reversing, between 80 and 200 milliseconds after the stimulus (i.e. around the P100). The region size was specified as a square with a side 0.3 times the size of the diameter of the source space.

Region	Latency	Max	Lateral position
1	102	3.90	0.71 0.29
2	106	2.64	0.35 0.12
3	140	2.16	0.53 0.76

The above shows the three strongest regions. The 'max' value is the peak current density within the region (in arbitrary units), the lateral position within the source space is given as fractions of the source space diameter with the centre of the source space at (0.5,0.5), and latency is the time in milliseconds after the stimulus.

The strongest region corresponds to the P100 and the arrow map of the current density at a latency of 102 milliseconds is shown in figure 6.10. In the figure the outline (manually extracted from a video image) of the back of the head is shown with the source space represented as a circle. The central cross marks the position of the inion.

The corresponding three regions for reversal of the right octant were

Region	Latency	Max	Lateral position
1	120	5.22	0.29 0.65
2	198	3.24	0.18 0.29
3	178	2.27	0.65 0.59

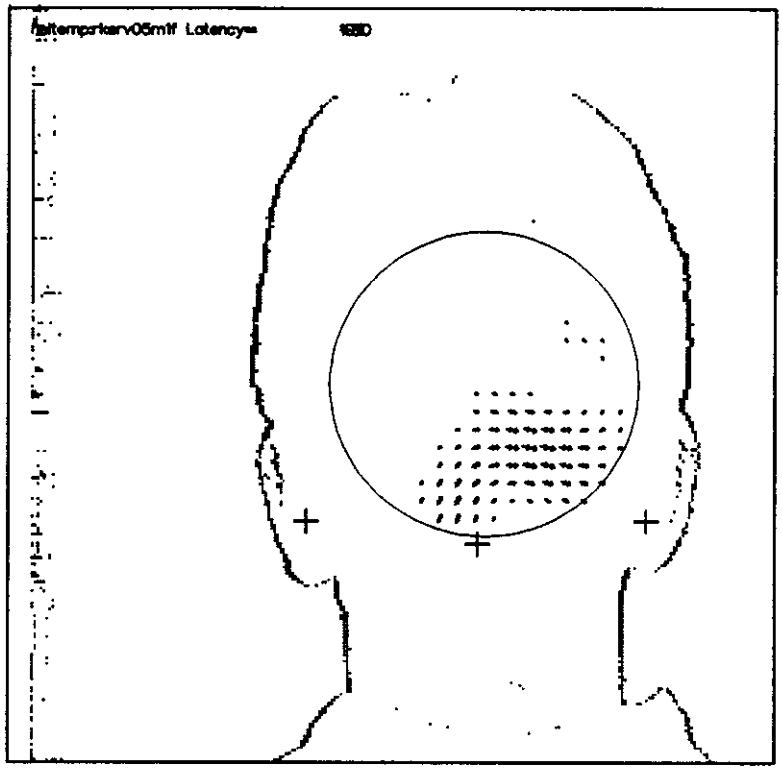

Figure 6.10 P100 response for a left octant stimulation. Latency = 102 ms.

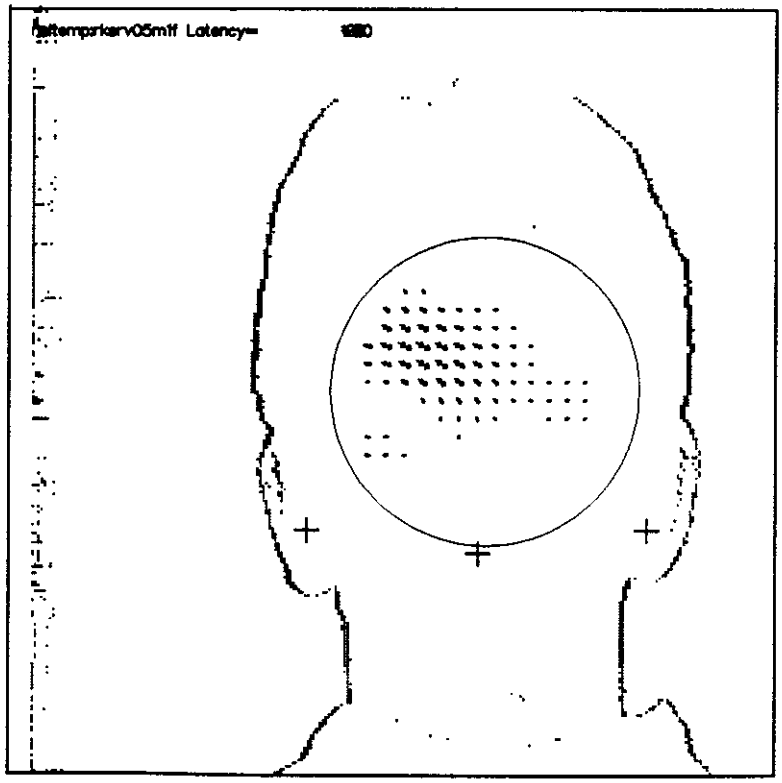

Figure 6.11 P100 response for a right octant stimulation. Latency = 120 ms.

The P100 for this reversal seems to occur 20 milliseconds after the P100 for the left reversal. Figure 6.11 shows the current density solution, as before. This difference in latency may have two possible explanations. Firstly, it is known from perception experiments that one side of the visual field is more dominant than the other and this may be reflected in the time it takes for the response to arrive at the cortex. Another explanation is that the folding nature of the cortical geometry is such that primary currents sources of the P100 for the right octant reversal are initially more radial (and hence silent) and become tangential at a later time than for the left octant. Some experimental evidence for this effect has been seen in studies comparing EEG and MEG measurements of evoked responses [9]. In these studies, the EEG response (which is sensitive to both radial and tangential sources), showed the P100 response occurring several milliseconds before the MEG response.

The active regions for the two octants are clearly in different areas of the cortex. This seems to validate our initial model, namely that there is a retinotopic map of the visual field, and that the response is predominantly contralateral to the stimulus. One feature of these two solutions that is rather hard to explain is the fact that the response to the right field of view stimulus appears rather higher up on the cortex than the response to the left octant reversal. We would have expected one response to be a mirror image (across the midline) of the response to the opposite stimulus. There are three possible explanations for this effect in our solutions. Firstly, there may well be some assymmetry in the functional allocation of the cortex, and the solutions are reflecting this. However, this hypothesis is in contradiction to what is already known about brain anatomy (see section 6.2). Secondly, Magnetic Resonance images of the subject's brain do show that the calcarine fissure does rest at a slight angle from the vertical and this would account for some of the assymetry seen. Finally an error may be introduced by the head location system in use at Helsinki. The fixing of three coils very close to a single spot (the inion) is very prone to rotational inaccuracies around this point, and any such error would introduce an upper/lower assymetry in the two responses.

In view of this, in our analysis of this experiment we will not tie the active regions identified by our method to specific physiological structures on the cortex, instead we shall concentrate on the analysis of the time variation of the activity within each region. However, we should emphasize that with a more stable head location system (for example three sets of three coils), localisation of cortical activity is much more feasible.

Another interesting feature of the two responses is that the direction of current flow appears to be more or less the same in the left octant response, as the right octant. This result has already been found in previous EEG studies with octant stimulation [60], although at present it is not known why the brain is organized in such a way.

We now look at the time evolution of the P100 area for both octants using the IMAGE software tool described in chapter 5. Figure 6.12 shows what we term an activation plot for the left octant P100. In the top left of the figure the magnitude of the current density at a latency of 102 milliseconds is represented as a line contour map. The user has selected,

with crosshair cursors, the rectangular region shown superimposed on the contour map. The system has then calculated the average current density, magnitude and direction, over this region as a function of time. The curve underneath the contour map shows this activation curve for latencies 80-180 milliseconds. The height of the graph represents the average current density magnitude, the arrow shows the average direction.

The results seem to show that the activity reappears in the same region roughly 60 ms after the initial P100 response, with the direction of the current flow reversed. This 're-entry' effect has been seen recently in auditory experiments already analysed here at The Open University [54].

The activation curve for the right octant P100 shows some startling similarities to the left octant stimulation. There is re-entry after approximately 80 ms, and again the direction is reversed. At present, we have no explanation or model for this re-occurrence of activity at the same site.

To investigate this re-entry, we instructed the system to plot what we call a *trace* of the activity for both octants. The computer draws a line on the source space, as the maximum current density moves in time. Figure 6.14 shows this for the left octant stimulation. Also shown are 5 regions which were identified using a combination of the automatic procedures described above, and manual selection. The choice is rather arbitrary, but we defined the regions by looking at where the trace 'dwelled' for a few milliseconds.

The peak activity moves from region 1 to 5 in a loop of 100 milliseconds. The activity jumped from region 1 to 2 and then tracked slowly to region 3. There was then a jump to 4, then 5, before a slow movement back to 1.

Figure 6.15 shows the same type of plot for the right octant. The geometry of the loop is different but is still present. This time there is a slow track from 1 to 2, a jump to 3 and then to 4, a slow movement from 4 to 5 before a jump back to 1.

Although these plots are useful for showing re-entry of activity, they do over-simplify the situation. Figure 6.16 shows the activation curves for all of the 5 selected regions, for the left octant stimulation, 80 to 180 milliseconds. The different activations can be identified by the colours on the figure. It then becomes clear that where the peak activity seems to jump, it is simply that one region has grown slightly stronger than the other. There are regions (3 and 4) however where the activity is in anti-phase with the activity in the original P100 region.

At the moment, we have no physiological understanding of these regions, but clearly the use of, for example, MR images would be of great benefit in identifying which areas of the cortex are being activated.

Around the region of the P100 we performed depth estimates (as described in chapter 4). The results did not show any large variation in the depth over the latency band shown, but did confirm that the source space we chose for the inversions was at a reasonable position. There was some evidence for the activity moving more deeply into the cortex at the peak of the P100, but as the distance was within the errors described in chapter 4 this cannot be

confirmed.

Finally, we investigated the stimulation of both octants. Figure 6.17 shows the current density map for a latency of 110 milliseconds, after both octants are stimulated. A time of 110 ms was chosen as it is midway between the peak P100 responses for each octant. We calculated a new data set (of gradiometer signals) by adding the left stimulus signals to the right stimulus signals, and inverted this new set. The current density solution is shown in figure 6.18. The similarity between the two images is striking and seems to suggest that, at least at the P100, there is a linear addition of the two separate responses.

6.5.1 Summary

The beauty of the distributed current method is that it allows us to investigate the time-evolution of an active site within the cortex. The use of regions identified post-inversion combines the 'summarising' effect of the dipole model with the generality of the distributed current model.

Using this method we have shown that the two primary regions of activity for the two octant stimulations are on opposite sides of the midline (as expected). The primary response arrives at a latency of 102 milliseconds for the left octant, and 120 milliseconds for the right octant. The difference in latency may represent a true difference in perception of left and right visual fields, or may arise from the axial/tangential distribution of the current sources around the P100.

The analysis of the time evolution of these regions show that both stimulus modes produce re-entry after 60-80 milliseconds, with the direction of the current flow reversed on re-occurrence of activity. The activation curves for these two regions are remarkably similar. Some researchers have suggested that the brain has some intrinsic 'normal frequency modes' of operation (chapters 10 and 11 of [43]). Any transient stimulus (such as the ones described in this chapter), will then generate a response which can be modelled as a Fourier summation of these modes. If this is the case, it seems likely that the time activation of two stimulated regions, where the only difference between the stimuli is their position in the visual field (and hence their representation on the cortex), will be similar.

Plotting the maximum current density as a trace over the source space indicated a loop like structure for both octants, although it is unlikely that the activation moved smoothly along this pathway. Region analysis seems to show that the activation within some areas varies roughly in phase with the activation within the initial P100 region, while some areas are active when the P100 region is silent.

The current distribution obtained for both octants reversing was shown to be very similar to that from a linear combinations of the signal from individual octants. More analysis of this effect at different latencies is under way, but it seems to validate the physiological model of the brain i.e. there is a contralateral separation of left and right visual field information at the optic chiasm, at least for the P100 response. We have analyzed this effect across the entire latency span, rather than just at the P100. Our conclusions are that for latencies up

to around 200 ms, if there is a strong response to both left and right octants (for example the P100), then the linear superposition effect described above still takes place. After 200 ms, the situation seems more complicated. Even at latencies where the individual response to left and right octants is strong, the response to both octants is not the same as a linear combination of the two individual responses. This seems to suggest that we may be seeing the onset of cognitive processes, although the results are very preliminary.

To make any strong conclusions about the operation of the human brain we need to analyze data from more subjects. Preliminary data from one subject, SA, has confirmed both the contralateral separation of responses and the re-entry effect seen in the P100 region. Also, if more accurate functional localisation is to be carried out, then in future we must make sure that the head location system is stable enough, enabling us to relate the solutions directly to anatomical information (for example MR images).

Despite the limitations of this particular study however, we believe that it does show the potential of this kind of analysis in investigating the time evolution of specific functional areas within the brain. The same kind of region analysis procedures we have described in this chapter are currently being used to analyse a variety of evoked responses, both auditory and visual, steady state and transient, here at the Open University. This ability to analyse data from different stimulus paradigms is providing us with a new body of knowledge on how the brain organizes its response to the outside world, and is even beginning to provide glimpses of how higher cognitive functions may be carried out.

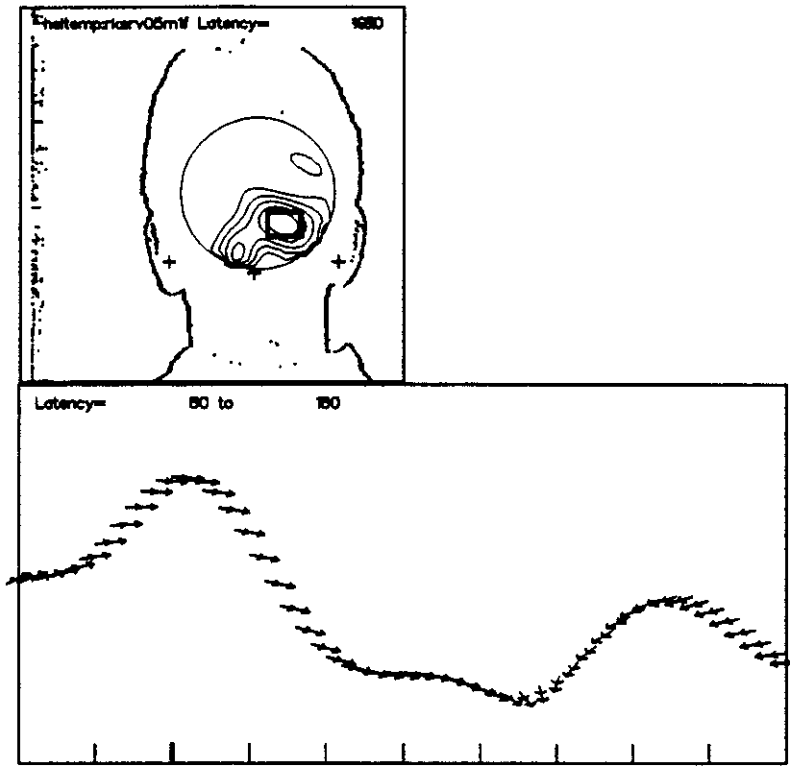

Figure 6.12 Activation curve, P100 response for a left octant stimulation. Latency = 102 ms.

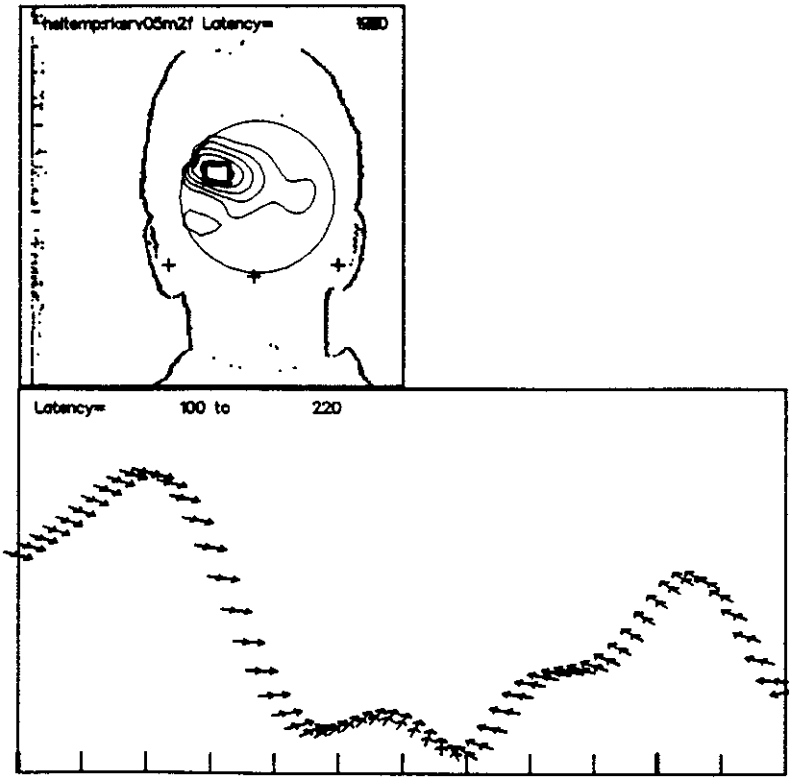

Figure 6.13 Activation curve, P100 response for a right octant stimulation. Latency = 120 ms.

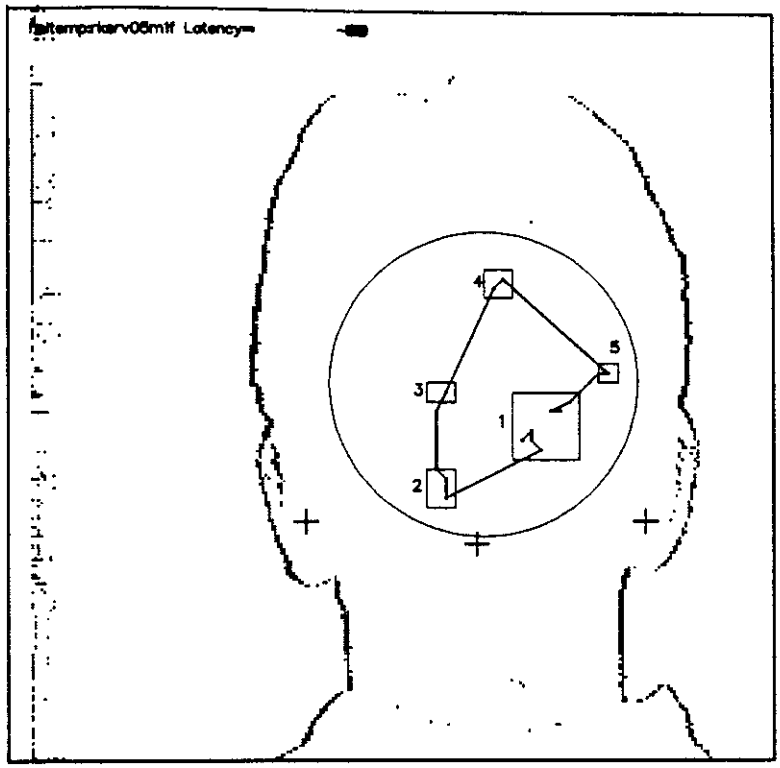

Figure 6.14 Trace plot, P100 response for a left octant stimulation. Latency = 80 - 180 ms.

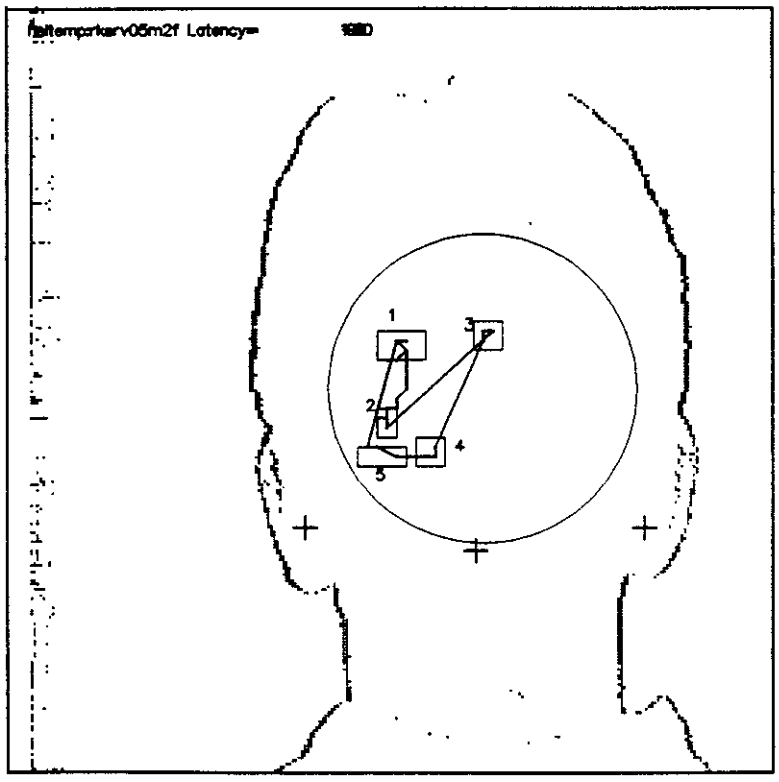

Figure 6.15 Trace plot, P100 response for a right octant stimulation. Latency = 100 - 220 ms.

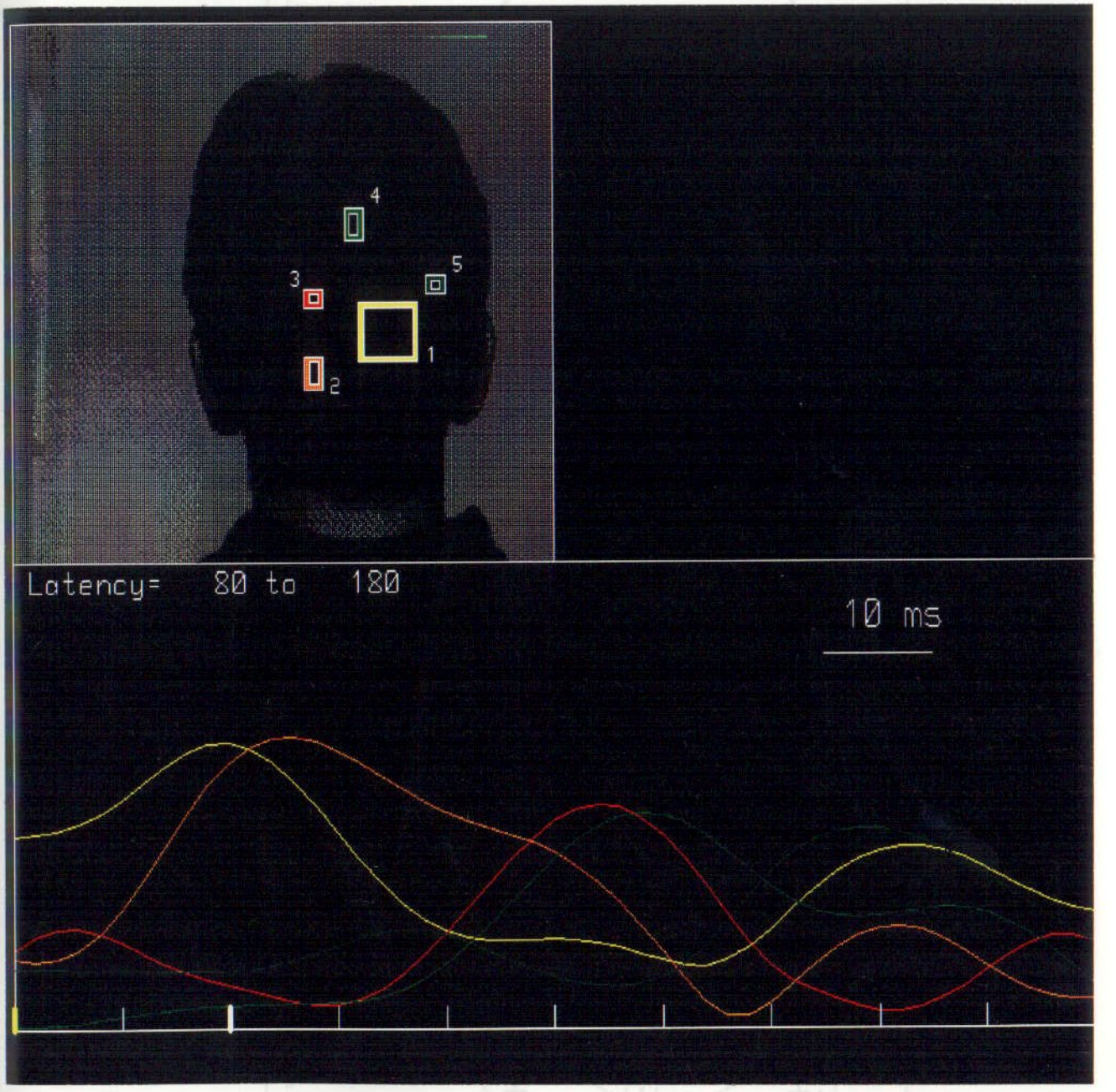

Figure 6.16 5 activation curves, P100 response for a left octant stimulation, Latency = 80 - 180 ms.

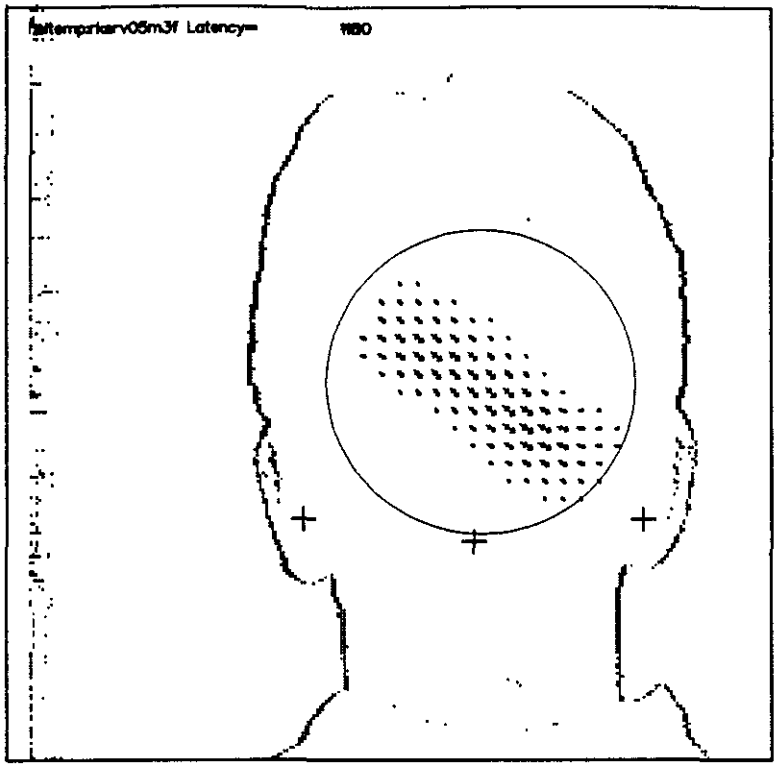

Figure 6.17 Current density solution, left and right octants reversing. Latency = 110 ms.

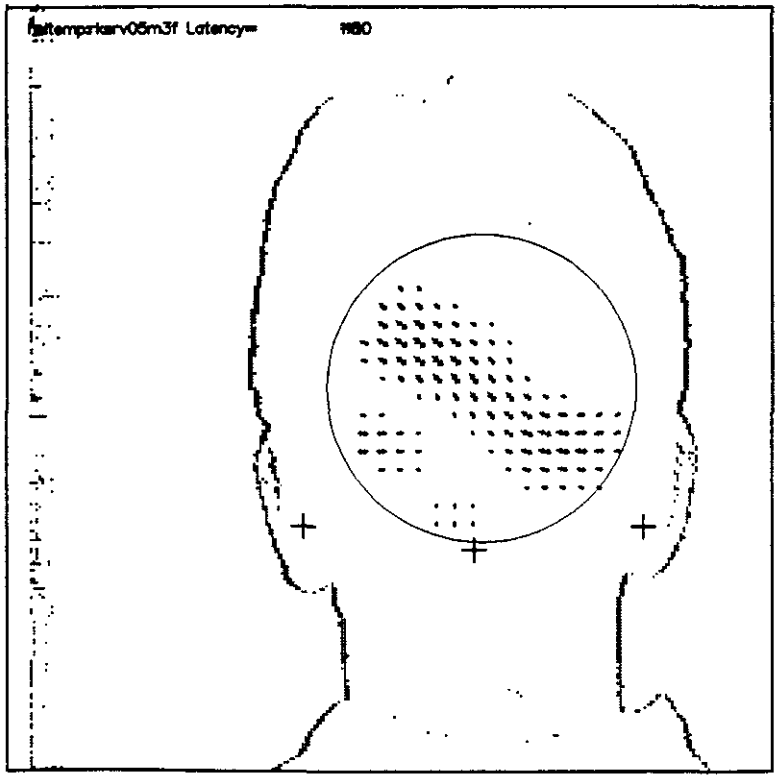

Figure 6.18 Current density solution, Calculated sum of left and right octant reversals. Latency=110 ms.

Chapter 7

A thin-film project

In this chapter we describe a test project to construct a gradiometer using the kind of thin-film techniques used in the micro-electronics industry. The advantages of using thin-film fabrication are three-fold.

Firstly, the gradiometers will have a high intrinsic balance because of the accuracy of coil definition that is possible. The standard axial gradiometer used in our lab has an initial balance of around 10^{-3} to uniform fields i.e. the effective unbalanced area of coil which is sensing uniform field is 1/1000 of the area of the bottom coil. The first reported thin-film gradiometer was fabricated by Ketchen et al in 1979 [26] and had an intrinsic balance of 10^{-4} and a final balance after modification of 10^{-5}.

Secondly, thin film gradiometers are very compact as they are fabricated on thin silicon substrates which are 0.25mm thick. This means that it should be possible to pack many gradiometers into a small space.

Thirdly, when the fabrication procedure has been perfected, it should be possible to manufacture large numbers of gradiometers with identical characteristics. This would be especially useful for multichannel systems. At present this goal has not been realised as the yield from fabrication is still low.

The most impressive thin-film gradiometers are those which have a DC SQUID fabricated directly into the gradiometer [27,10]. As shown in chapter 3, these devices can have very impressive sensitivities to current sources. Here at the OU we decided on a more modest approach which involved producing a discrete thin-film gradiometer which would be coupled to one of our standard, commercially made RF SQUIDs. The goals of the project were

- To establish some expertise in thin-film fabrication, with possible spin-offs in SQUID fabrication etc..
- To produce an easily reproducible, compact gradiometer with high intrinsic balance.

Unfortunately, although we were able to construct a suitable device, it was not superconducting. However, we have decided to present our thin-film procedures in some detail here, as we feel there is currently a lack of sufficiently detailed thin-film 'recipes' in the published literature. Our experiences suggest that with a suitably advanced clean room facility our project could have succeeded, but whether it is possible to manufacture large numbers of

thin-film gradiometers in a reasonable amount of time (for use in multichannel facilities) is not clear at the present time. It should be noted that despite the attractions of using thin film gradiometers, all large multichannel systems currently in operation use hand-wound gradiometers (or thick-film devices).

7.1 Design

One consequence of using RF SQUIDs was that it was necessary to use several turns on each of the gradiometer coils. The gradiometer was first designed using the optimisation procedure described in chapter 3. The gradiometer was of the form shown in figure 3.5 and had to be confined to an area $W \times Z_{max}$ with $W = 1.8$cm and $Z_{max} = 5$cm. The device chosen had the following dimensions.

```
N1=3
N2=3
N3=3
Z0=0.0 cm
Z1=1.0 cm
Z2=1.5 cm
Z3=3.5 cm
Z4=4.0 cm
Z5=5.0 cm
```

This represents a symmetric geometry with the middle coil having twice the area of the bottom and top coils. The optimisation assumes multi-turn rectangular coils which are impossible to fabricate on a planar substrate. Instead, tightly wound flat spirals with the same average dimensions as the rectangles are used.

Figure 7.1 shows a schematic of the planar device (known as OPTPOD2) with the dimensions critical for balancing. Note that the dotted lines represent crossover structures and must not connect with the lines they pass over (this has consequences for the fabrication, see later). In the final design these lines will actually lie along the $x = 0$ line, so that they do not contribute to the flux gathering and alter the device balance. In the diagram however, they are shown displaced from this line for clarity. The device dimensions are not shown to scale. Recalling equation 3.24 for balance to a uniform field (i.e. $n = 0$)

$$0 = \oint x dy \tag{7.1}$$

This can be re-expressed as a summation over all tracks in the gradiometer

$$0 = \sum_{i=1}^{alltracks} x_i \Delta y_i \tag{7.2}$$

By examination of the figure, it was noticed that if $B = 2A$ and $V_2 = 2V_1$ then the above condition would be satisfied. So the gradiometer was designed so that the vertical separation

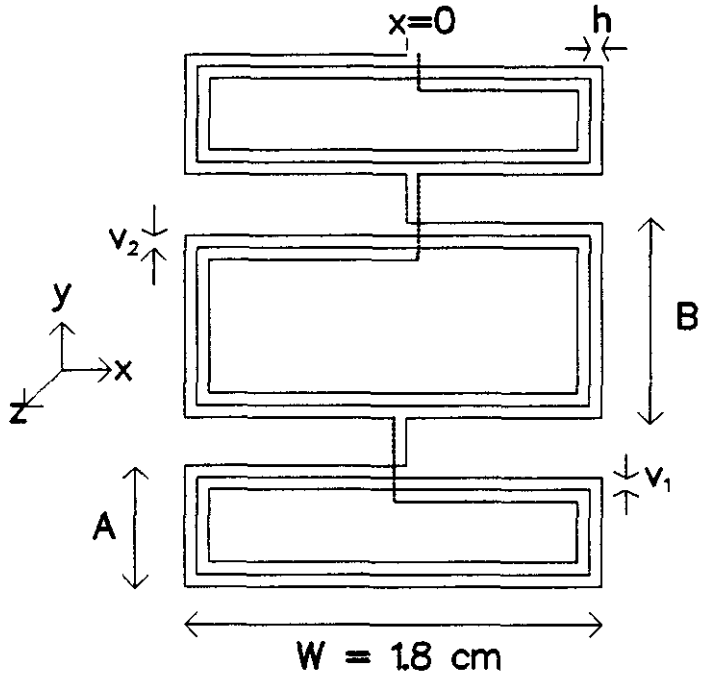

Figure 7.1 The OPTPOD2 gradiometer.

of the spiral loops was twice as big in the middle coil, as in the two outer coils. The horizontal track separation, h, was the same in all three spirals. The gradiometer would then in theory be balanced to a uniform magnetic field. The corresponding equation for the balance due to a field varying uniformly in x i.e. $n = 1$ can be obtained by writing equation 3.27 as a summation

$$0 = \sum_{i=1}^{alltracks} x_i^2 \Delta y_i \tag{7.3}$$

and the equation for the $n = 1$ y sensitivity is

$$0 = \sum_{i=1}^{alltracks} y_i^2 \Delta x_i \tag{7.4}$$

These conditions are not satisfied completely. The summation actually returns a result of $2 \times 10^{-9}\mathrm{m}^3$ for the x balance and $3 \times 10^{-8}\mathrm{m}^3$ for the y balance to uniform gradients. To see how significant this imbalance was, we constructed in simulation a gradiometer with two similar sized coils to the ones in OPTPOD2, but measuring the first order gradient in y. The value obtained from equation 7.4 was $1 \times 10^{-5}\mathrm{m}^3$, which shows the intrinsic balance in OPTPOD2 is around 3/1000 for uniform gradients.

This was the best realization of the optimum gradiometer described at the beginning of this chapter, and an attempt was made to fabricate it.

7.2 Fabrication

The fabrication of OPTPOD2 was carried out in the Silicon Laboratory at Leicester Polytechnic. Niobium was chosen as the superconductor because it is a stable refactory metal,

which grows a native oxide relatively slowly [22]. The tracks of OPTPOD2 are 50μ wide and 0.3μ thick. This relatively large line-width was chosen to reduce the chance of a small dust particle destroying an entire track width. Note that crossovers must be fabricated, and so the device consists of three layers. The first patterned layer is niobium and defines most of the coil structure. The second layer is a thin layer of electrical insulator (pyrex or silicon dioxide) which covers most of the wafer apart from a few select areas known as vias. The third layer is niobium and completes the electrical circuit by connecting one via to another. Figure 7.2 shows a typical crossover structure. The top layer of niobium is acting as a connecting path between two niobium pads. Note that the thickness of the films has been exaggerated for clarity.

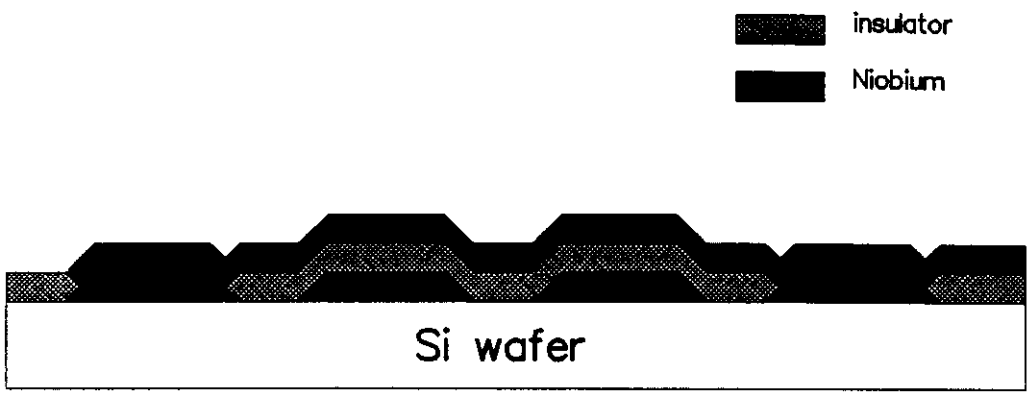

Figure 7.2 Crossover structure.

7.2.1 Niobium films

The niobium films were deposited using a technique known as dc sputtering [12,13,14]. Figure 7.3 shows the apparatus used. The chamber is pumped down to as low a pressure as possible. In the case of the Leicester system this was about 10^{-6} torr. The chamber is then filled with 1-10 millitorr of argon and a potential difference of 400V is applied between the substrate holder and the niobium target. A glow discharge is produced in the argon, and argon ions are accelerated towards the niobium target. These ions strike the niobium surface and atoms are ejected from the metal with sufficient kinetic energy to allow them to cross the chamber and coat the substrate surface. With a sputtering voltage of 400V and a 2A current, deposition rates of $1 nms^{-1}$ were achieved. Instead of being earthed, the substrates are connected to -24V. This is done so that there is a small amount of argon bombardment of the wafer surface, which 'cleans' the niobium film as it is deposited. This so called bias sputtering can potentially produce very high quality films [12].

A bare silicon wafer was cleaned (see later) and then sputtered with a uniform thin-film of niobium, of thickness 307 nm. The resistivity of the film was measured using a 4 point probe and was found to be $35 \times 10^{-8} \Omega m$, which is a factor of 2.2 times greater than the normal bulk resistivity of niobium. This is similar to films produced by other groups [10].

To check if there was any significant contamination in the film, energy dispersive x-ray

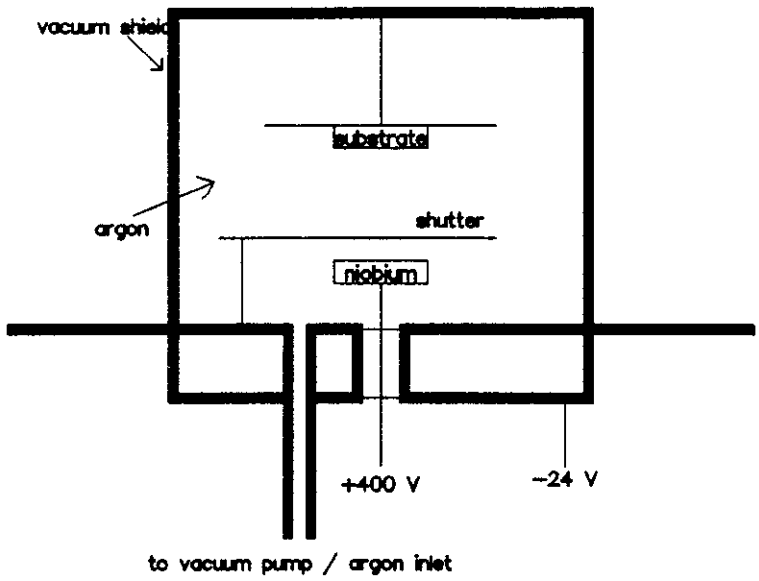

Figure 7.3 DC sputtering system.

analysis [15] was carried out in the Open University's Electron Microscope suite. A typical background corrected spectrum is shown in figure 7.4. The software has marked significant peaks with their atomic 'signatures'. The gold peaks arise because the sample had been

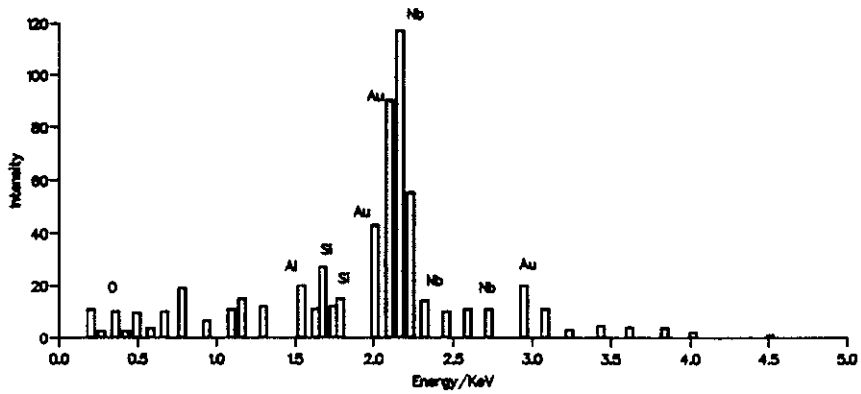

Figure 7.4 Energy-dispersive x-ray spectrum of a sputtered niobium film.

coated with a few nm of gold prior to electron microscope observation. The Si and O peaks are probably due to the fact that this type of analysis samples a volume which extends into the SiO surface of the wafer. Note that Nb is the predominant metal in the sample, but there is some Al contamination.

The niobium was tested for superconductivity by slowly immersing the film in a liquid helium dewar. A 4 point contact array was attached to a small piece of the film using pressed Indium solder contacts. A calibrated carbon resistor was used as a temperature sensor. The resistor and niobium film were encased in an evacuated brass cylinder to isolate the measurement from the liquid helium. Figure 7.5 shows the cooling curve for the film and clearly shows a transition to a superconducting state. The film quality is immediately seen to be rather poor as the residual resistance ratio $\frac{R(300)}{R(transition)}$ is only 1.4. A good niobium

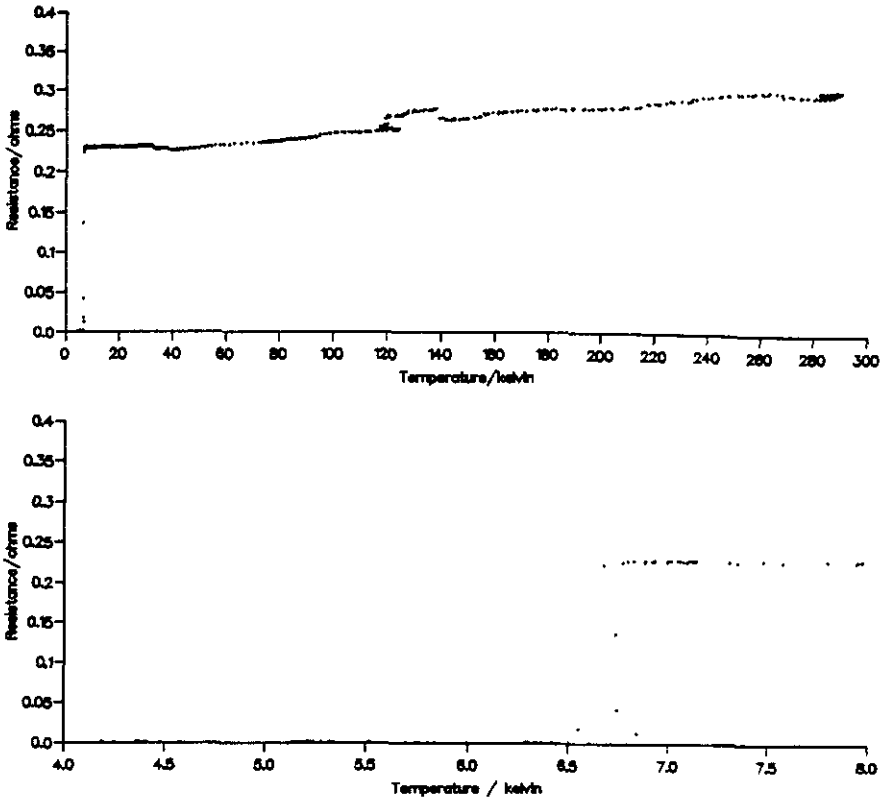

Figure 7.5 Cooling curve for a sputtered niobium film.

film will have a residual resistance ratio of 4 or more [22]. The transition was estimated to be 6.7 ± 0.1K. The scatter on the transition is due to the sample being moved in and out of the liquid helium, causing a thermal lag in the carbon resistor.

The transition for bulk niobium is around 9.2K so again we have an indication that the film quality is rather poor.

The poor quality of the film is probably due to the vacuum pressure that the Leicester system is able to pump down to. A 'rule of thumb' for niobium films is that the transition temperature decreases by 1K for every 10^{-7} above 3×10^{-7} torr [16]. This is consistent with the vacuum pressures we observed.

Despite reservations about the film quality, the films are superconducting in liquid helium and so we believed it was possible to construct a working device.

7.2.2 Insulating films

The insulating films used were deposited using rf sputtering. The dc sputtering technique described earlier cannot be used as it is impossible to maintain an insulating target (in our case pyrex) at a high potential. In rf sputtering, the target is surrounded by an rf source which is driven at 13.56 MHz, via an impedance matching network. If there were no collisions with argon atoms, a free electron in the vacuum chamber would oscillate in simple harmonic motion. However, if collisions occur the electron moves more randomly and can absorb energy from the rf field. Eventually the electron will have sufficient energy to

liberate an electron from an argon atom to create an ion. In this way an argon plasma can be supported. The pyrex target gains a negative electric charge from free electrons which are accelerated onto the target surface by the rf field. This negative charge in turn attracts the heavy argon ions onto the target, and sputtering takes place. A typical power of 1kW is used and this gives a sputtering rate of around 5nm per minute.

7.2.3 Film patterning

It is necessary to pattern the thin films, to define the spiral coil shapes, vias etc. One possible approach would be to selectively etch away certain parts of the film using an appropriate acid. This has two disadvantages. Firstly, niobium is very difficult to etch chemically and would require a rather nasty mix of hydroflouric and nitric acids. Secondly, and more importantly, it would be very difficult to etch the top layer of niobium (to form the crossovers) without damaging the underlying layers.

A more suitable technique was chosen, the *single step chlorobenzene lift-off process* [17,18,19]. This was first developed by IBM to pattern sub-micron structures very accurately. Our line widths are extremely crude in comparison but the process does not suffer from the two complications outlined above.

The lift-off process is outlined in figure 7.6. A silicon wafer is coated with 1.5μm of a special chemical known as a photoresist (a). In our case the resist is Shipley AZ1400-27 [21]. This consists of three components; a photoactive compound, a resin, and a carrier solvent. In this case the resist is a positive one and the photoactive compound is known as an inhibitor i.e it protects the resin system from chemical dissolution by the developer.

The photoresist is baked, driving off the solvent and is then exposed to ultraviolet light (405 nm) through a mask (b). The masks we use consist of a glass plate coated with chromium metal. The holes in the chromium define the patterns that we wish to produce. For the lift-off process, the holes define the areas on the wafer which will eventually contain niobium.

Where the ultraviolet strikes the resist layer, the photoactive inhibitor is broken down into a carboxylic acid which is soluble in the alkaline developer solution. The development stage preferentially removes the areas of resist which have been exposed (c).

In the next step, 300 nm of niobium or pyrex is sputtered over the whole surface (d). The wafer is then immersed in acetone (or N-methyl pyrillodone), which will dissolve away the remaining 'hard' photoresist structures and hence remove the unwanted film (e). For this process to work properly, without film tearing, it is necessary for the photoresist image to have the undercut profile shown in figure 7.6. However, normal photoresist images actually have a slight overcut rather than an undercut. To achieve the required profile, the whole wafer is immersed in chlorobenzene, prior to exposure. The chlorobenzene chemically modifies the surface of the resist, making it less susceptible to developer attack.

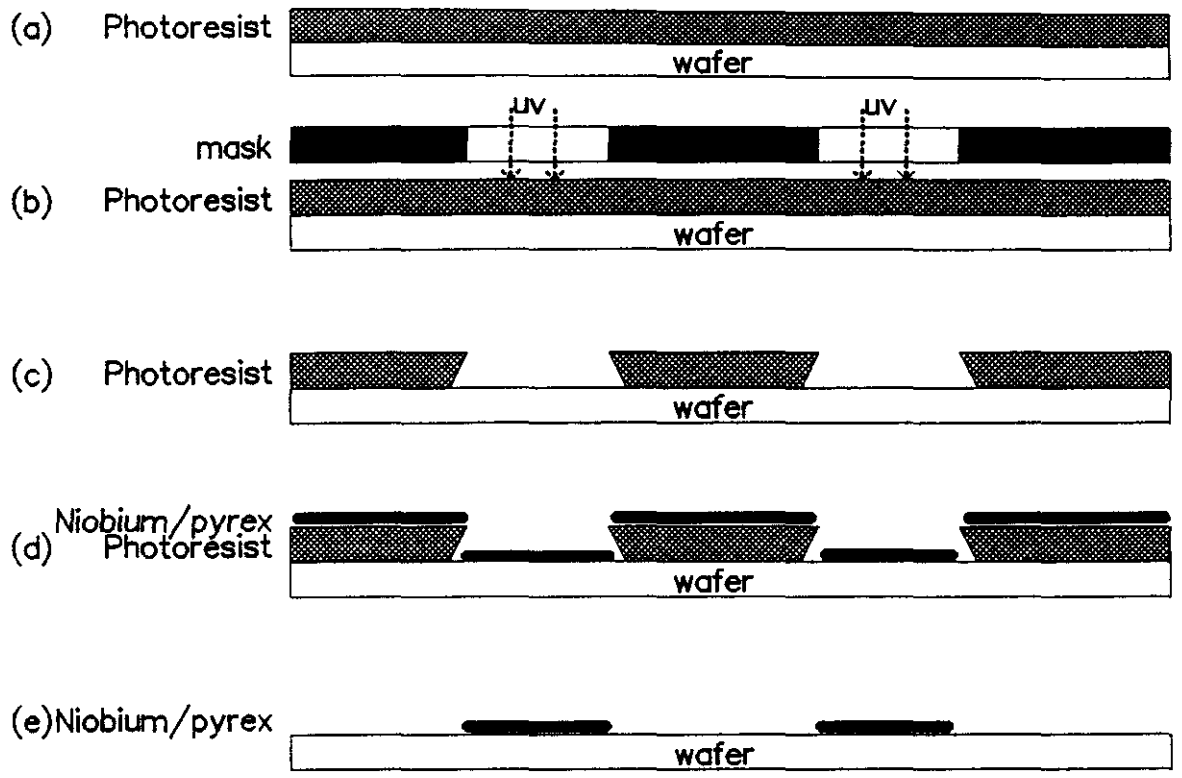

Figure 7.6 Single step chlorobenzene lift off process.

7.2.4 Mask production

The masks used in the photolithographic process were produced by a commercial firm, Compugraphics Ltd of Stratchclyde, and consist of a 10cm square glass plate with a thin film coating of chrome. The data defining OPTPOD2 as a thin film device were converted into the format required by Compugraphics and figure 7.7 shows the mask for the bottom layer of niobium. Note that, at this resolution, the individual spiral tracks are not visible. The two contact pads (one on the bottom layer, one on the top layer) needed to connect the SQUID to the gradiometer were taken as far away from the device as possible, and made as small as possible, to minimise any field distortions which will degrade the balance. OPTPOD2 occupies the central part of the wafer and there are three other structures in the 'spare' space round the edges. The first is a simple contact block arrangement which was used to test the ability to make connections to the thin films, and also to test the resistivity of the niobium films. The second device is a first-order, one-turn gradiometer, and the third is a concentric coil gradiometer made from square spirals. Also shown are the 4 small alignment marks which allow registration of the three layers

7.2.5 Process Recipe

- Grow 1 μm of oxide on a silicon wafer using a steam process.

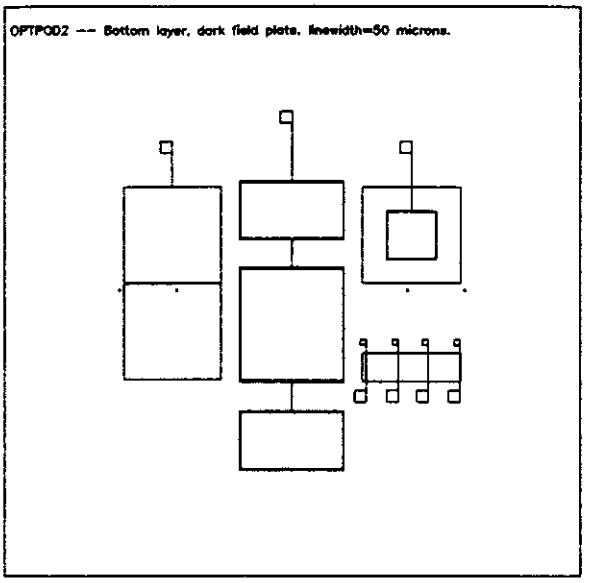

Figure 7.7 OPTPOD2, bottom layer mask.

- Bake at 200°C for 15 minutes to dehydrate wafer surface.
- Spin-on 1.5 μm of photoresist
- Bake at 90°C for 30 minutes
- Soak in chlorobenzene for 10 minutes.
- Expose to 60-65 mJ at 405 nm.
- Develop in Shipley 1:1 developer water for 1 minute.
- Immerse in de-ionised water.
- Rinse in de-ionised water.
- Immediate blow dry.
- Examine.
- Sputter 300nm of niobium.
- Lift-off.
- Rinse in de-ionised water.
- Immediate blow dry.
- Examine.
- Spin-on 1.5 μm of photoresist
- Bake at 90°C for 30 minutes

- Soak in chlorobenzene for 10 minutes.
- Expose to 60-65 mJ at 405 nm.
- Develop in Shipley 1:1 developer water for 1 minute.
- Immerse in de-ionised water.
- Rinse in de-ionised water.
- Immediate blow dry.
- Examine.
- Sputter 350nm of Pyrex.
- Lift-off.
- Rinse in de-ionised water.
- Immediate blow dry.
- Examine.
- Spin-on 1.5 μm of photoresist
- Bake at 90^{o}C for 30 minutes
- Soak in chlorobenzene for 10 minutes.
- Expose to 60-65 mJ at 405 nm.
- Develop in Shipley 1:1 developer water for 1 minute.
- Immerse in de-ionised water.
- Rinse in de-ionised water.
- Immediate blow dry.
- Examine.
- Sputter 400nm of niobium.
- Lift-off.
- Rinse in de-ionised water.
- Immediate blow dry.
- Examine.
- Cut wafer.
- Test device.

7.2.6 Process Details

Baking

The initial hard bake at 200°C drives off any residual moisture from the wafer and improves the photoresist adhesion. It is carried out on a hotplate and the baking time and temperature are not critical. The bakes at 90°C are carried out in a thermostatically controlled oven, with the temperature monitored by a thermocouple. Both the baking temperature and the time are critical. The oven should be allowed to regain its operating temperature of 90°C before timing of the bake commences. Note that after baking, the wafer should be left to cool for five minutes.

Photoresist coating

The photoresist is spun-on to the wafer using a vacuum spinner. The best coatings were achieved using the following protocol

- Blow wafer clean using a nitrogen gas jet
- Pour on some photoresist so that around 1/2 of the wafer is coated centrally.
- Immediate spin, 400 r.p.m for 30 seconds.
- Blow clean.

Chlorobenzene soak

The wafers were immersed in chlorobenzene for 10 minutes, without any agitation. After the required time, the wafers were quickly removed from the solvent and the back of the wafer was dried with with the nitrogen jet. The wafer was immediately spun on the spinner to dry off the top surface.

Exposure

Before exposure, it is important to ensure that the masks are clean. In most cases a simple blow with the nitrogen to remove dust etc is sufficient, but if photoresist residues build up on the mask then it is necessary to clean the mask using the following technique

- Ultrasonic agitation in acetone for 30 minutes.
- Ultrasonic agitation in N-Methyl Pyrillodone for 2 minutes.
- Immerse in de-ionised water.
- Rinse in de-ionised water.
- Immediate blow dry using the nitrogen jet.

Developing

Two clean pyrex beakers were used for the development stage. The first beaker held 600ml of 1:1 developer solution. The wafer was immersed in this bath and agitated gently by hand for exactly 1 minute. The wafer was then removed and immediately plunged into the second beaker containing 1 litre of deionised water. The wafer was agitated to ensure the developer was rinsed off the wafer surface.

Wafer rinsing and drying

At many points in the device fabrication, the wafer has to be rinsed with very high purity water, and then dried. To prevent the formation of drying stains, the following protocol was established

- Immersion in a relatively clean bath of de-ionised water, together with agitation of the bath.
- Removal of the wafer from the bath, and then immediate rinsing of the wafer surface with a jet of 18 $M\Omega cm^{-1}$ de-ionised water.
- Immediate blow dry of the wafer surface.

Sputtering

The procedure for film sputtering was as follows

- Mount wafer on a brass heatsink.
- Pump down system overnight to achieve 2×10^{-6} torr.
- Admit 1 - 10 millitorr of argon.
- Switch on power supplies and create argon plasma.
- Leave sputtering for 15 minutes with a shutter over the wafer.
- Open shutter and deposit required film thickness
- Switch off power supplies.
- Turn off vacuum pumps and vent system to argon.
- Leave in argon for 15 minutes to cool
- Vent chamber.

Note that each of the two upper layers are 50nm thicker than the previous layer. This is to make sure that each layer is able to successfully step over any structure already present.

The heat-sinking was found to be necessary for two reasons. Firstly, the lift-off stage was very difficult and often needed prolonged periods of ultrasound agitation to remove the

photoresist (which risks damage to the film). Secondly, some film depositions resulted in local black 'bubbles' rather than smooth films. Both of these problems are indicative of overheating of the wafer surface which bakes the photoresist hard and can damage the film. The problem was solved by applying a small amount of vacuum grease to the back surface of the wafer and pressing it down onto a large block of brass, prior to sputtering. This appeared to solve the two problems satisfactorily.

Another process modification that was tried was a blanket exposure of the photoresist to ultraviolet light for 75 seconds, prior to sputtering. This exposure breaks down the photoactive compound in the photoresist and prevents the photoresist hardening during sputtering [20]. This blanket exposure did not seem to significantly alter the ease of lift-off however.

The actual argon pressure and power supply parameters must be adjusted at the beginning of the sputter run to achieve the desired sputtering rate. The pre-sputtering of the target with a closed shutter over the wafer is used to remove any surface contamination or oxide layer on the niobium.

The film thickness is monitored using a quartz crystal mounted adjacent to the wafer. As film is deposited on the crystal its oscillation frequency changes and external calibration electronics transform this frequency change into a thickness reading.

The wafer is allowed to cool down in argon for 15 minutes so that there is no chance of rapid oxide growth on the niobium metal when the hot wafer is exposed to air. Also, the risk of thermal shock to the film is reduced.

Lift-off

The following lift-off protocol was found to work if the wafer had been heatsinked.

- Immerse in acetone for 10 minutes.
- Immerse in N-Methyl Pyrillodone for 5 minutes.
- Immerse in water bath to remove solvent.
- Rinse wafer in DI water.

N-Methyl Pyrillodone is an organic solvent which is especially useful for removal of photoresist residues. For a troublesome lift-off problem it can be heated to 80°C. It also has the advantage that it can be rinsed off in water.

Despite the fact that ultrasound is not needed in the lift-off procedure (which can remove all the film!), we still had serious problems with film lifting off the substrate even when we wished it to remain! This meant that the lift-off procedure was the stage at which most device fabrication runs failed, and the rather poor yield that we obtained reflected this. There are two explanations for this problem. Firstly, incomplete development or rinsing would leave behind a residue on the wafer which would lift-off in the acetone, destroying

the thin-film track. Secondly, the sputtering stage could be producing films with a large amount of stress in them, which would be easily separated from the wafer surface.

Wafer cutting

After fabrication, the rectangular OPTPOD2 must somehow be extracted from the central part of the wafer. The silicon wafers we use are sliced from a large single crystal of silicon, and must be cut along one of the crystal axes. A flat on the edge of the wafer marks one of these easy directions and all cuts must be made parallel or anti-parallel to this flat.

A cutting rig was built which allowed translation of the wafer accurately in x and y and allowed a weighted diamond stylus to scribe the wafer along the easy directions. After scribing through approximately 1/3 of the wafer, the wafer was removed from the scribing table and broken across straight edges on the scribe lines. This could be a very harrowing experience after spending 4 days fabricating the device. Silicon is rather brittle and extreme care is needed when attempting to manually cut the wafer.

7.2.7 Device testing

After fabrication the first test the device goes through is a simple measure of its resistance. From the path analysis described at the beginning of the chapter, we know that OPTPOD2 has a niobium path length of around 59 cm. Assuming a 50μm line width, 300nm thickness and a film resistivity of $3.5 \times 10^{-7}\Omega$m, this gives an estimate for the total device resistance of 13.7 kΩ. The first device we manufactured had a resistance of 14.0 kΩ, which seemed encouraging.

To see if the device was a conducting path of the right form, and that there were no shorts in the crossover regions, OPTPOD2 was scanned using a high resolution SQUID gradiometer called SQUIDLET [49]. SQUIDLET was initially designed to look at small biological systems but its small bottom coil (and hence high spatial resolution) make it ideal for looking at thin-film devices. A 1mA current was passed through OPTPOD2 and SQUIDLET was scanned in a plane 5mm above the wafer. Figure 7.8 shows the magnetic field both as a contour map and in a 3d representation. The data clearly indicate that all three coils of OPTPOD2 are generating field, and that the centre coil is producing field in the opposite direction to the other two coils. The small hill to one side of OPTPOD2 is generated by the wires carrying current into the gradiometer. An approximation to the actual current flow can be derived using the so called V_3 transformation [28]. If S(x,y) is the signal from SQUIDLET then V_3 is a vector whose components are defined by

$$\begin{aligned} V_{3x}(x,y) &= \frac{\partial S(x,y)}{\partial y} \\ V_{3y}(x,y) &= -\frac{\partial S(x,y)}{\partial x} \end{aligned} \tag{7.5}$$

Figure 7.9 shows the V_3 plotted for the scan over OPTPOD2. The plot only shows those arrows which have a modulus greater than 0.45 of the maximum modulus. The current can

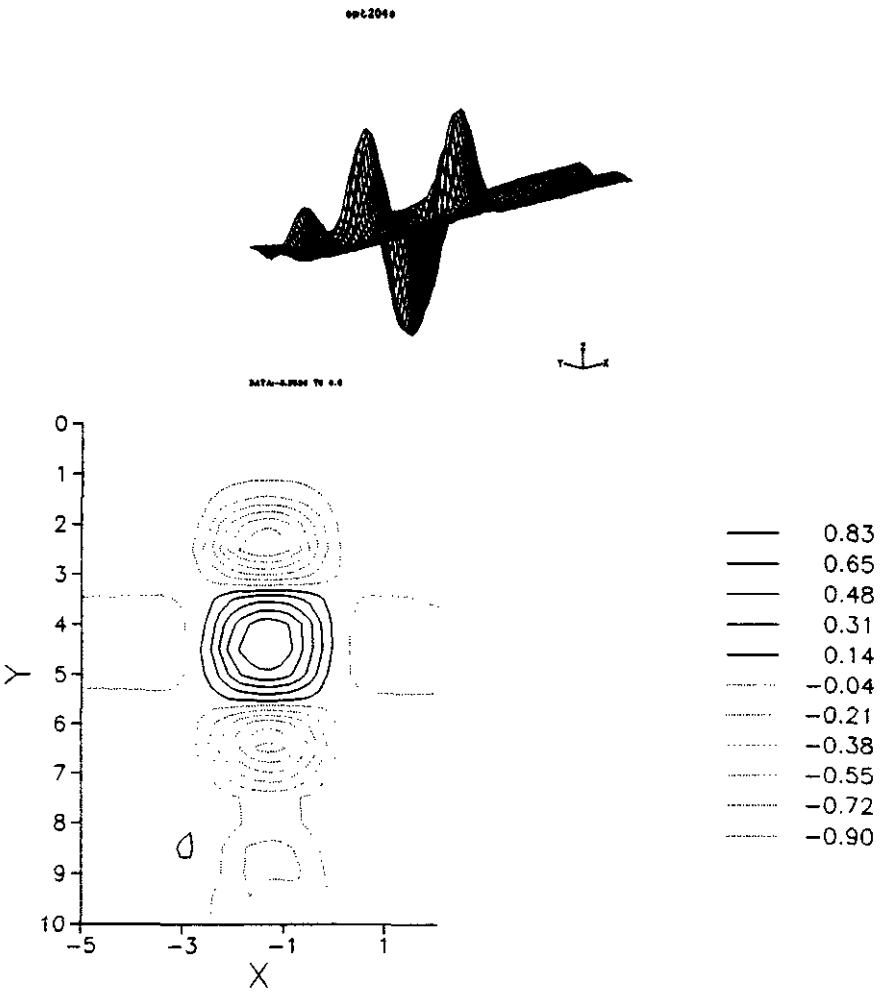

Figure 7.8 SQUIDLET scan of OPTPOD2.

clearly be seen circulating round all three coils, but in the opposite direction in the centre coil.

So it was clear that this device had been fabricated correctly, and the final test was to see if it was superconducting. Four contacts (two to each contact pad) were attached to the gradiometer using a low-temperature Indium solder. An AC signal at 28Hz was used to cancel any thermal e.m.f effects that might occur, and was applied to the two outer contacts. The voltage drop was measured as a peak-to-peak value across the two inner contacts, and the current was measured as a peak-to-peak voltage drop across a 9.85kΩ resistor in series with the gradiometer. Figure 7.10 shows the resistance as as function of temperature (Note that the only calibrated temperatures in this plot are room temperature, T=293.5K and the liquid helium temperature, 4.2K).

The curve clearly shows a transition but not to a zero resistance state. The most plausible explanation for this is that the majority of the device is superconducting but that there is not a superconducting path at the crossover vias. After the first layer of niobium is sputtered it quickly grows a very thin layer of oxide which the second layer has not penetrated. There are two possible solutions to this problem. Firstly, if the sputtering

system allows multiple targets, then immediately after sputtering the niobium first layer, a 5nm thick layer of gold can be sputtered on top. This will prevent oxide growth but is thin enough to superconduct itself, because of the proximity effect. Secondly, prior to film deposition of the top niobium layer, rf energy can be applied to the wafer instead of the niobium target. Argon bombardment of the wafer will strip off the oxide and allow the deposition of the top layer of niobium onto a fresh niobium base.

Unfortunately, neither of these options was available on the Leicester sputtering system.

This experience we have gained in this area suggests that the fabrication of thin-film gradiometers is possible, but requires very stringent clean room conditions, together with the very best equipment. It is perhaps worth noting that at present no multi-channel system has been constructed using thin-film gradiometers, despite the many advantages. This is a reflection of the poor device yield many groups are experiencing.

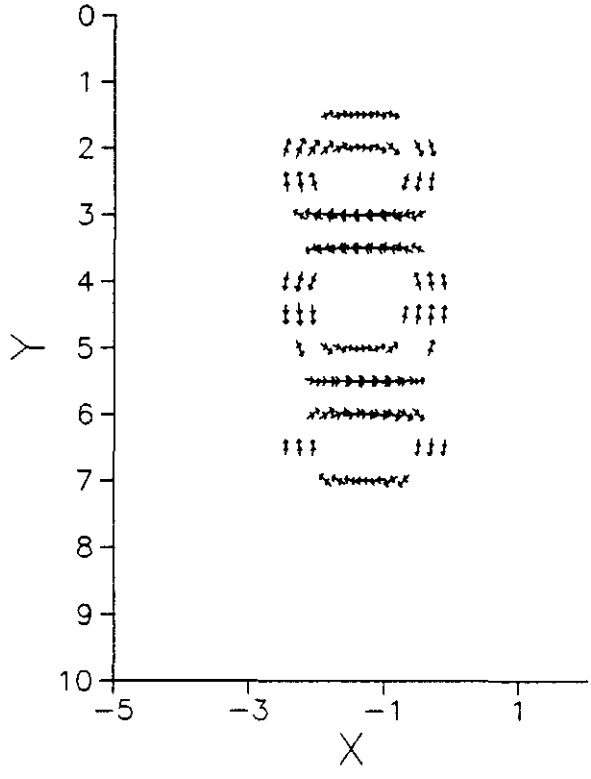

Figure 7.9 V_3 plot of SQUIDLET scan over OPTPOD2.

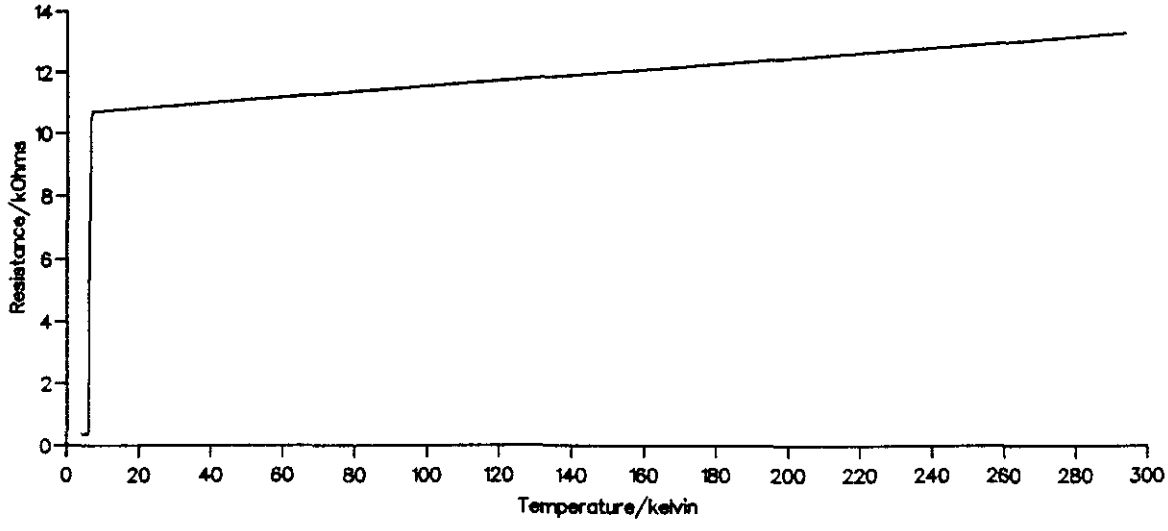

Figure 7.10 4 point cooling curve for OPTPOD2.

Appendix A

Contour maps of field derivatives

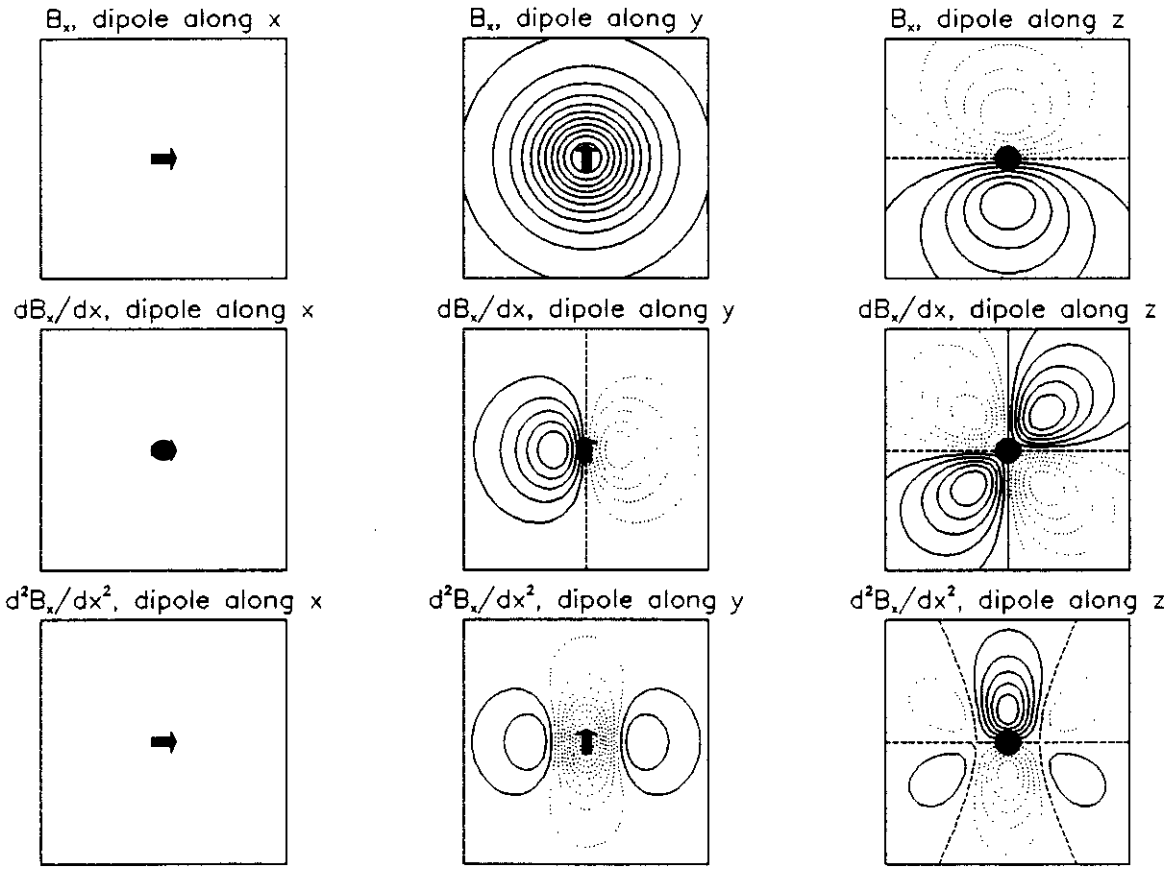

Figure A.1 B_x and its x derivatives.

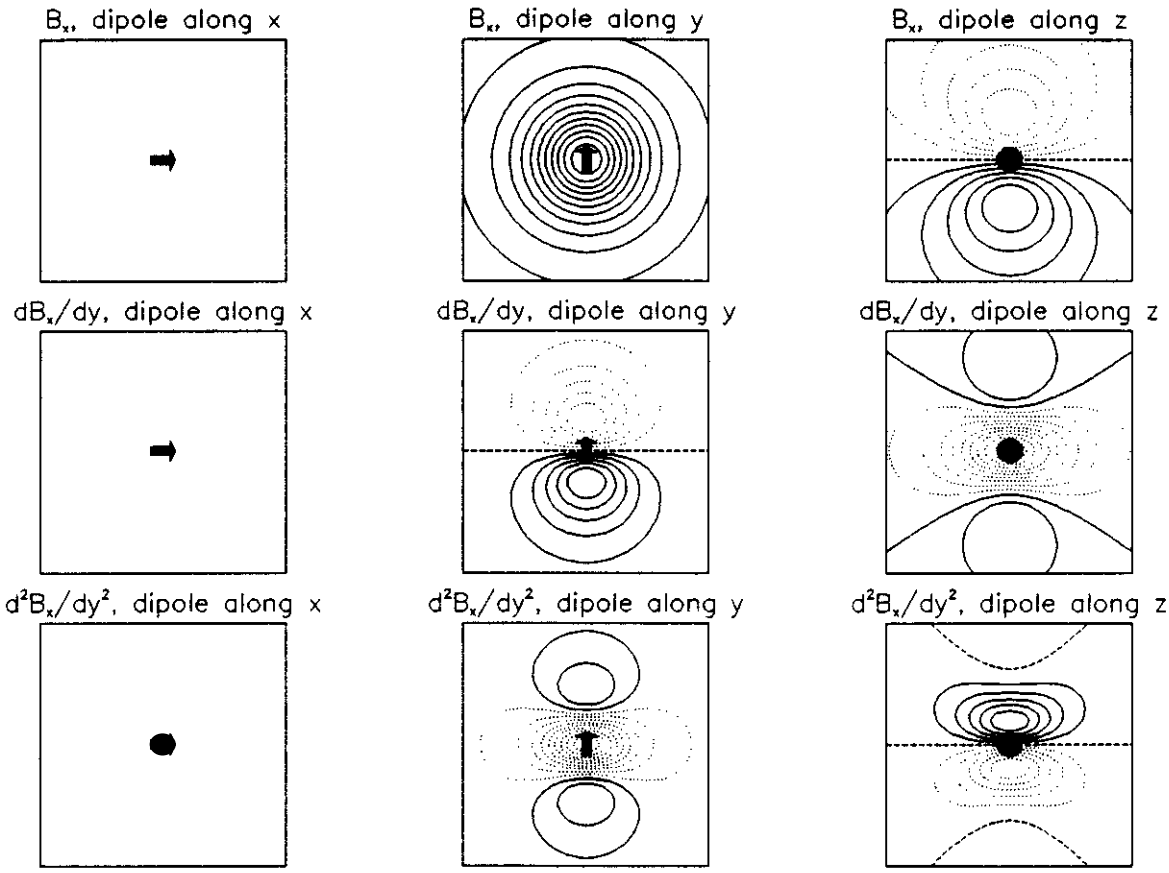

Figure A.2 B_x and its y derivatives.

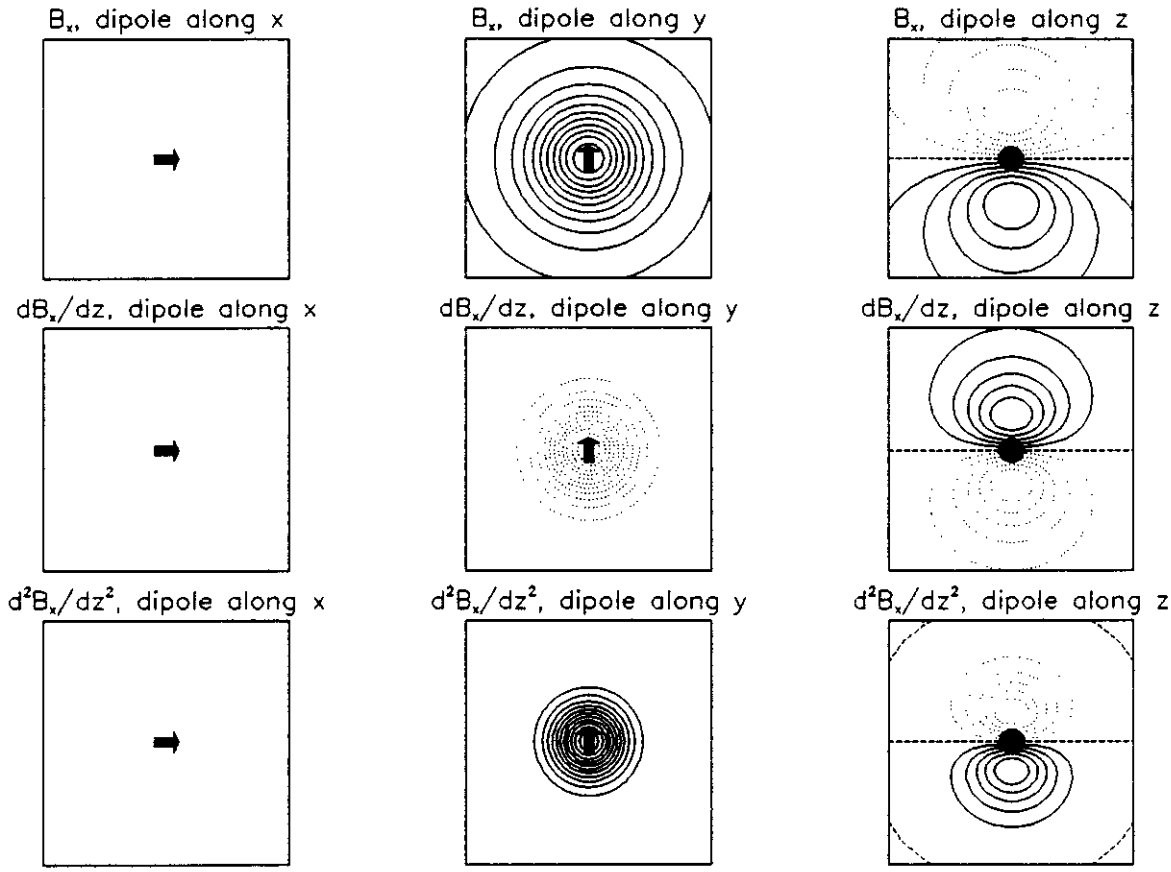

Figure A.3 B_x and its z derivatives.

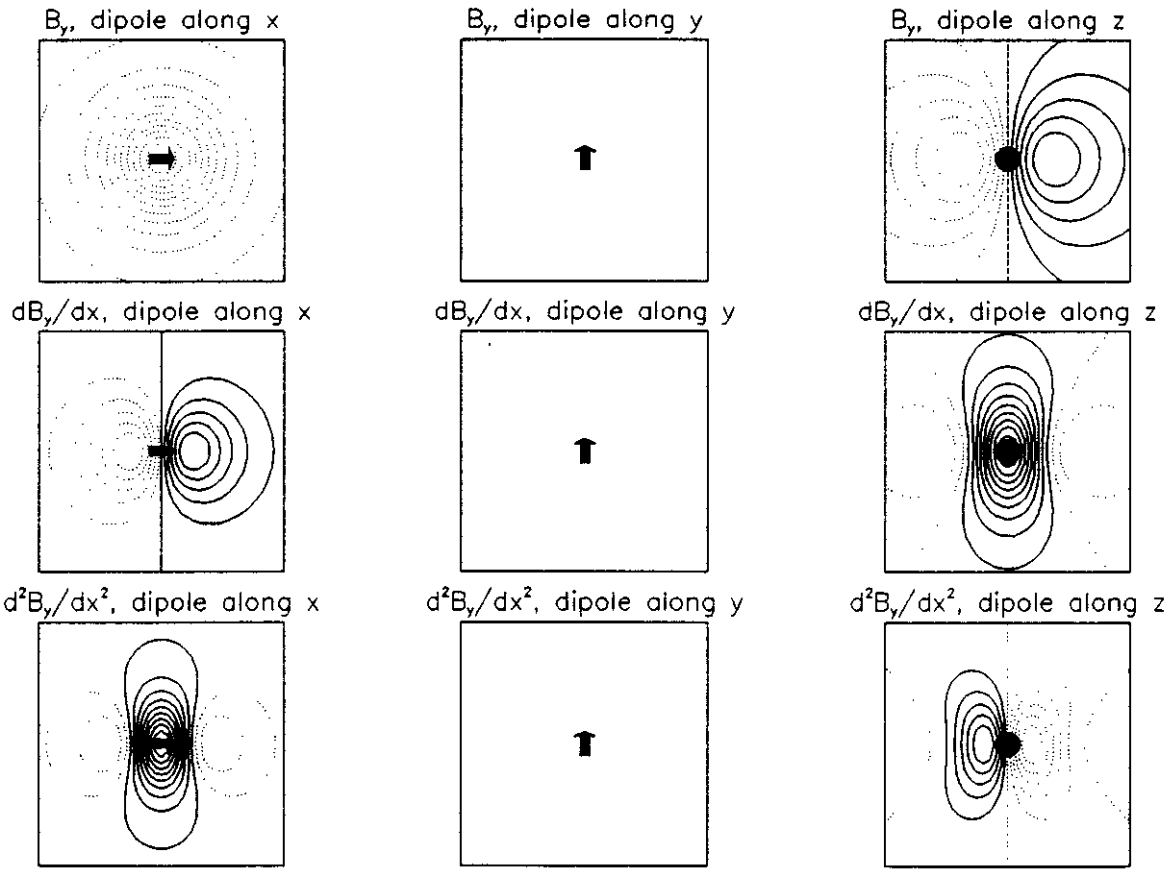

Figure A.4 B_y and its x derivatives.

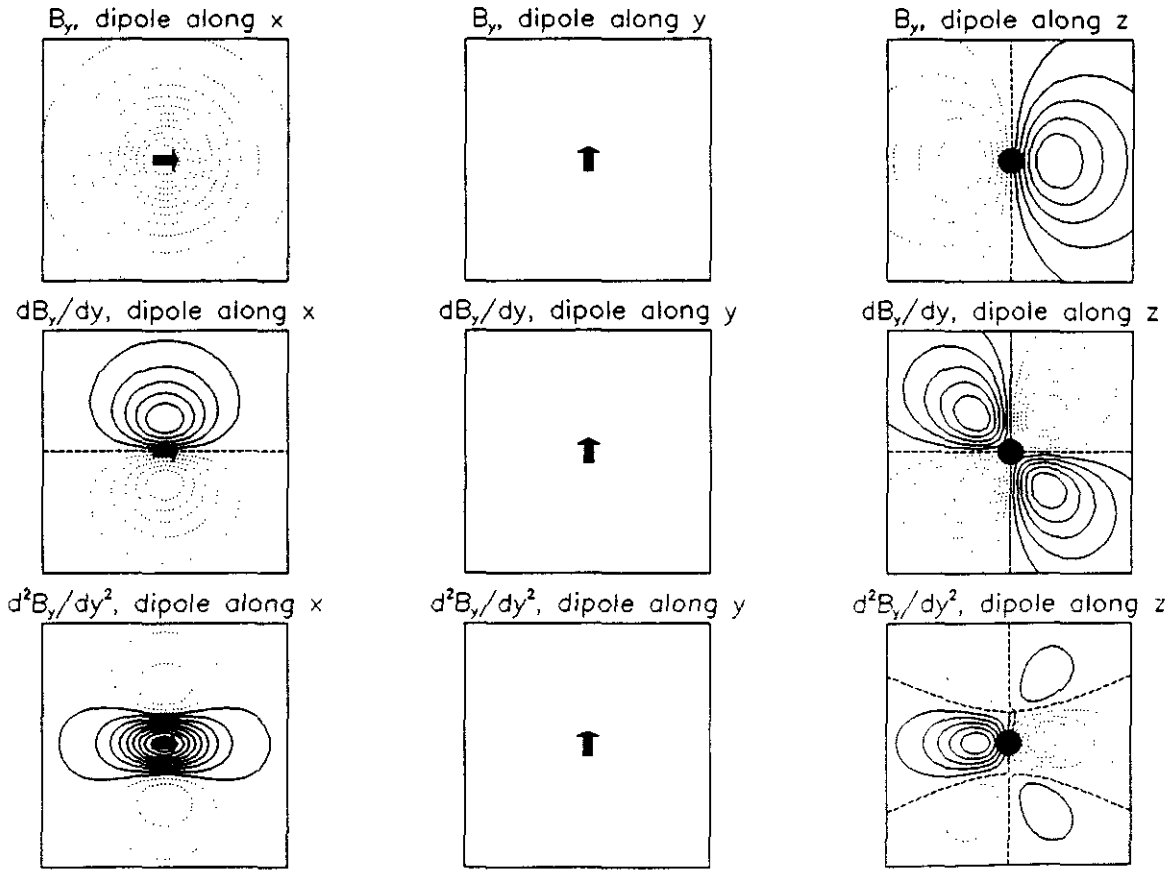

Figure A.5 B_y and its y derivatives.

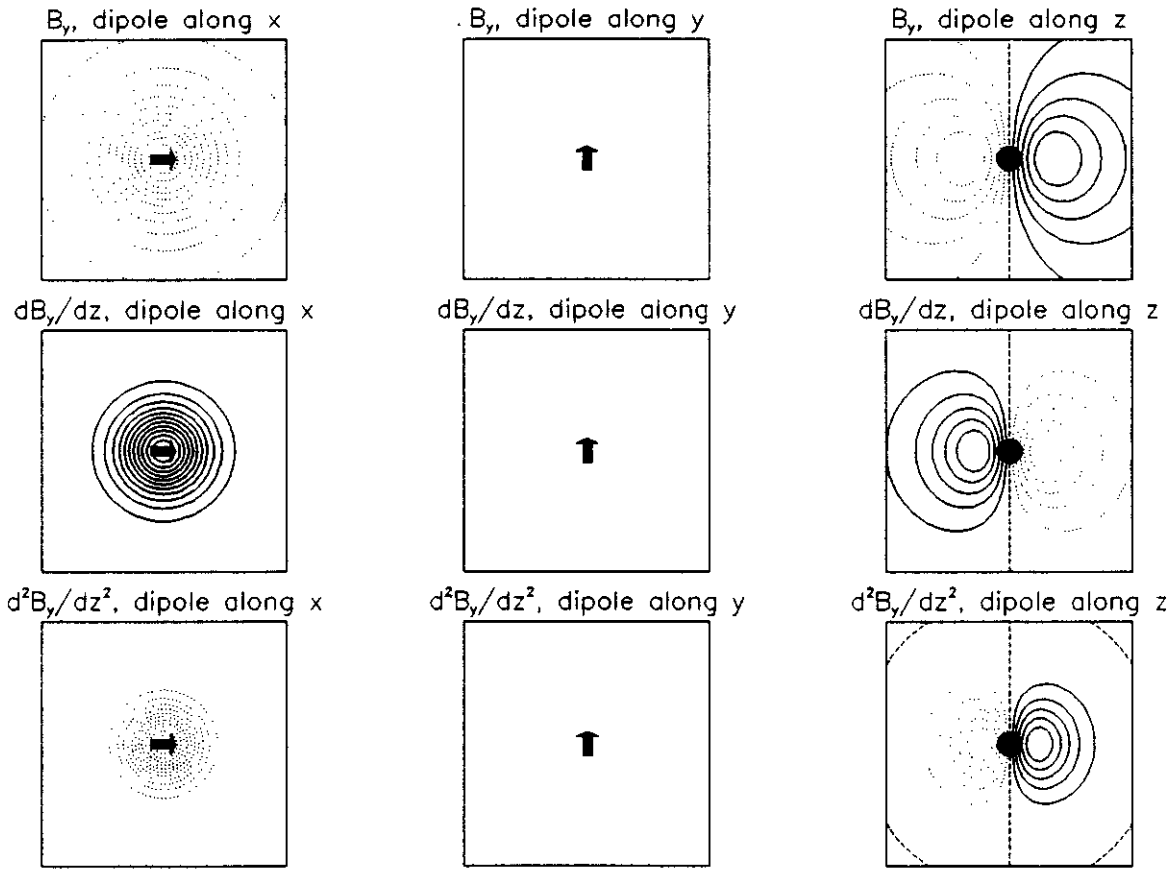

Figure A.6 B_y and its z derivatives.

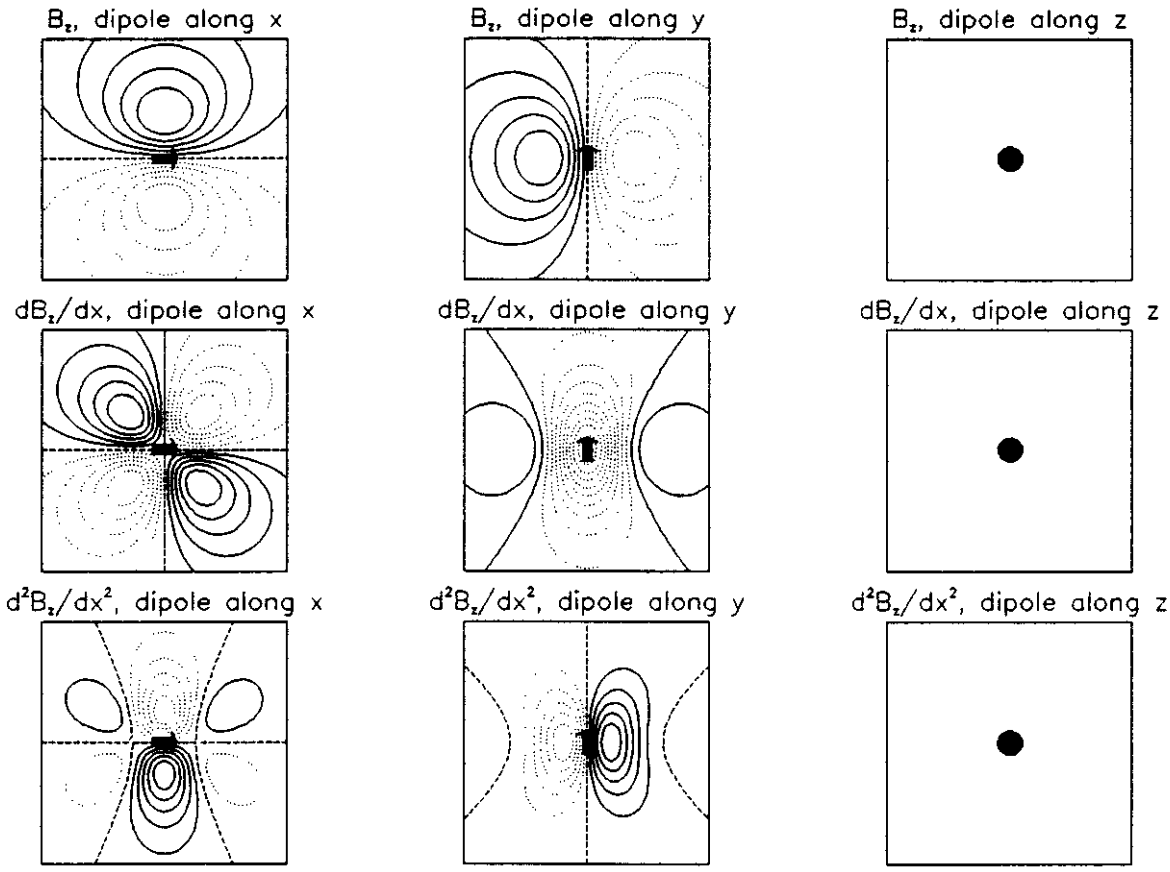

Figure A.7 B_z and its x derivatives.

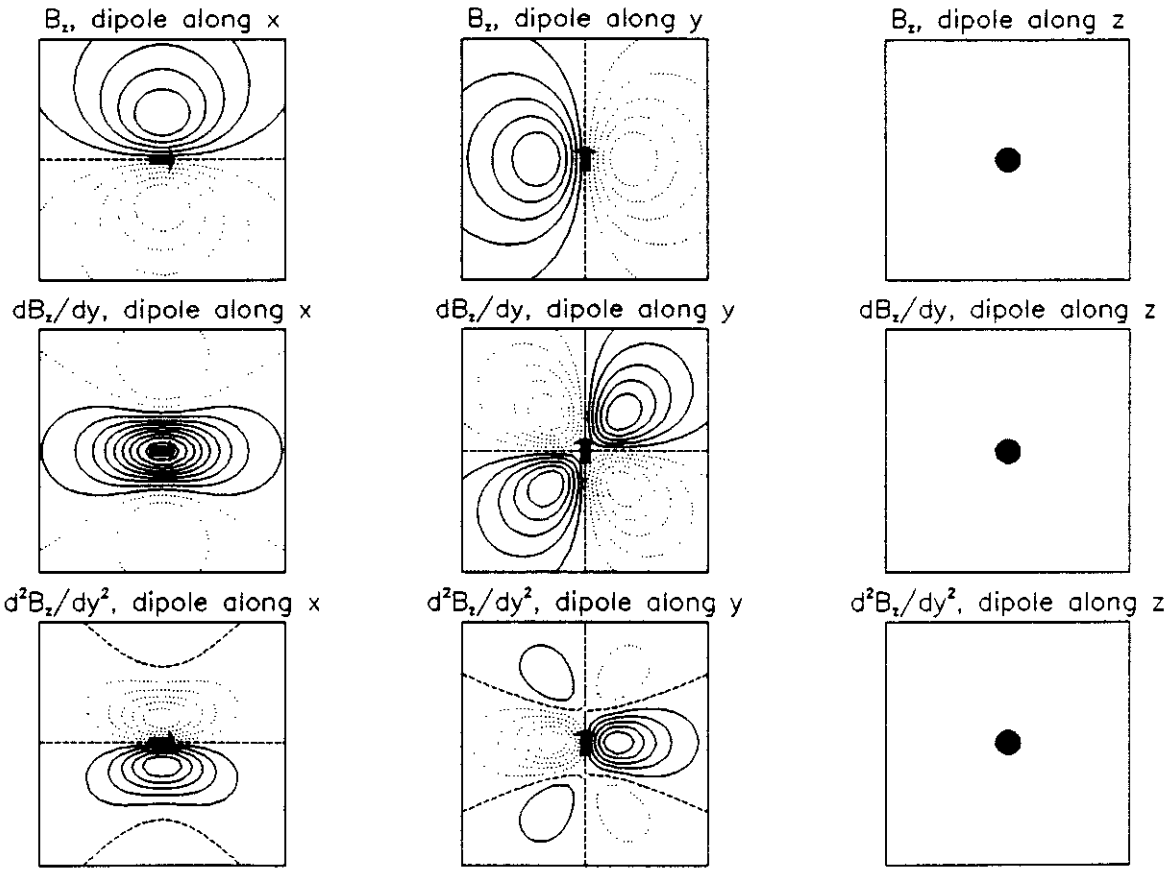

Figure A.8 B_z and its y derivatives.

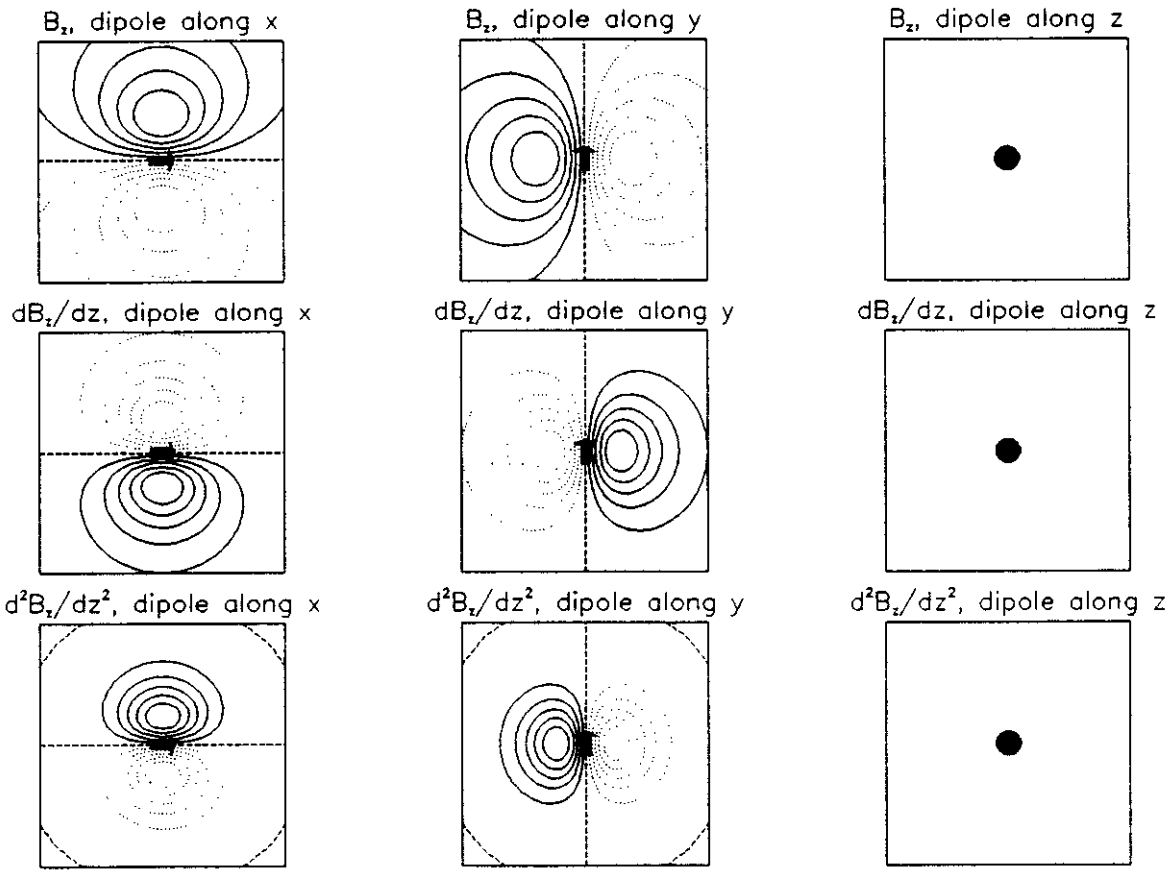

Figure A.9 B_z and its z derivatives.

Appendix B

Software library

In this appendix we present a brief description of the software developed for this thesis.

DESIGN

This program allows the user to design and comprehensively test any gradiometer with any combination of current dipole sources. It calculates parameters such as dipole sensitivity and spread, as well as interfacing with graphics packages to provide graphs of response to particular sources.

Each gradiometer is defined as a set of arbritarily oriented coils, which can be either rectangular or circular.

PATH

This program performs path analysis of any arbritary gradiometer path, to give the intrinsic balance and inductance of the device.

HUNT

Given SQUID parameters and the design limitations, HUNT will find the best planar gradiometer by using a numerical search procedure.

GCL

GCL is a graphics control language which allows the production of contour maps of magnetic field data. Options include user-specified annotation and automatic superimposing of current dipoles. GCL is also the graphics environment for the ABIS rulebase.

DataView

DataView is a major graphics/analysis package for looking at magnetic field data immediately after collection in the lab. Data can be drawn as scans, intensity images or contour maps. DataView also performs user controlled software filtering of the dataset.

DataView has been specially designed to be 'user-friendly', and is usually operated in a mouse-icon environment. The user can identify signal values and latencies by simply pointing a crosshair cursor at the scan and pressing the mouse button.

REGION

REGION will look through an entire time-series of current density inversions and pick out active regions. The user specifies the size of region to look for and REGION will find all the appropriate regions, together with the latency at which each region reaches its maximum strength.

IMAGE

IMAGE is an advanced tool for graphically analysing a time-series of current density inversions. Like DataView it has an icon interface which allows the user to view the current density, in a variety of representations, at any latency. The user can graphically select a region of interest and plot the activation curve for that region over a specified latency band. IMAGE will also track peak activity over the source space as a function of time.

In anticipation of the use of MRI images, IMAGE can use any raster image as a backdrop for its representations, as well as allowing the user to annotate the final image using text etc.

B.1 List of commands

In this part of the appendix we list the commands available in the software tools describe in chapter 5. Menu structures are shown using indentation, and any descriptions are prefixed by a % character.

B.1.1 DataView

```
files       % enter a menu which allows selection of a particular file
              from the set
restart     % restart DataView
double      % display scans twice as high
half        % halve the scan height
local       % select local normalisation
global      % select global normalisation
grey        % load grey scale colour palette
colour      % load full colour palette
pick        % use pointer to measure signal values/time etc
image       % display entire timesequence as a set of tiny colour images
scans       % display as scans
quit        % leave DataView
```

```
select        % define current working timeslice
limits        % select time limits for scans
filter        % perform band-pass filtering
save          % save current data file

examine       % menu for looking at signals in colour block
                representation (single timeslice)
        return        % back to main
        forward       % next timeslice
        back          % previous timeslice
        sequence      % animate through all timeslices

map           % contour map representations
        return        % back to main
        local         % local normalisation
        global        % global normalisation
        forward       % next timeslice
        back          % previous timeslice
        select        % select timeslice
        files         % select data file from set
        shaded        % plot a colour shaded contour map
        v3            % plot a V3 arrow map
        line          % plot a line contour map
        save          % save an interpolated  map
        sequence      % save a timesequence of interpolated maps

trace         % follow position of maximum activity with time
        save          % save trace data
        load          % load trace data
        local         % local normalisation
        global        % global normalisation
        calculate     % calculate trace data
        display       % draw the trace
        animate       % animate the trace
        snail         % join trace positions
        return        % return to main
        files         % select file from the set

arrow       % represent signals as an arrow (only vector gradiometer systems)
        return       %  return to main
```

```
forward     % next timeslice
back        % previous timeslice
sequence    % animated sequence
```

B.1.2 GCL

```
set_scan_lines      %  set zero line for scans plot
laser_queue         % set laser queue for printing
set_axes            % turn axes on/off
set_arrow_scale     % define arrow map scale constant
intensity_v3        % plot an intensity map + a V3 map
shaded_v3           % plot a shaded contour map + a V3 map
cont_v3             % plot a line contour map + a V3 map
v3                  % plot a V3 map
chop                % enter map data editor utility
describe            % describe the size and form of a data map
edit                % enter text editor to alter data values
safe                % remove illegal characters/illegal number formats
                      from a data file
grad                % calculate two dimensional gradient of a scalar map
set_arrow_limit     % set arrow map cutoff limit
set_no_image        % turn off background raster image
set_image           % define background raster image
triangle            % plot special triangle plot (for the 3 channel system)
intensity_arrow     % plot intensity map + arrow map
shaded_arrow        % plot shaded contour map + arrow map
cont_arrow          % plot line contour map + arrow map
set_no_overlay      % turn off line drawing overlay
set_no_sources      % turn off dipole source overlay
set_overlay         % define line drawing overlay
set_sources         % define dipole source overlay
scans               % plot scans
line_intensity      % plot line contour + intensity map
line_shaded         % plot line contour + shaded contour map
contour             % plot line contour map
shaded              % plot shaded contour map
intensity           % plot an intensity map
arrow_map           % plot arrow map
show                % show current settings
set_dir             % set data directory
calc_limits         % set local normalisation
```

```
limits              % define global normalisation constants
set_title           % set title
set_head            % set heading
set_colour          % set colour palette
set_device          % set current graphics device
set_defaults        % reset settings
set_save            % set filename for saving image in LaTeX importable form
(..vms..)           % do operating system command
set_notify          % turn on/off messages
set_scale           % turn on/off colour scale
waitforret          % wait for return to be pressed
set_no_save         % turn off image save option
execute             % execute a GCL program
end_execute         % end a GCL program
help                % enter HELP environment
end_defaults        % end of the defaults file
dir                 % show data files
sq                  % show laser queue status
set_head_map        % heading for plots is the map filename
line3d              % plot a line 3D representation
shaded3d            % plot a colour shaded 3D representation
gcl                 % restart GCL
```

B.1.3 ABIS/SPHERE

In this subsection we present documentation for the ABIS expert system and the sphere rulebase described in chapter 5. This documentation is an abridged version of the full documentation written by Palfreyman et al.

ABIS

picture Map Display a Map on the screen as a 3-d picture, using GCL.

block Map Display a Map on the screen in coarse resolution, using GCL.

contour Map Display a contour Map on the screen, using GCL.

default_smoothing(N) When asserted in the rulebase, this defines the default level (N= $0, 1, \ldots$) of smoothing of maps which is required when using *describe*. ABIS provides a default smoothing of 2.

sources Define a source configuration.

grad Define a gradiometer design.

describe Map Display a description of a Map on the screen. The components of a description are:

disturbance(D) D is a measure of the amount of activity in the map.

edge(Label,(X1,X2),(D1,D2),Mag) A local gradient maximum at the position (X1,X2) and with direction (D1,D2) and magnitude Mag.

dot(Label,(X1,X2),Radius,Mag) A local extremum of convexity of the map — a "hump" or "hollow" — with its position, Radius and Magnitude.

weight(Label1,Label2,Sep,Rel,Contr) A number of useful parameters relating dot(Label2) to edge(Label1). Sep is the separation between the two, Rel is the likelihood that the dot is related to the edge, and Contr is the proportion of the dot which is caused by a dipole at the location of the edge.

Description describes Map_spec • If Description is a variable, it is instantiated to a list describing the Map_spec in terms of edges, dots and weights; otherwise Description is a notion which generates a description of the Map_spec.

- If Map_spec is a map name, this map is described using the default_smoothing specified in the rulebase.
- If Map_spec has the form "N-smoothed Map", the named Map is first smoothed N times, and then described.
- If Map_spec has the form:

```
Original - Proportion * Fit_field about (Px,Py),
```

where Fit_field has the form:

```
Grad( dipole((X,Y,Z), (Dx,Dy,Dz), Magnitude)
```

then Original is taken as a map name from which is subtracted a Proportion of the field obtained from the given Gradiometer scanning the given source dipole. This field is fitted to the Original field in the convex (or concave) region about the point (Px,Py). The difference map obtained by this process is then described by Description. An example of this form of *describe* might be:

```
descrn describes
        orig - 0.7*ou(dipole((1.4,1.6,-5),(-0.6,0.8,0),Mag))
        about (2.7,3.4).
```

After this satisfying this goal the uninstantiated variable Mag would become instantiated to the best-fit dipole strength. Note that this form of *describe* is very specific, and will only work if those variables are instantiated which are instantiated in the above example.

Map equals Expression Map is the name of a MAP file, which will contain the regularised data obtained by evaluating the given Expression. Valid forms are:

- map1 equals map2.
- patch((Nx,Ny), (Sx,Sy), (Dx,Dy)) equals patch(map1).
- map1 equals grad(map2).
- map1 equals bti1(source1) over map2. map1 is obtained by scanning a source configuration source1 with the gradiometer bti1 within the coordinate patch of map2.
- `map1 equals map2 - 0.98 * Fit_field about (Px,Py),`

  where Fit_field has the form:

  `Grad( dipole((X,Y,Z), (Dx,Dy,Dz), Magnitude)`

  map1 is the residue obtained by subtracting from map2 0.98 of the field obtained from the Gradiometer bti1 scanning the given source dipole. This field is fitted to the field map2 in the convex (or concave) region about the point (Px,Py) and subtracted from map2. The residue map is then stored in map1.

store(Notion,List) Save a List of items as the structures generated by the given Notion.

map(Data) Regularise the given DAT file to obtain a map of the same name.

sources(Internal,External) If Internal is a variable then it is set to the internal representation of the source configuration contained in the file SOURCES:External.DEF; otherwise, this the given Internal representation is written to the External source file in standard format.

diff(Vector1,Vector2,Diff) Diff is set to a measure of the degree of "difference" between two (normalised) dipoles or edges.

decreasing_magn(Edge1,Edge2) This is true if the magnitude of Edge1 is greater than the magnitude of Edge2.

Grad gives_separation_relation (S,R) R is a variable which is set to the radial position of a dipole which would lead to the given separation S, using the given Gradiometer and assuming default smoothing.

(Grad,Smoothing) gives_separation (S,R) This has the same effect as above, but gives the option of assuming a different level of smoothing.

weight(Relevance,Contribution,W) W is a variable which is set to an appropriate combination of Relevance and Contribution weights. These are obtained from the weights in a map, and are combined to give a measure of how likely it is that the edge and dot related by the weight are corresponding features of a single underlying source.

reduce(Description) Description is a given notion which generates a map description. Reduce that description by eliminating all information relating to edges which are not regarded as significant. This is assessed by *significant_edge*.

significant_edge(Edge) Assess whether or not a given Edge is likely to correspond to a dipole. At present this is done simply by checking whether the magnitude of the Edge is greater than 0.8.

The SPHERE rulebase

The *sphere* rulebase implements the dipole location process which has been described in chapter 5 for the case of a uniformly conducting sphere with the gradiometer *she.des*. The extra predicates that become available when the SPHERE rulebase is loaded into ABIS are the following:-

Solution underlies Map Find a Solution set of dipoles for the specified Map, allowing at most four dipoles at each peeled level.

peel(Map, Solution, Residue) Peel off at most four dipoles from a Map, which constitute the first–order solution to the Map. Merge these dipoles into the set Solution, and return the Residue map.

N-dipole_guess(Map, Solution) Find the initial estimate of the Solution to a Map, using not more than N dipoles.

diff(Vector1, Vector2, Diff) Calculate a measure of the degree of Difference between two (normalised) Vectors.

B.1.4 IMAGE

The brief documentation for IMAGE is in two parts. Firstly there is a list of all the interactive menu commands, and then there is a description of all the IIL commands that IMAGE understands. The use of IIL is descibed in chapter 5. Note that the 'top' menu command always returns the user to the main set of menu commands.

Menu structure

```
-----------------------------------------------------
plots:-
       mark maximum
       magnitude plot
       pick point
       plot activation
       plot peaks
       auto max
       plot snake
       arrow map
       more plots:-
                   loop
```

```
                    plot depths
                    add text
                    plot overlay
                    polyline
                    image plot
                    montage plot
                    cylinder plot
                    back to plots
                    image plot
        top
-----------------------------------------------------
files:-
        save image
        set data root
        set back image
        top

-----------------------------------------------------
hardcopy:-
           laser printer
           colour printer
           laser printer
-----------------------------------------------------
view style:-
             colour mode:-
                         colours
                         reversed colour
                         black/white
                         reversed b/w
                         pos/neg
                         false mri scale
                         top
             data draw mode:-
                            shaded contour
                            line contour
                            grid image
                            top
             activation mode:-
                             plot as a line
                             plot as arrows
```

```
                        lines + arrows
                        top
            set image limit
            define window
            reset windows
            pick mode:-
                        pick mark on
                        pick mark off
            set transform:-
                        transform on
                        transform off
                        top
            montage options:-
                        montage mark
                        no montage mark
                        montage ann on
                        montage ann off
                        top
            top
-------------------------------------------------
annotation:-
            clear marks
            set mark
            set overlay
            set heading
            set axes:-
                        axes on
                        axes off
                        top
            top
-------------------------------------------------
data style:-
            set stimulus
            set step
            set angle
            set max
            auto max
            use magnitude
            use dot product
            set power
```

```
            top
-------------------------------------------------
clear screen
-------------------------------------------------
description
-------------------------------------------------
repaint
-------------------------------------------------
exit
-------------------------------------------------
```

IIL commands

The form of this list is slightly different to those previously presented. Comments are not prefixed by indentation. IIL commands are all 4 characters long, and are followed by a list of arguments, which are shown enclosed in <>. Integer arguments start with an i or an l in the list below. Character string arguments are shown prefixed by a $ character.

```
-------------------------------------------------------------------------
pick <ipos>
                Pick a point in window number <ipos>. User selects point
                interactively using mouse/tablet
-------------------------------------------------------------------------
actv <ipos> <istart> <iend> <iactcol>
                Initiate an activation curve. User specifies region
                interactively using mouse/tablet.
Region is selected from window <ipos>.
Latency range is <istart> to <iend>.
                The curve is drawn in colour <iactcol>.

                Note that 'actv' is an interactive front-end for the
                'regn' command
-------------------------------------------------------------------------
regn
<ipos>
<istart>
<iend>
<iactcol>
<ixbot>
<iybot>
<ixtop>
<iytop>
```

Plot an activation curve for the data already represented in window <ipos> for the latency range <istart> to <iend>.

The colour of the curve is <iactcol>. The region within the source disk picked by the user, from which the activation is calculated is specified by a rectangle. The bottom left is specified by <ixbot>,<iybot>. The top right is given by <ixtop>,<iytop>. These coordinates are measured in data points i.e 1 to 17 in the normal hyper map.

---

autm <ipos> <istart> <iend>

Calculate the normalisation constant for window <ipos> by scanning through all slices in the latency range <istart> to <iend>.

---

lase

Send current image to laser printer (in batch mode)

---

file

Send current image to a LaTex file (in batch mode)

---

colp

Send current image to colour printer (in batch mode)

---

clrs

Clear screen and reset image to its original state

---

quit/halt/exit

Finish IMAGE run

---

vuim <xstart> <ystart> <xext> <yext>

Define the background raster image extent within the plot window. The above 4 parameters are specified as fractions of the physical window.

---

vuda <xstart> <ystart> <xext> <yext>

Define the data image extent within the plot window. The above 4 parameters are specified as fractions of the

physical window.

---

dark <ibase>

Set the intensity value for 'black' in the background raster image. <ibase> is 0 to 255

---

datm <idatm>

Set data representation mode:-

idatm = 0 line contour map

idatm = 1 shaded contour map

idatm = 2 grid image map

---

imon <ipos>

Plot the background video image in window <ipos>

---

ovpl <ipos>

Plot the current line overlay in window <ipos>

---

mark <xp> <yp>

Define a cross-mark at <xp>,<yp>. The two parameters are normalised coordinates.

---

mkcl

Clear all cross-marks

---

stmk <stimlat> <stimdir>

Define a stimulus mark for activation curves. <stimlat> define the latency for the mark. <stimdir> indicates either +1 for upward mark. -1 indicates downward mark.

---

desc

Plot a set of text lines down the left margin fo the image. The text lines are read from a file defined by

temp:image.dsc

---

debg <idebug>

If <idebug> is 1, some diagnostics are printed during IMAGE operations. If <idebg> is 0, debugging is supressed.

```
gind <itype>
                Select graphics input device
                <itype> = 0     Keyboard cursor keys
                <itype> = 2     Mouse/graphics tablet
-------------------------------------------------------------------------
trac <itrans>
                Select coordinate transform mode
                <itrans> = 0    Turns off coordinate transforms
                <itrans> = 1    Enable coordinate transforms
                The transform is defined by the trans command
-------------------------------------------------------------------------
axes <iaxes>
                Select/deselect axes
                <iaxes> = 0      axes off
                <iaxes> = 1      axes on
-------------------------------------------------------------------------
axlm <xorig> <yorig> <xend> <yend> <$xaxtext> <$yaxtext>
                Define axis limits and axes text
-------------------------------------------------------------------------
stim <istim>
                Define stimulus latency
-------------------------------------------------------------------------
step <istep>
                Define step between timeslices
-------------------------------------------------------------------------
zmax <ipos> <znormal>
                Define normalisation constant for window <ipos>
                to be <znormal>. If <znormal> is zero, then local
                normalisation is used for each timeslice.
-------------------------------------------------------------------------
calc <icalc> <calx> <caly> <calz> <calpow>
                Define the dot-product mode for magnitude plots
                <icalc> = 0   Plot simple plot of modulus
                <icalc>=  1   Plot dot product value, <calx>,<caly>
                              and <calz> define the vector to use.
                <calpow> is the power to which the intensity value is
                         raised.
-------------------------------------------------------------------------
wind <ipos> <xstart> <ystart> <xext> <yext>
                Define the physical window <ipos> as fractions of the
```

total image. <xstart>,<ystart>,<xext>,<yext> are normalised coordinates.

---

mult <zmult>

Define a multiplication constant. All data is multiplied by this as it is read. Allows scaling of the modulus and a reversal of the arrow direction.

---

winr

Reset all physical windows to their defaults:-
0 is a big window covering the whole image
1 to 4 are each a quarter of the whole size
5 is the bottom half of the image

---

dirn <iangle>

Define a rotation angle in units of 90 degree. The data plots (magnitude/arrow etc) will be physically rotated within the window by this angle.

---

monk <imontmark>

Define whether a maximum arrow mark is placed on each of the montage images.
<imontmark> = 0 no maximum mark
<imontmark> = 1 maximum mark

---

mona <imontannot>

Define whether annotation is placed on each of the montage images.
<imontannot> = 0 no annotation
<imontannot> = 1 annotation

---

txsz <textmult>

Define the text size. Text is normally about 3.0 mm high but, for example, if <textmult>=3, the size would be about 9.0mm.

---

txju <textjust>

Define text justification.
<textjust> = 0 text left justified
<textjust> = 1 text centre justified

---

mode <iraster>

Define background raster image presentation mode.

<iraster> = 0 full shaded image

<iraster> = n image is presented as an n% edge detected line drawing.

---

picm <ipickmark>

Define whether an arrow mark is plotted during the pick operation

<ipickmark> = 0 No mark

<ipickmark> = 1 Mark

---

actm <iactmod>

Set the activation curve mode.

<iactmod> = 0 Line curve only

<iactmod> = 1 Arrow curve

<iactmod> = 2 Line and arrow curve

---

grhd <igrhd>

Set the heading for activation curves. Normally it is a latency heading.

<igrhd> = 0 No heading

<igrhd> = 1 Heading activated

---

cmod <ipalettecode>

Select the colour palette

<ipalettecode> = 0 Normal colours

<ipalettecode> = 1 Reversed colours

<ipalettecode> = 2 Grey shades

<ipalettecode> = 3 Reversed grey shades

<ipalettecode> = 4 Positive/negative colours

---

back <$rasterfilename>

Set the background raster image filename

No assumptions made on the filespec

---

root <$hyperfilename>

Set the hyper filename. Extension .HYP assumed

---

head <$headingtext>

Set the heading for each window. If <$headingtext> is defined to be a fullstop, IMAGE prints a heading which consists of the hyper filename and the latency.

---

text <xp> <yp> <$textstring>

Plot text on the image. <xp> and <yp> are the position and are normalised coordinates (i.e fractions of the whole image size).

---

dept <ipos> <istart> <iend> <iactcol>

Plot a depth graph in window 5. The depth values are found by taking the root name from window <ipos>, adding a .DEP extension and looking in the file specified by this filename. The depth values are plotted over a latency range <istart> to <iend>.

---

vlin <latx>

Draw a vertical line on the activation curve window. The latency at which the line is drawn is specified by <latx>.

---

hlin <zsigy>

Draw a horizontal line on the activation curve window. The signal value at which the line is drawn by is specified by <zsigy>.

---

mont <istart> <iend>

Draw a montage plot. The timeslices in the range <istart> and <iend> are represented as a set of small contour maps. IMAGE works out how small each plot should be.

---

data <ipos> <ilat>

Draw an intensity representation in window <ipos>. Data comes from the timeslice specified by latency <ilat>

---

dipl <ipos> <icol> <xp> <yp> <xc> <yc>

Draw a dipole mark. Coordinates specified in local, normalised coordinates. Position given by <xp>,<yp> and

direction/size by <xc>,<yx>

---

dipg <ipos> <icol> <xp> <yp> <zp> <xc> <yc> <zc>

Draw a dipole mark. Coordinates specified in global coordinates. IMAGE transforms them to local ones by using the transformation matrix specified by 'tran'. Position given by <xp>,<yp>,<zp>. Size and direction given by <xc>,<yc>,<zc>

---

arro <ipos> <ilat>

Draw an arrow map of the data at latency <ilat> in window <ipos>

---

mkmx <ipos> <ilat>

Mark the maximum modulus position with an arrow mark in window <ipos>. Data taken from latency <ilat>

---

peak <ipos> <istart> <iend>

Draw a set of coloured dots marking the maximum modulus in each of the timeslices in the latency range <istart> to <iend>. Display occurs in window <ipos>.

---

snak <ipos> <istart> <iend>

Similar to 'peak' shown above, but the dots are joined with arrows showing how the point of maximum modulus moves within the image

---

over <$overlayname>

Set a filename for a line drawing overlay. Directory 'overlays' and extension '.ovy' are assumed. The overlay file is usually a CALCOMP format file.

---

tran

<sradius>

<disp1x> <disp1y> <disp1z>

<rota1x> <rota1y> <rota1z>

<rota2x> <rota2y> <rota2z>

<rota3x> <rota3y> <rota3z>

<disp2x> <disp2y> <disp2z>

Setup the global-local transformation.

<sradius> is a scaling parameter and represents the
radius of the source disk

<disp1x>,<disp1y>,<disp1y>
is a displacement vector which is subtracted
from the global coordinates to move the
input vector to the rotation origin

<rot...>
is a 3x3 rotation matrix

<disp2x>,<disp2y>,<disp2y>
is a displacement vector which is added
to the rotated coordinates to move them
to the local system. Usually identical
to the disp1 vector.

---

boxd
<ipos>
<iactcol>
<ixbot>
<iybot>
<ixtop>
<iytop>

Draw a rectangle in window <ipos>, colour <iactcol>. The
bottom left is specified by <ixbot>,<iybot>, the top
right is given by <ixtop>,<iytop>. These coordinates
are measured in data points i.e 1 to 17 in the
normal hyper map.

---

poly
<icol>
<xp> <yp> 0
<xp> <yp> 1
.
.
.
<xp> <yp> 2

Draw a polyline i.e a set of connected straight line segments. Colour is <icol>. Coordinates of each node on the polyline specified as normalised fractions of the whole image, <xp>,<yp>. The code on the end of each line have the following meaning

0 move to <xp> <yp>

1 draw segment to <xp> <yp>

2 draw segment to <xp> <yp> and terminate the polyline

Bibliography

[1] G. M. Baule. and R. McFee, "Detection of the magnetic field of the heart", Am.Heart.J,**66**,95-96,(1963)

[2] D. Cohen, "Introduction", in Biomagnetism - an interdisciplinary approach, Plenum Press, (1983).

[3] B. D. Josephson, "Possible new effects in superconductive tunnelling", Phys.Rev.Lett 1:251, (1962).

[4] J. E. Zimmerman, P. Thiene and J. T. Harding, "Design and operation of stable rf-biased superconducting point-contact quantum devices, and a note on the properties of perfectly clean metal contacts", J.Appl.Phys, 41,1572-1580. (1970).

[5] K. D. Singh, A. A. Ioannides, U. Ribary, R. Llinas, F. Lado, "Extraction of dynamic patterns from distributed current solutions of brain activity", to be published.

[6] U. Ribary, A. A. Ioannides, K. D. Singh, R. Llinas, "Magnetic Field Tomography (MFT) of coherent Thalamo-cortical 40-Hz Oscillation in normal Humans and Alzheimer Patients", to be published.

[7] *Proceedings of the 7th International Conference on Biomagnetism*, Plenum, (1990).

[8] I. M. Thomas, Ph.D thesis, Open University (1991).

[9] B. S. Janday, Ph.D thesis, Open University (1987).

[10] J.Knuutila, Ph.D thesis, Helsinki University of Technology (1987).

[11] F. W. Grover. *Inductance Calculations.* Dover publications, New York, (1946).

[12] T. E. Dillinger. *VLSI Engineering.* Prentice-Hall, (1988).

[13] J. M. Doyle. *Thin-Film and semiconductor integrated circuitry.* McGraw-Hill, (1966).

[14] O. S. Heavens. *Thin-Film Physics.* Methuen, (1970).

[15] Kevex Corporation. *Energy dispersive x-ray microanalysis.* Kevex, (1983).

[16] A. H. Worsham, Yale University. Private communication.

[17] J. M. Frary and P. Seese, "Lift-off Techniques for Fine Line Metal Patterning", *Semiconductor International*, December 1981, p72.

[18] M. Hatzakis, B. J. Canavello, and J. M. Shaw, "Single-step Optical Lift-off Process", IBM J. RES DEVELOP. **24**(4), July 1980.

[19] G. G. Collins and C. W. Halstead, "Process Control of the Chlorobenzene Single-Step Liftoff Process with a Diazo-Type Resist", IBM J.RES DEVELOP. **26**(5), Sept 1982.

[20] D. J. Elliot. *Integrated Circuit Fabrication Technology*. McGraw-Hill, (1982).

[21] Shipley Chemicals. *Techical data for Microposit S1400 series photoresists*, (1986).

[22] G. B. Donaldson, "Fabrication of Tunnel Junction Structures", Superconducting Electronics, NATO ASI Series Vol. F 59.

[23] J. Vrba, A. A. Fife, M. B. Burbank, "Spatial discrimination in SQUID gradiometers and 3rd order gradiometer performance", CAN. J. PHYS. **60**, (1982).

[24] A. A. Ioannides, S. J. Swithenby, "An efficient magnetic flux integration method for bounded current sources", J. Appl. Phys. **61** (10), 15 May 1987.

[25] C. F. Gerald, *Applied numerical analysis*, Addison Wesley, (1970).

[26] M. B. Ketchen, W. M. Goubau, J. Clarke, G. B. Donaldson, "Superconducting thin-film gradiometer", J. Appl. Phys. **49** (7), July 1978.

[27] M. B. Ketchen, "Integrated Thin-Film dc SQUID sensors", IEEE Transactions on Magnetics **MAG-23** (2), March 1987.

[28] A. A. Ioannides, "Graphical solutions and representations for the biomagnetic inverse problem", Advances in Electronics and Electron Physics, Supplement 19 (Inverse Problems: An Interdisciplinary Study), (1987).

[29] C. M. Pegrum, "SQUIDs and their applications", presented at the Institute of Physics Low Temperature Techniques course, 5 Nov 1987.

[30] J. C. Gallop, B. W. Petley, "SQUIDs and their applications", J. Phys. E: Sci. Instrum. 9 417-29, (1976).

[31] N. M. Palfreyman, K. D. Singh and S. J. Swithenby, "Rule-based location of multiple current-dipole sources from biomagnetic data", Advances in Biomagnetism, Plenum Press, (1989).

[32] N. M. Palfreyman and S. J. Swithenby, "Modelling Human Expertise in Solving the Biomagnetic Inverse Problem", To be published.

[33] D. Marr, *Vision*, McGraw-Hill, (1980)

[34] A. A. Ioannides, Private communication.

[35] M. S. Hämäläinen and R. S. Ilmoniemi. Preprint TKK-F-A559, Helsinki University of Technology (1984).

[36] C. J. S. Clarke and B. S. Janday, "The Solution of the Biomagnetic Inverse Problem by Maximum Statistical Entropy", Inverse Problems 5 (1989) 483-500.

[37] C. J. S. Clarke, A. A. Ioannides, J. P. R. Bolton, "Localised and Distributed Source Solutions for the Biomagnetic Inverse Problem 1", Advances in Biomagnetism, Plenum Press, (1989)

[38] A. A. Ioannides, J. P. R. Bolton, C. J. S. Clarke, "Continuous probabilistic solutions to the biomagnetic inverse problem.", Inverse Problems 6, (1990).

[39] C.J.S. Clarke, "Probabilistic Methods In a Biomagnetic Inverse Problem", Inverse Problems 5, (1989).

[40] M. Kajola, S. Ahlfors, G. J. Ehnholm, J. Hallstrom, M. S. Hämäläinen, R. J. Ilmoniemi, M. Kiviranta, J. Knuutila, O. V. Lounasmaa, C. D. Tesche, V. Vilkman, "A 24-channel magnetometer for brain research", Advances in Biomagnetism, Plenum Press, (1989).

[41] P. K. Kemppainen, R. J. Ilmoniemi, "Channel capacity of multichannel magnetometers", Advances in Biomagnetism, Plenum Press, (1989).

[42] S. W. Kuffler, J. G. Nicholls, A. R. Martin, *From Neuron to Brain*, Sinauer Associates Inc, (1984).

[43] P. L. Nunez, *Electric fields of the brain: The neurophysics of EEG*, OUP, (1981).

[44] S. Ahlfors, R. J. Ilmoniemi, "Magnetometer position indicator for multichannel MEG", Advances in Biomagnetism, Plenum Press, (1989).

[45] W. H. Press, *Numerical recipies in C*, chapter 12, (1989).

[46] A. A. Ioannides, Private communication.

[47] S. Kuriki, K. Mizuno, "Design and fabrication of a planar gradiometer and dc SQUID system for biomagnetic measurements", Biomagnetism '87, Tokyo Denki University Press, (1987).

[48] S. Kohjiro, K. Enpuku, K. Yoshida, K. Yamafuji, "Thin-film gradiometer with large β dc SQUID", Biomagnetism '87, Tokyo Denki University Press, (1987).

[49] S. M. Freake, S. J. Swithenby, I. M. Thomas, "A miniature SQUID magnetometer for Detection of Quasi-DC Ionic current flow in Developing Organisms", Biomagnetism '87, Tokyo Denki University Press, (1987).

[50] H. Stefan, S. Schneider, K. Abraham-Fuchs, J. Bauer, H. Feistel, U. Neubauer, W. J. Huk, "Application of a multichannel MEG system in temporal lobe epilepsy", Advances in Biomagnetism, Plenum Press, (1989).

[51] Yu. Zhuralev, Private communication.

[52] A. Matlashov, Yu. Zhuralev, A. Lipovich, A. Alexandrov, E. Mazaev, V. Slobodchikov, O. Wazhiewski, "Electronic noise suppression in multichannel neuromagnetic system", Advances in Biomagnetism, Plenum Press, (1989).

[53] U. Ribary, R. Llinas, A. Kluger, S. H. Ferris, "Neuropathological dynamics of magnetic, auditory steady-state responses in Alzheimer's disease", Advances in Biomagnetism, Plenum Press, (1989).

[54] A. A. Ioannides, Private communication.

[55] J. H. Tripp, "Physical Concepts and Mathematical Models", in Biomagnetism - an interdisciplinary approach, Plenum Press, (1983).

[56] L. Kaufman, "Perception and event-related potentials and fields", in Biomagnetism - an interdisciplinary approach, Plenum Press, (1983).

[57] H.P. Lehmann, "Signal processing", in Biomagnetism - an interdisciplinary approach, Plenum Press, (1983).

[58] S. N. Erne, "SQUID sensors", in Biomagnetism - an interdisciplinary approach, Plenum Press, (1983).

[59] M. Scherg, T. W. Picton, "Separation and identification of event-related potential components by brain electric source analysis", Electroenceph. clin. Neurophysiol., Suppl., in press, EPIC IX.

[60] S. R. Butler, G. A. Georgiou, A. Glass, R. J. Hancock, J. M. Hopper, K.R.H. Smith, "Cortical generators of the CI component of the pattern-onset visual evoked potential", Electroenceph. clin. Neurophysiol., 1987, 68:256-267

[61] G. Barrett, L. Blumhardt, A. M. Halliday, E. Halliday, A. Kriss, "A paradox in the lateralisation of the visual evoked response", Nature Vol.261, May 20 1976.

[62] S. J. Williamson, "Introduction to cerebral modelling", in Advances in Biomagnetism: Functional localisation, World Scientific Press, (1986).

[63] M. O. Leach, "Spatially localised Nuclear Magnetic Resonance", in The Physics of Medical Imaging, Adam Hilger, (1988).